POLITECNICO DI MILANO

POLO TERRITORIALE DI COMO
School of Civil, Environmental and Land Management Engineering

Master of Science in Environmental and Geomatic Engineering

Investigation of the Asymmetry Attribute in Marine Controlled Source Electromagnetic (mCSEM) Data for Detection and Delineation of Resistive Anomalies.

Supervisor: **Prof. Giancarlo Bernasconi**
Co-supervisor: **Eng. Ahmed H. Mansi**

Master Graduation Thesis by:
Arinze Hawkins Hycienth Ezieke

Student ID number: **803643**

A. Y. 2014/2015

Dedication

To God almighty who strengthened and preserved me to witness this day.

Acknowledgements

The work presented in this thesis was made possible by the valued contribution of some individuals in Politecnico Di Milano, the morale support of some of my unwavering friends and of course the unending motivation and encouragement from my nuclear family.

I thank Prof. Giancarlo Bernasconi for his time, keen supervision and guidance. Reminiscing on the incessant appointments I asked for and your continuous adjustment of your tight schedule to accommodate me, I can't help but offer my unreserved appreciation to you.

Ahmed Mansi, your intelligent ideas and many fruitful discussions made this work a reality. Thank you for keeping me on my toes. I wouldn't leave out your wife (Neamat Gamal) who understood the situation and your sunshine, Roqayyah, whose smiles and giggles always brightened my day.

I also wish to thank Andrea Gola for his contribution in the building of the synthetic model and dataset and for all the useful discussions and suggestions. This thesis wouldn't have been complete without you.

To my wonderful family, how on earth would I have survived this journey without your contributions? When it seemed all hope was lost, your tiny voices kept me going. I am ever grateful to every one of you. Specifically, I am indebted to Engr. Chukwudi Ezieke and Mrs. Nkemdilim Okeke (nèe Ezieke); we started this journey together and now we are here.

Amarachi Fortune Ude, I am fortunate to have had you during this period, your encouraging words made the rough times seem smooth. I am thankful to Walter Malacrida, for always being at hand to tutor me when need be. You were a classmate, a friend and now a brother. To my friends, both home and abroad; Tuge, Ikeaka, CJ, Joe, Olivia, Di Wang, Vijay, Vuong, Florin, the Maryams, the Carolinas, Emilija, Gi Pe, Sepehr, Gina and any other person not mentioned, I am quite grateful for your company and support, I will choose you guys as friends anytime, any day.

Finally, I extend my gratitude to Chevron Global Cooperation for making available the GOM Benchmark dataset and the permission to use it for this studies and any further research involving mCSEM survey.

Abstract

Marine controlled source electromagnetic (mCSEM) method is able to detect resistivity variations in the subsurface, and so it can complement seismic method in order to reduce exploration risks.

The work presented in this thesis studies a qualitative method for the fast interpretation of mCSEM dataset, which is used to detect lateral extension of subsurface embedded resistive layers (resistors). The method is based on the analysis of the symmetry properties of the dataset. The symmetry attribute computation is applied on the magnitude component of the electric field observations of two dataset, canonical data from a 2.5D resistor model and a more realistic GOM benchmark data, both presenting a clear response indicative of the localities of subsurface resistors.

The method is extended to the phase component of the electric field which has been mentioned in literatures but not implemented. It is demonstrated that the phase component of the electric field can be exploited and relevant information about the subsurface resistive discontinuities can be obtained.

The asymmetry attribute method proves to be effective for qualitative detection of the lateral extent of buried resistors. Moreover, the combined outcome from both magnitude and phase components of the electric field observations will increase the degree of certainty of making decision about exploration and drilling prospects.

Table of Contents

List of Tables

List of Figures

Abbreviations

CSEM	Controlled Source Electromagnetic
EM	Electromagnetic
SBL	Sea Bed Logging
mCSEM	Marine Controlled Source Electromagnetic
MVO	Magnitude versus Offset
PVO	Phase versus Offset
Tx	Transmitter
Rx	Receiver
Hz	Hertz
m	Meters
km	Kilometres

1. INTRODUCTION

Marine controlled source electromagnetic (mCSEM) method is an electromagnetic sounding technique for hydrocarbon exploration which has the ability to differentiate resistive, potentially oil-bearing intervals from surrounding, more conductive water bearing units. Since seismic methods only give an idea of the presence of mineralized reservoir through measurements of changes in velocities of the rocks, supplementary method which properly detects the spatial distribution and borders of the subsurface resistive layers would increase the level of certainty and confidence of making decisions about exploration processes, bearing in mind that drilling and exploration projects are capital intensive, with costs reaching over millions of dollars.

This thesis will extensively investigate the efficacy and potential of the proposed electromagnetic attribute which is extracted from magnitude component of the electric field data of marine controlled source electromagnetic (mCSEM) acquisition, as a useful quantity for quick analysis and interpretation of mCSEM dataset and as a fast imaging tool for qualitative and direct identification of resistive bodies, such as mineralized reservoirs or geological discontinuities i.e., hydrocarbon reservoirs, basaltic bodies, etc. The analysis will be extended to the phase component of the electric field data which has been mentioned in literatures but has not been fully exploited. Demonstration will be carried out on the phase of a near realistic data to determine the potential of exploiting the phase component of the electric field of each receiver gather in order to obtain relevant information that will aid the interpretation workflow of the marine controlled source electromagnetic (mCSEM) data.

The outline of this thesis work is as follows:

A general introduction and overview of the thesis is presented in the first section of this chapter, while in the subsequent sections of this chapter the thesis objectives, approach and expected results are presented.

In the first section of the second chapter, tutorial on the general theory of mCSEM method is duly presented and discussed. The second section of the chapter covers an explanation of the theoretical methodology behind processing mCSEM data using the “asymmetry attribute”. In the last section of the chapter, an in depth review of literatures on the existing approaches and past works by various authors on CSEM and mCSEM data interpretation is presented.

Description of the model and dataset utilized in this thesis is presented in the first section of the third chapter, while in subsequent sections of the chapter, the application of the Asymmetry attribute to the already described dataset and an extensive explanation of each of the processing steps for the two utilized dataset is respectively presented.

In the fourth chapter, the results of the processing carried out on the datasets are presented, analyzed and duly discussed.

In the final chapter, the thesis is concluded based on the analyzed results and possible future work to be done proposed.

1.1. OBJECTIVES

Solving geophysical inverse problem for estimation of resistivity distribution in an investigated area is known to be ill-posed giving rise to a non-unique solution. Moreover, solving inverse problems is always likely to demand a high computational cost, thus utilizing preliminary information about the model to be estimated (i.e., through the approaches demonstrated in this work) constrains the inverse problem making the solution better.

This thesis exploits some methods, indicators and principles proposed in literature to explore, analyze and quickly interpret marine controlled source electromagnetic (mCSEM) data, providing fast and preliminary information that aids inversion.

The main aim of the work is to map the subsurface resistivity discontinuity of a simulated investigated area by applying innovative and special processing procedure based on symmetry attributes of marine controlled source electromagnetic (mCSEM) data, which serves as a fast imaging tool for qualitative and direct identification of resistive bodies, such as mineralized reservoirs or geological discontinuities which could be hydrocarbon reservoirs, basaltic bodies, etc.

The thesis extensively investigates the efficacy and potential of this proposed electromagnetic attribute extracted from marine controlled source electromagnetic (mCSEM) data as a useful quantity for quick exploration of marine CSEM dataset for better interpretation, through its application to the analysis of a synthetic canonical model data and to a more realistic data (Benchmark GOM dataset) generated and made available by Chevron Cooperation.

It also compares the results obtained using the attribute computed at different offsets of the receiver gather and that obtained when the attribute is computed at integrated range of selected offsets.

Finally, the thesis aims to demonstrate that the phase of the electric field versus the offset (PVO) of each receiver gather (which has been mentioned in literatures but has not been exploited) can also be explored and analyzed to obtain relevant information that aide the interpretation workflow of the marine controlled source electromagnetic (mCSEM) data.

1.2. METHODOLOGY

Symmetry properties of both the synthetic and the GOM benchmark dataset will be extracted, exploiting the unique electromagnetic attribute which is extensively explained in chapter two. The EM attribute is computed considering the in-towing and out-towing observations of the MVO plot of each receiver gather and the unique attribute which is a single value/parameter corresponding to each receiver is plotted against the receiver inline position thus making it possible for the effects of any subsurface buried body i.e., resistor and/or resistive anomaly and its lateral extent, distribution and boundaries to be imaged. Asymmetry attribute profile will be generated for both the non-normalized and normalized values.

Considering the amplitude component of the electric field, the processing of the marine CSEM data will toe the following steps:-

The electromagnetic attribute will be calculated (explained in the details in chapter Three) and the asymmetry attribute profiled along the receiver inline positions, altering different frequencies, i.e., same frequencies used for the marine CSEM acquisition, and at different offsets (short and long respectively) so as to image deep and shallow subsurface layers.

The electromagnetic attribute will be calculated and profiled along the inline receiver positions at a particular frequency (i.e., at fixed frequency) and at differing offsets. The effect of the subsurface resistor and/or resistive anomaly will be observed.

The EM attribute will be calculated for each receiver gather (i.e. along the receiver inline position), integrating in a selected range of offset and at different frequencies. These calculation will be done from offsets larger than 2000 – 3000 m, so as to omit responses at the MVO dominated by sea water attenuation. The corresponding effects of the subsurface will be mirrored and the observations duly noted.

Subsequently, following the above steps, it is demonstrated that the electromagnetic attribute can be profiled using the phase component of the electric field and necessary information about the subsurface resistivity can be extracted.

1.3. EXPECTED RESULTS

After proper analysis and application of the adopted methodology to both sets of data (Canonical model data and Chevron Benchmark GOM dataset) the expected results are as follows:

- A preliminary mapping of subsurface resistivity discontinuity.
- Qualitative identification of the presence, lateral extent, boundaries and location of the resistive anomaly and/or resistive body in the subsurface.
- Synoptic view of the electric field distribution at the seafloor and their attenuation with offsets.

- Quality control of the full dataset for quick identification of possible artefacts made possible by the generated algorithms.
- Sufficient information to aid the definition of proper a-prior models for electromagnetic inversion.

2. MARINE CONTROLLED SOURCE EM THEORY AND TUTORIAL

2.1. BACKGROUND

Measurement of electric resistivity beneath the seafloor have traditionally played a crucial role in hydrocarbon exploration, reservoir assessment and development. In the oil and gas industry, sub-seafloor resistivity data has in the past been obtained almost exclusively by wireline logging of wells. However, there are clear advantages to developing non-invasive geophysical methods capable of providing such information. Although inevitably such methods would be unable to provide capable vertical resolution to wireline logging, the vast saving in terms of avoiding the cost of drilling test wells into structures that do not contain economically recoverable amounts of hydrocarbon would represent a major advantage.

Electromagnetic (EM) sounding methods represent one of the few geoscientific technique which can provide information about the current state and properties of the deep continental crust and upper mantle. EM sounding respond to the distribution of electrical conductivity which is the most highly variable physical properties of rock and minerals. Consequently, EM techniques represent an exciting and challenging class of experiments with which to examine the structure, state and composition of the crust and upper mantle.

The EM methods which have been traditionally applied for sounding the deep crust use the temporal variations of the natural fields to image the conductivity structure of the earth. The principal reason for this is that natural fields are essentially plane waves in the mid-latitudes and have sufficient energy at long periods to generate a detectable response from very deep structure. However, the use of natural source fields has at once benefits as well as problems. There are low energy regions in the natural source frequency spectrum and the signal levels can change dramatically over a relatively short time span making data acquisition demanding and time consuming (Boerner 1992). As well, the large spatial extent of the plane wave fields produces response in the data from structures at some horizontal distance from the receiver location. Such lateral responses, when coupled with uncertainties about both the source field characteristics and geology, complicate the already difficult task of data interpretation.

2.2. SUBSURFACE RESISTIVITY

Information about resistivity variations beneath the seafloor is crucial in offshore hydrocarbon exploration. Although various electromagnetic methods for remote mapping of resistivity in marine environment exist (Chaveet al., 1991), until recently, sub-seafloor resistivity data in the oil and gas industry were obtained almost exclusively by wire-line logging of wells.

Resistive variations in rocks are generally controlled by the interplay between highly resistive minerals (1011 - 1014 Ωm) and pore fluids including low resistive saline water (0.04 - 0.19 Ωm) and/or infinitely resistive hydrocarbons (S. E. Johansen et al., 2005). Tight crystalline rocks such as oceanic crust typically show high resistivities (100 – 1000 Ωm) with variations mainly controlled by saline fluids in fracture networks. Sedimentary rocks can exhibit a wide range of resistivities (0.2 – 1000 Ωm) mainly controlled by variations in porosity, permeability and pore connectivity geometries in addition to pore fluid properties and temperature. The high resistivity of hydrocarbon filled reservoir rocks (30 – 500 Ωm) compare to reservoirs filled with saline formation water (0.5 – 2 Ωm) makes EM sounding a potential tool for detection of subsurface hydrocarbon.

2.3. ELECTROMAGNETIC SOUNDING FOR HYDROCARBON EXPLORATION

Over the years, EM techniques have been used in the oil and gas exploration and production companies for exploration purposes. Magnetotelluric and controlled source electromagnetic (CSEM) survey are the electromagnetic sounding techniques that have found extensive application in hydrocarbon exploration industry. These deep reading EM survey methods provides distinctly different insights into the subsurface and are basically used for examination of subsurface resistivity or its inverse the conductivity, providing information that is complementing to seismic data. However, because MT current within the earth are generated mostly in the horizontal plane and the MT fields attenuate with depth, thin sub-horizontal resistive formations are almost invisible to the magnetotelluric method thus the technique alone is not useful for hydrocarbon fluid detection (J. Brady et al., 2009). Owning to this limitation of the magneto-telluric sounding, attention has been diverted to the controlled source electromagnetic (CSEM) as a better technique for delineating thin formations.

2.4. CONTROLLED SOURCE ELECTROMAGNETIC (CSEM) TECHNIQUE

Controlled source electromagnetic methods are an attractive complement or alternative to natural source soundings in some circumstances (J. M. Reynolds, 2011). They are a commonly used way to obtain information about the electrical conductivity or resistivity of the subsurface of the earth which have been used for geophysical applications for many decades. Different earth materials have resistivity across multiple of magnitude and controlled source electromagnetic techniques are used to map and differentiate these materials based on that contrast. All CSEM methods utilize an active, or man-made, ac electromagnetic transmitter source to induce a secondary current in the subsurface and are attractive compliment or alternative to so-called “passive-source” electromagnetic methods such as magneto-telluric which rely on naturally occurring electromagnetic fields (C. M. Swift 1991).

In frequency-domain CSEM, the secondary current is induced by driving an alternating current at a particular frequency through a coil or long grounded wire. This creates a primary magnetic field, which in turn induces secondary currents as it propagates through the earth and changes with time. In time domain CSEM, a large transmitter loop is laid out on the ground and most commonly a square-wave current is run through it. When the current abruptly goes to zero, in accordance with faraday’s law, a short-duration voltage pulse is induced in the ground, which causes a loop of secondary current to flow in the immediate vicinity of the transmitter wire. These secondary currents in turn creates secondary magnetic and electric fields as they propagate and decay. Receivers placed some distance away from the source record various components of the electromagnetic fields produced. In most frequency-domain surveys, these receivers measure both the primary fields from the transmitter and secondary responses from the earth. As most time-domain receivers take their measurement when current is not flowing in the transmitter, the receiver will measure only the secondary fields.

Controlled source electromagnetic methods are relatively quick in terms of collecting data, depending on the strength of the source and the desired depth of investigation and have been employed on land, airborne systems and underwater (marine CSEM) for hydrocarbon exploration and detection of oil and gas (Sundberg, 1930; Constable and Srnka, 2007), mineral prospecting (Wait, 1951), hydrological and environmental surveys (Palacky et al., 1981; Osella, 2005) and in archaeology (Tite and Mullins, 1970; Osella, 2005).

2.4.1. MARINE CONTROLLED SOURCE ELECTROMAGNETIC (MCSEM) METHOD

With the success of the controlled source electromagnetic (CSEM) technique in onshore mining exploration, the technique was expanded into new applications for hydrocarbon exploration, initially in deep water (500 meters or more) and more recently, in shallower water less than 500 meters (Peace et al., 2004). The application of controlled source electromagnetic (CSEM) technique in offshore and marine environment is termed marine controlled source electromagnetic (mCSEM) or seabed logging as commonly used in the industry. The basic idea behind the use of controlled source electromagnetic

(CSEM) for offshore hydrocarbon exploration is to identify resistive layers in an otherwise conductive environment (J. Brady et al., 2009).

The new marine controlled source electromagnetic (mCSEM) method, although superficially similar to magnetotelluric, is different and uses an artificial electric dipole energy source instead of recording passive earth energy. This improves the resolution of the method by about an order of magnitude and permits the identification of thin, high-value resistors in a background matrix of low-resistivity conductor rock, down to tens of meters rather than the hundreds of meters typical of passive marine magnetotelluric resolution. With offset information from, for example, a nearby discovery well, the marine controlled source electromagnetic method can identify a target hydrocarbon-bearing reservoir rock in a structure before it is drilled (Peace et al., 2004). However, there are several methodological limitations regarding both acquisition operation and interpretation approaches (P. Dell'Aversana 2010). Intrinsic limitation of lateral and vertical resolution derive from the fact that marine controlled source electromagnetic is a low-frequency EM method and in practice receivers consist of standalone multicomponent stations deployed on the seafloor with spacing that ranges from several hundred meters to greater than 1 km thus good lateral resolution with such sparse recording stations is difficult to provide. The method also has intrinsically low lateral resolution because of its interpretation which is often based on the analysis of amplitude (and phase) versus offset data, observed over a large range of source-receiver distances.

2.4.1.1. ACQUISITION METHOD

The basis of the approach is the use of a mobile horizontal electric dipole source (Young and Cox, 1981) and an array of seafloor electric field receivers. The horizontal electric dipole (HED) is towed close to the sea bed emitting an ultra-low frequency (typically a few tenths to a few tens of hertz, approximately 0.1 Hz to 10 Hz) electromagnetic (EM) signal that diffuses outwards both into overlying water column and downward into the sea bed where it is recorded by the stationary seabed receivers as shown in Figure 1 below. It relies on the large resistivity contrast between hydrocarbon-saturated reservoirs, and the surrounding sedimentary layers saturated with aqueous saline fluids. Hydrocarbon reservoirs typically have a resistivity of a few tens of ohm-meter or higher, whereas the resistivity of the over and underlying sediments is typically less than a few ohm-meter thus making marine controlled source electromagnetic (mCSEM) method an excellent discriminator between high-hydrocarbon-saturation economic reservoirs and low-hydrocarbon saturation non-to low-economic reservoirs (Peace e al., 2004).

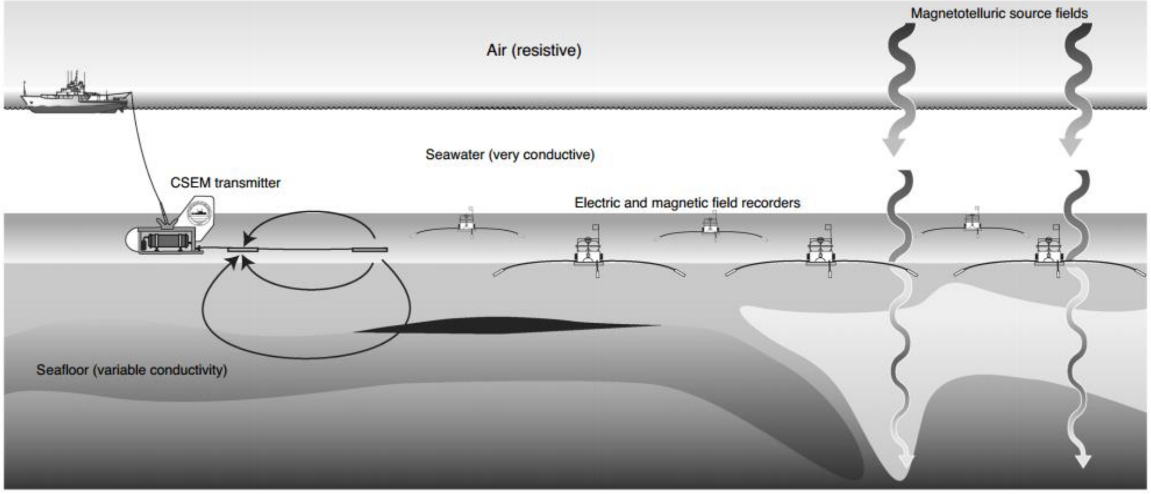

Figure 1. Schematic representation of the horizontal electric dipole-dipole mCSEM method.

The figure shows an electromagnetic transmitter being towed to the seafloor to maximize the coupling of electric and magnetic fields with seafloor rocks. These fields are recorded by instruments deployed on the seafloor at some distance from the transmitter. Seafloor instruments are also able to record magnetotelluric fields that have propagated downwards through the seawater layer. Source: (Steve Constable & Leonard J. Srnka, 2007).

The rate of decay in amplitude and the phase shift of the mCSEM signal are controlled both by geometric and by skin depth effects. Because in general, the seabed is more resistive than seawater, skin depths in the seabed are longer. As a result, electric fields measured at the seafloor by a receiving dipole at a suitable horizontal range are dominated by the components of the source fields that have followed diffusion paths through the seabed. Both the amplitude and phase of the received signal depend on the resistivity structure beneath the seabed thus a survey consisting of many transmitter and receiver locations can therefore be used to determine a multidimensional model of sub-seafloor resistivity (T. Eidesmo et al., 2002).

2.4.2. PATHS FROM MARINE SOURCE TO RECEIVERS

As illustrated in Figure 2 below, seabed receivers record the electromagnetic responses as a combination of energy pathways including signal transmission directly through seawater, reflection and refraction via the seawater-air interface, refraction and reflection along the seabed, and reflection and refraction via possible high resistivity subsurface layers. Low frequency electromagnetic (EM) signals decay exponentially with distance z (m) by $e^{-z/\delta}$ where $\delta = (2 \bullet \rho\ /(8 \bullet 10^{-7} \bullet \pi^{2} \bullet \mathrm{f}))^{1/2}$ and ρ and f denote resistivity (Ωm) and signal frequency (Hz) respectively. The distance required to attenuate an EM signal by the factor e^{-1} (0.37) is defined as the skin depth and is about 551 m in seawater (0.3 Ωm), 1424 m in 2 Ωm sediment and 10^{8} m in air (1010 Ωm) for a 0.25 Hz signal (S. E. Johansen et al., 2005).

Electromagnetic signals are rapidly attenuated in seawater and seafloor sediments saturated with saline water, and these signal pathways will dominate at near source-to-receiver offsets (~ 3 km). The strength of the signal decreases rapidly with distance because of its attenuation in conductive water. Another contribution comes from the airwave. The electromagnetic field travels to the water surface, where it encounters highly resistive air. The resistance contrast forces the wave propagation to follow the air/water interface and energy is reflected and refracted via this interface. This energy is commonly termed the air-wave and dominates at far offsets (~ 6 km) depending on water depth, because unlike the signals following other paths, the signal at the air-water interface has little attenuation.

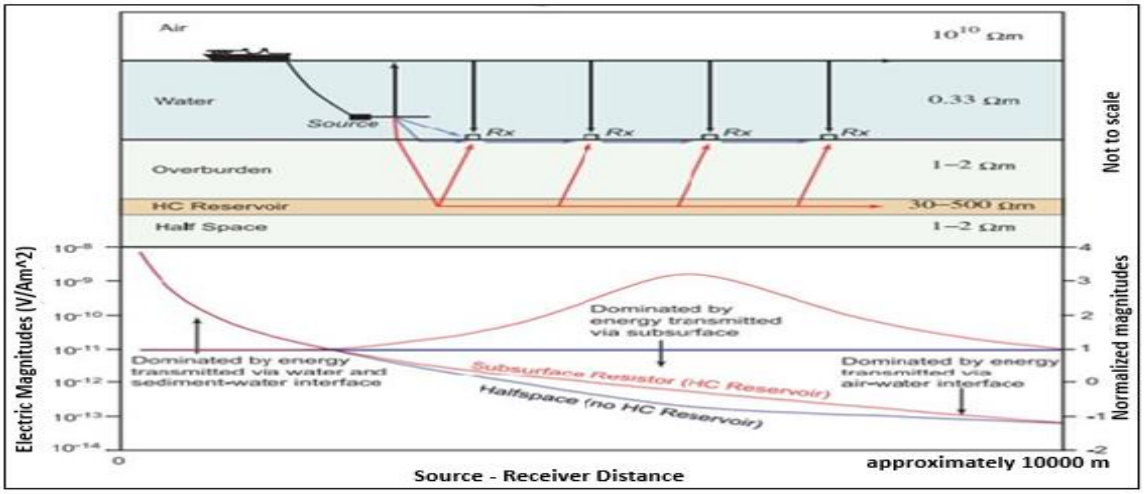

Figure 2. Schematic sketch of air/water-sediment geometry and receiver (Rx) layout on seabed during towing of electromagnetic source.

(Top) Typical resistivities of air, water, sediments and hydrocarbon reservoirs are shown for reference. Black arrows denote refracted transmission of electromagnetic signals via air/water interface. Blue arrows denote direct transmission of electromagnetic signals through water and by refraction along the seabed. Red arrows denote refracted transmission of electromagnetic signals via a buried high-resistivity layer (hydrocarbon reservoir). (Bottom) Electric magnitudes measured at a single receiver as a function of source-receiver distance. Red curve show the expected response from a model including a high-resistivity hydrocarbon reservoir. Blue curve is the significantly weaker response from a model without hydrocarbon reservoir. Source: S.E. Johansen et.al. (2005).

In high resistivity and relatively thin (20-200 m) subsurface media, such as hydrocarbon filled reservoirs (30-500 Ωm), the energy is guided along the layers and attenuated less depending on the critical angle of incidence (Kong et al., 2002). Guided EM energy is constantly refracted back to the seafloor and is recorded by the EM receivers. The refracted energy from high resistivity subsurface layers will dominate over directly transmitted energy when the source-receiver distance is comparable to or greater than the depth to this layer. Since the waves propagates more easily through a resistive than a conductive formation, the presence of a reservoir enhances the received signal compared to a uniform subsurface lacking a resistive layer. The detection of this guided and refracted energy is the basis of marine controlled source electromagnetic (mCSEM) method (S. T. Ellingsrud et al., 2002).

2.5. GENERAL THEORY OF ASYMMETRY

Marine controlled source electromagnetic technology presently being utilized for the direct detection and characterization of possible hydrocarbon bearing prospects has given exploration companies a cutting edge to discover new oil and gas fields both in shallow and deep water environment at a time when the large and easy to produce fields are diminishing. Transition into deep water settings has forced geoscientists to be more certain of the presence and position of hydrocarbon especially in deep water settings where the costs to drill exploratory wells can reach in excess of 100 million dollars. Methods to properly explore and analyze offshore marine controlled source dataset would aid the understanding of the acquired data and subsequently its interpretation, providing geoscientists with a high level of certainty about the presence and lateral limits of a resistive body buried in the subsurface. The method exploited in this thesis as explained in this chapter, when duly implemented serves as a fast imaging indicator of resistive anomaly which can be combined with modern seismic to lower prospect drilling risk.

In a frequency domain seabed marine controlled source electromagnetic acquisition, the signals (electric and/or magnetic field) recorded as a function of offsets at each receiver station/gather are called magnitude versus offset (MVO) and phase versus offset (PVO) plots. The attenuation trend of the measured fields versus offset depends on the resistivity distribution in the space between the actual source position and the receiver location and its depth of penetration is proportional to offset. A fundamental characteristics of the marine controlled source electromagnetic data is the possibility to distinguish, at each receiver position, an in-towing and an out-towing part of the data which corresponds respectively to the response recorded for decreasing source-receiver distances i.e., when the source approaches the receiver and for increasing source-receiver distances, when the source goes far away from the receiver.

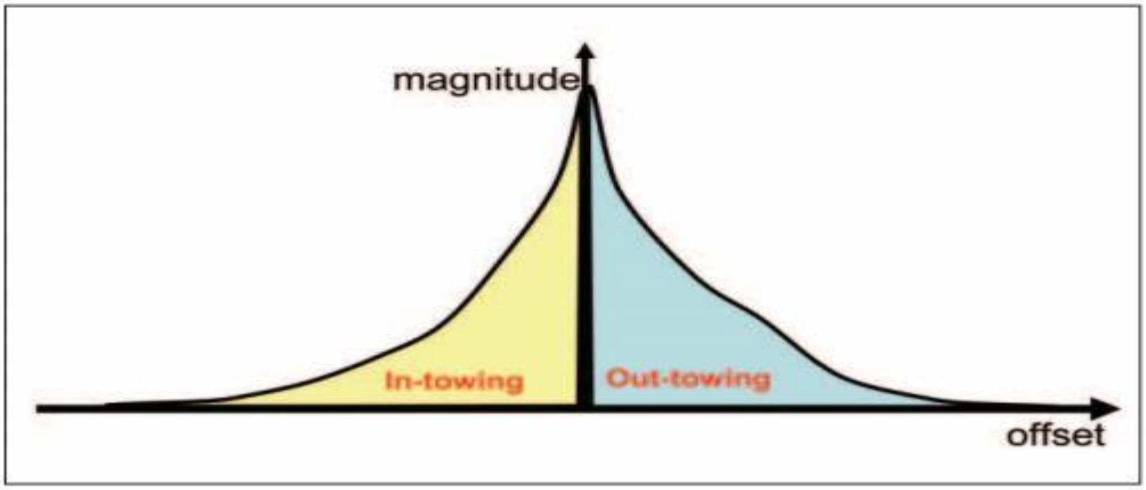

Figure 3. Conceptual representation of marine CSEM data as magnitude versus offset.

On the vertical direction the electric field is represented; the horizontal direction is the distance between source and receiver. In-towing and out-towing correspond, respectively, with the response recorded for decreasing source-receiver distance (when the source approaches the receiver) and for increasing source-receiver distances (when the source goes far away from the receiver). Source: P. Dell'Aversana & F.Zanolleti, 2008.

The level of symmetry between the decreasing source-receiver distance (in-tow) and the increasing source-receiver distance (out-tow) is an important property of the receiver gather, which depends on the resistivity distribution. In the case of a half space, uniform or a symmetrical resistivity distribution to either side of a receiver, both the magnitude versus offset (MVO) and phase versus offset (PVO) plots will be perfectly symmetrical with respect to the vertical axis at the receiver position, assuming flat seafloor topography. On the contrary, if a lateral resistive discontinuity exists due to resistive body on one side of the receiver, in-towing and out-towing data will not be symmetrical and the electric (or the magnetic) response versus offset will reflect the presence of the resistive variation with different attenuation trends for the in-towing and out-towing data respectively.

The level of symmetry associated with the recorded electric and/or magnetic field at each receiver gather as a function of offset, i.e., magnitude versus offset and phase versus offset in a marine controlled source electromagnetic (MCSEM) acquisition are represented by an electromagnetic attribute dubbed “asymmetry attribute”. The attribute is a unique parameter that represents a measure of asymmetry between in-towing and out-towing data and it’s expected to be zero in the case of a perfect symmetry in both sides of the receiver gather. On the contrary, it will have maximum absolute values above resistivity discontinuities thus if a receiver line crosses a resistive discontinuity, the maximum asymmetry between in-towing and out-towing data will appear at the nearest receiver with respect to the discontinuity while the other receivers will show an asymmetry progressively decreasing for increasing distances from the lateral discontinuity.

In a complex situation which is usually characterized by multiple resistive layers, to properly locate and estimate the distribution of the discontinuities or multiple stacked resistors, complicated by lateral discontinuities i.e., resistive gaps at different depths, the attribute is computed for multiple frequency values at different offset. The driving principle is that the higher is the frequencies, shorter is the maximum useful offset, and shallower is the source of the asymmetry or location of the anomaly.

2.6. LITERATURE REVIEW

Since its introduction as an additional hydrocarbon-exploration technique, resulting from the idea that guiding of electromagnetic energy in hydrocarbon reservoir is detectable (Eidesmo et al., 2002; S. T. Ellingsrud et al., 2002), marine CSEM has become an important complementary tool to seismic exploration methods in the detection and characterization of possible hydrocarbon-filled layers in sedimentary environments. The marine CSEM method was introduced by (Cox et al., 1971), and has since then been successfully applied to study the oceanic lithosphere and active spreading centres (Young and Cox, 1981; Cox et al., 1986; Constable and Cox, 1996; MacGregor and Sinha, 2000). Pioneering works and researches on the marine CSEM was carried out by Charles Cox et al., (1971), who with the understanding that marine CSEM is preferentially sensitive to relatively resistive zones under the seafloor demonstrated that the method compensates for the loss of magnetotelluric signal at deep ocean seafloor. Further details on the basic theory behind the marine CSEM method is described in (Eidesmo et al., 2002) and a summary of the first marine CSEM survey can be found in Ellingsrud et al., (2002).

Recently, there has been a rapid increase of marine CSEM survey, with relatively slower advancement in processing and interpretation methods which has led to increased efforts by academic institutions, contractors and oil and gas companies to exploit the method and its ability to measure remotely one of the most fundamental earth physical properties, electrical resistivity as it relates to hydrocarbon. Several scholars and researchers have done many works on the marine CSEM, with the aim of improving the acquisition, processing and interpretation of the acquired data from both deep and shallow marine environment.

The earliest of these recent work is that of Eidesmo et al., (2002), that verified the so called "split effect" i.e., sensitivity of different antenna configuration to thin buried resistive layers with 1-dimensional modelling. They demonstrated with 1- and 2-dimensional modelling on real data from marine CSEM survey offshore west Africa that by careful positioning of both transmitter tow tracks and receivers relative to suspected hydrocarbon bearing structure, a multidimensional model of sub-seafloor resistivity can be determined, which provides detailed information on the presence and lateral extent of the hydrocarbon reservoir.

On the contrary, (S. Constable 2005; Hesthammer et al., 2010), states that by dividing the measured electric field by the background response and/or simply normalizing by the response of an instrument assumed to be positioned off target, real mCSEM data can be interpreted. Constable concluded that application of this method at different frequencies having other skin depths will help resolve ambiguities in interpretation. On the other hand, Hesthammer et al., (2010) through assessment of the success of marine CSEM technology on hydrocarbon exploration for different wells suggested that the normalized anomalous amplitude response (NAR) is a simple and observable methodology for data analysis and interpretation. The normalization is with respect to a reference receiver from an area that represents the background resistivity profile without the targeted resistor (i.e., the hydrocarbon reservoir). A normalized response value of 1 is said to indicate that chosen receiver has exactly the same electric field magnitude for the chosen offset as the reference receiver while a NAR value of 1.5 indicates that the observed receiver has a normalized response 50% higher than the reference receiver which implies that something in the subsurface has higher resistivity than observed at the reference receiver and could potentially be a hydrocarbon-filled reservoir or something resistive.

However, (P. Dell'Aversana 2006, 2007) highlighted the limitations of marine controlled source electromagnetic interpretation when based only on the analysis of the normalize magnitude versus offset data, especially in shallow water where airwave effect masks the earth response. He proposed different electromagnetic attributes, i.e., slope of magnitude versus offsets (MVO), integral of the magnitude versus offsets (MVO) curves, the semblance with respect to a reference magnitude versus offset (MVO) trend (measured at well locations), the instantaneous frequency (phase derivative with offset) as useful quantities for quick exploring of the data which provides a synoptic view of the electric and magnetic field distribution at seafloor and their attenuation with offsets thus improving the comprehension of any given data before taking up any multidimensional inversion.

Um Schankee & Alumbaugh, (2007) examined the underlying physics of the marine CSEM method and demonstrated that the efficacy of the method for detecting high-resistivity thin layers at depth is strongly dependent on the source-receiver geometrical configuration and source-frequency range.

MacGregor et al., (2007) demonstrate that the analysis of the marine CSEM survey combined with the existing seismic data allowed a more robust and in-depth understanding of the Ernest prospect in North Fakland basin. This, they stated will help the license holder make confident decisions in its exploration process.

Avdeeva et al., (2007) extended the earlier works on marine CSEM to time domain and presented a comparative studies on the ability of the marine CSEM method to detect hydrocarbon reservoirs in both time (TDEM) and frequency domain (FDEM) utilizing signal to noise ratio (SNR) calculated at same survey configuration and model geometry. The conclusion suggests that acquisition on FDEM method is able to detect targets for source-receiver offsets from 200 meters to 7000 meters while the TDEM method can detect the reservoir over a whole range of receiver profile.

R. Mittet (2008) demonstrated that the normalized amplitude ratio used for marine CSEM data does not give a reliable and consistent diagnostic reservoir signature in different water depths. He proposed the use of modified normalized amplitude ratio which unlike the standard normalized amplitude ratio includes both the amplitude and the absolute phase of the electromagnetic fields and behaves consistently at all water depths.

James Brady et al., (2009) presented a comparative studies between the two offshore electromagnetic sounding techniques for identification of hydrocarbon deposits i.e., marine CSEM and marine magnetotelluric (MMT). They highlighted the high sensitivity of marine CSEM to resistivity contrast of thin formations and its ability to utilize multiple frequencies components at several depth and several resolution as advantage over the marine magnetotelluric technique.

Further investigations carried out by Nguyen et al., (2009) on the potentials of mCSEM technology to detect an EM anomaly in prospects with high resistive anisotropic overburden reveals that with high frequency content waveform at far offsets, resistivity anomaly can be detected below the overburden and they concluded that the ratio of the resistivity of the anomaly and the background is important for estimating hydrocarbon saturation.

P. Dell'Aversana & F. Zanoletti (2008, 2010) expanded on the suggestion on the previous literature (P. Dell'Aversana 2006, 2007) and introduced a new electromagnetic attribute termed "asymmetry attribute", which they said to be helpful for detecting properly the spatial distribution and borders of resistive layers with an accuracy that depends on the receiver spacing. They stated that the EM attribute when combined with the results of multi-dimensional modelling and inversion yields 3-D resistivity model of the subsurface.

Other methods for fast interpretation of marine controlled source electromagnetic (mCSEM) data which have been proposed in literatures includes the "Singular Function Normalization" (De Lerma et al., 2013) and the "Pseudo-image" (Andrea Gola and Giancarlo Bernasconi, 2014)

The SFN method is based on determining on the MVO (magnitude versus offsets) curve the best-fit estimates of the exponent coefficients of the exponential singular functions and of the exponents of the Lipschitz singular function which aids definition of areas where higher values of resistivity occur in the underground.

The proposed Pseudo-image method which was demonstrated on a synthetic model is estimated by representing in pixels, computed magnitude (in log10 scale) of the difference between the inline electrical field component (amplitude and phase) produced by models with and without a resistive anomaly at a certain source receiver pair so as to highlight the deviation of the curves of the models which indicates the presence of a resistive anomaly.

3. APPLICATION OF ASYMMETRY TO CSEM DATA

In this chapter, the two mCSEM datasets utilized for the analysis and their simulated and hypothesized models are duly introduced and described. Subsequently, the processing steps implemented on both dataset are separately explained under subsection title corresponding to each datasets.

3.1. Data and Model Description

This thesis work was carried out on two sets of data which is similar to actual dataset from marine controlled source electromagnetic (mCSEM) acquisition. The dataset explored and processed are as follows:

- Canonical model dataset and
- GOM Benchmark Test CSEM MT Synthetic data.

3.1.1. CANONICAL DATASET

The data contains electric field components (amplitude and phase) observation from a hypothesized and simulated marine controlled source electromagnetic (mCSEM) survey. The acquisition geometry is assumed inline with 101 transmitters and receiver gathers having a spacing of 200 meters respectively.

Four marine CSEM frequencies were used for the data generation, i.e., 0.125 Hz, 0.25 Hz, 0.5 Hz and 1 Hz and transmission is assumed to be from a horizontal electric dipole (HED). It contains information about the coordinates and locations x; z (in meters) of transmitters (Tx) and receivers (Rx) in the subfields.

The amplitude of the electric field (Ex) for each receiver is in linear scale and the simulated data contains both an anomalous part of the amplitude component of the electric field and that without anomaly which is referred to as background. The data is totally devoid of noise and the amplitude of the electric fields are in units of V/Am^2 while the phase are in degrees.

3.1.2. CANONICAL MODEL

The model used for the data generation is a simple 2.5D resistivity model consisting of an upper air layer which is about 0.35 km mean sea depth (using bathymetry from a real dataset) and a homogenous half space with resistivity (ρ) = 1 Ωm. A 0.1 × 2 km resistive anomaly with resistivity (ρ) of 100 Ωm is placed inside the half space with its upper boundary at around a depth of 0.5 km from the lowest bathymetry point.

The resistivity model is assumed to be along a hypothetical marine CSEM towing line crossing one resistor embedded in a layered overburden. The seabed, the buried resistive anomaly/body in the conductive half space and the inline positions of the receivers (in km) are shown in Figure 4.

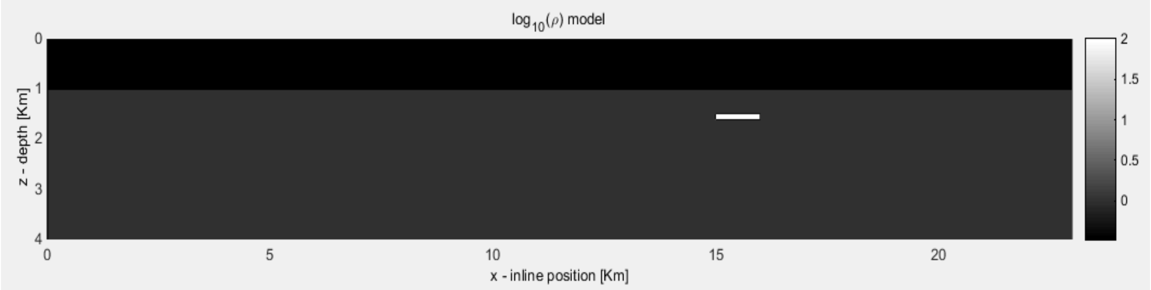

Figure 4. Resistivity model of subsurface with one anomaly.

Further description of the resistivity model and its ability to represent reality in the subsurface (in this case the synthetic scenario) is achieved by considering some receivers within and outside the area and/or lateral extent of the highly resistive body in the subsurface.

Assuming no knowledge of the lateral extension of the embedded resistor, receivers are selected (Rx10, Rx35, Rx75 and Rx76 are considered in this case) and there recorded observations, i.e., uniform background and anomalous responses superimposed and represented in plots called magnitude versus offsets (MVO) plots/profiles as shown in Figure 5, Figure 6, Figure 7 and Figure 8.

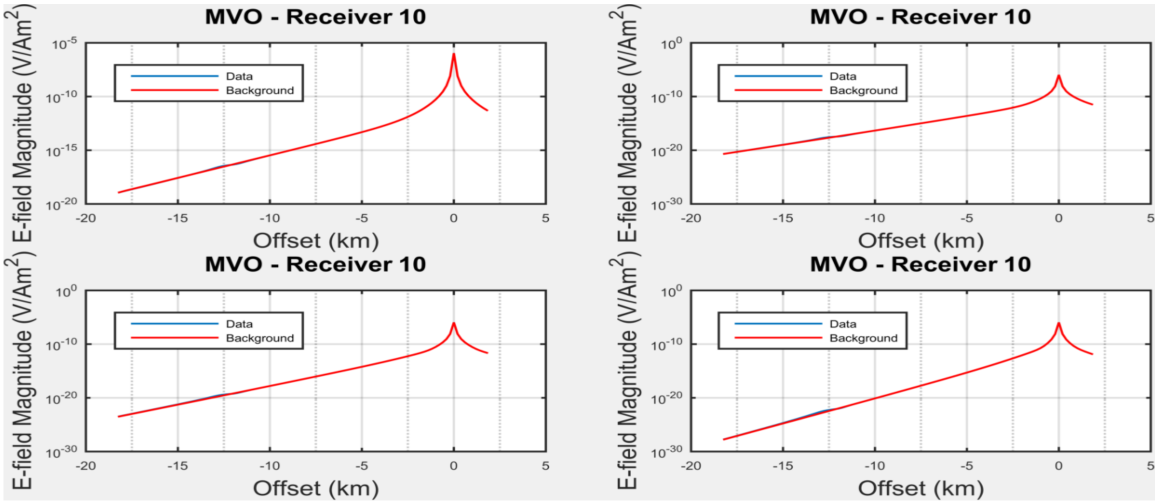

Figure 5. MVO of Rx10 showing the background and the resistive anomalous data. (Top left) MVO at 0.125 Hz (Top right) MVO at 0.25 Hz (Bottom left) MVO at 0.5 Hz (Bottom right) MVO at 1 Hz.

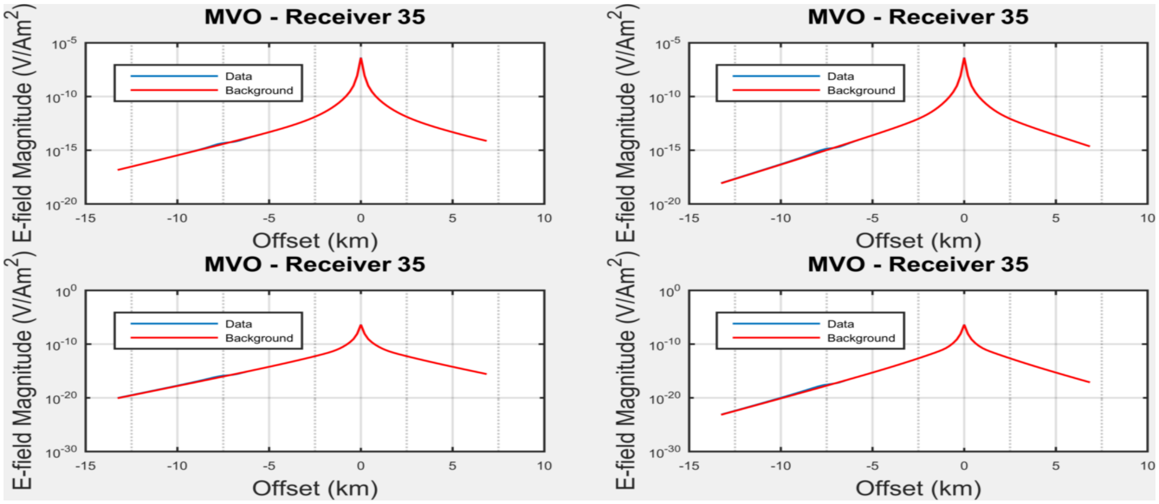

Figure 6. MVO of Rx35 showing the background and the resistive anomalous data. (Top left) MVO at 0.125 Hz (Top right) MVO at 0.25 Hz (Bottom left) MVO at 0.5 Hz (Bottom right) MVO at 1 Hz.

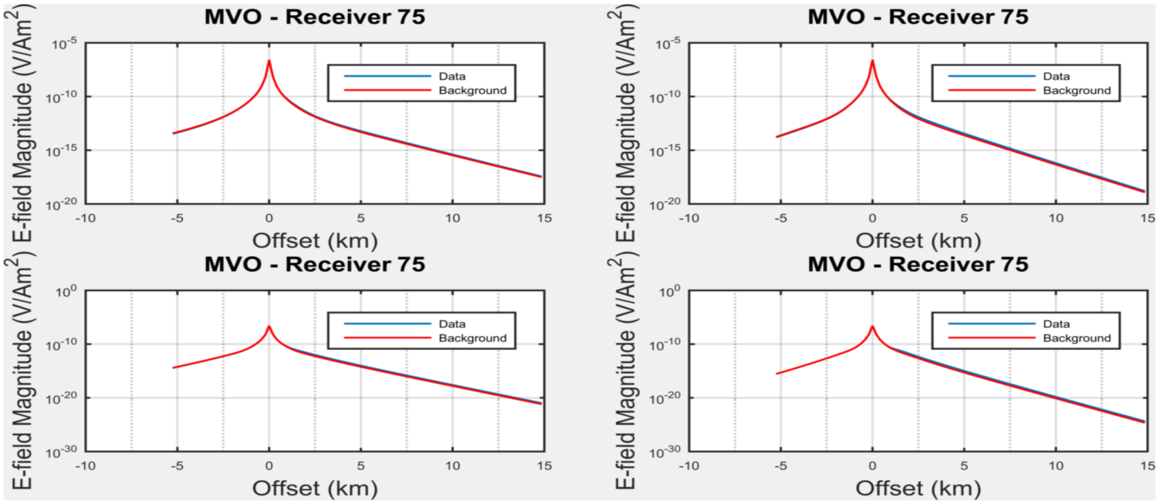

Figure 7. MVO of Rx75 showing the background and the resistive anomalous data. (Top left) MVO at 0.125 Hz (Top right) MVO at 0.25 Hz (Bottom left) MVO at 0.5 Hz (Bottom right) MVO at 1 Hz.

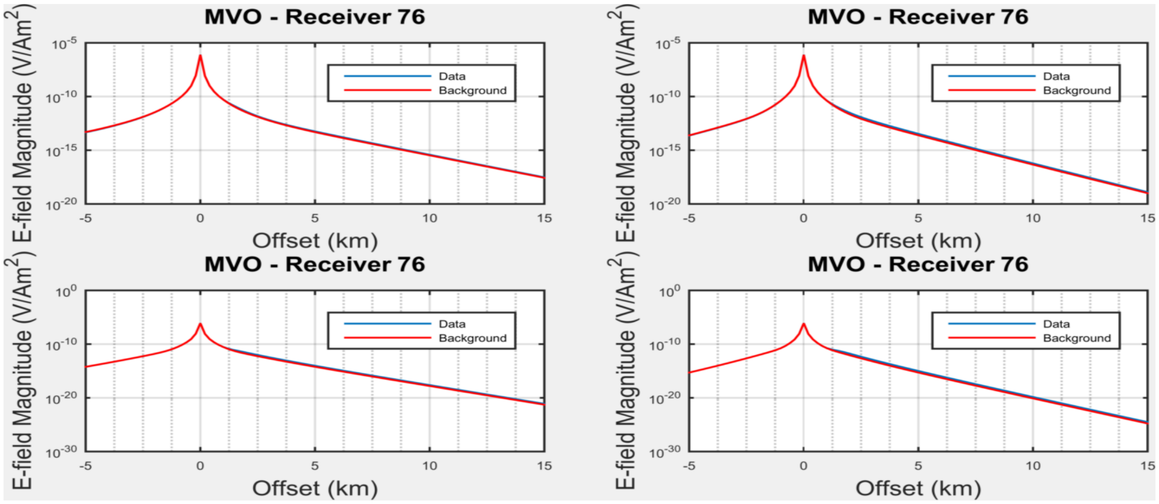

Figure 8. MVO of Rx76 showing the background and the resistive anomalous data. (Top left) MVO at 0.125 Hz (Top right) MVO at 0.25 Hz (Bottom left) MVO at 0.5 Hz (Bottom right) MVO at 1 Hz.

Table 1 Synthetic Receiver index with their inline position along x-[km]

Receiver (Rx)	*Rx inline Position 'meters' (Km)*
10	3300 (3.3)
35	8300 (8.3)
75	16300 (16.3)
76	16500 (16.5)

Table 1 above shows the inline positions of the considered receivers, with the highlighted receivers (Rx75 and Rx76) corresponding to the receivers MVO plots (Figure 7 and Figure 8) that shows a conspicuously noticeable trend of the resistive anomaly. It's expected that these receivers with conspicuous resistive anomalous trend crosses or are within the area of influence of the subsurface resistive body. Moreover, the inline positions of Rx75 and Rx76 (Table 1) are within the location of the buried resistor as seen in the resistive model of the subsurface in Figure 4.

3.1.3. GOM BENCHMARK DATASET

The GOM Benchmark Test CSEM MT Synthetic data is a more realistic dataset, which has a file format corresponding to the format used by Scripps Institution of Oceanography and made available by Chevron Corporation. The data contains electric field components (amplitude and phase) observation from both marine controlled source electromagnetic (mCSEM) survey and marine magneto-telluric (MMT) acquisition.

It is a raw synthetic data with added synthetic noise, both a random Gaussian noise (3%) and an additional geometry uncertainty (computed following Myer et al. 2012) thus allowing for the following uncertainty in the acquisition geometry: 3 degrees in receiver orientation, 1 degree in transmitter dip, 1.5 degrees in transmitter azimuth, 2 m in transmitter depth, 10 meters in inline distance. A noise floor of 10^-15 V/Am^2 for CSEM and 5% error for the MT is used and with the same co-ordinate system as the seismic.

The data contains information about the x; y; z (meters) locations of the transmitters and positions of receivers i.e., their rotation angle (degrees clockwise from x), dip angle (degrees positive down), the type of transmitter and optionally the name assigned to each transmitter and receiver. Assuming point electric dipoles (e-dipole). It has been assumed that all data responses have been normalized by the transmitter dipole moment (i.e., divided by Am), so each transmitter is considered a unit dipole.

Five marine CSEM frequencies were used for the data generation, i.e., 0.06 Hz, 0.18 Hz, 0.25 Hz, 1.25 Hz and 2.25 Hz respectively. The data contains marine CSEM phase (Ey), log10Amplitude (Ey) and magnetotelluric phase Zxy, 2D TE mode, phase

Zyx 2D TM mode, log10 Apparent Resistivity Zxy, 2D TE mode and log10 Apparent Resistivity Zyx, 2D TM mode.

Electric fields are in units of V/Am^2 for CSEM data from electric dipoles. For MT data, the impedances are in units of ohms, apparent resistivities in units of linear ohm-m and phases in degrees.

It should be noted that the thesis work focuses on marine CSEM thus as explained further in this chapter, the magnetotelluric part of the data is not considered during processing.

3.1.4. GOM BENCHMARK DATASET MODEL

Since the true model of the GOM benchmark dataset is not available and there is need to understand whether the observed trend in the signal signature of the asymmetry attribute profile of the receivers is as a result of a buried resistor and/or resistive body or it is being caused by other factors such as the sea undulation owning to water current (causing ocean induced fields), air-wave effects and dipole arm vibration. Water bottom channels, canyons and sloping or having the target sit above the water bottom when surveying off a shelve edge can also influence the survey (Pethick 2008). Bathymetry is one of the biggest factor influencing detectability in marine controlled source electromagnetic survey (mCSEM), as it usually influences the onset of airwave which may mask the hydrocarbon response, thus in place of the unavailable dataset model, the bathymetry of the seabed is shown and compared with the asymmetry attribute profile below in Figure 9 and Figure 10. Also, for clarity and better understanding of the subsurface of the simulated acquisition geometry, the transmitter trajectory, a line following the bathymetry at lower depth of approximately 30 meters of mean difference is also shown below in Figure 11.

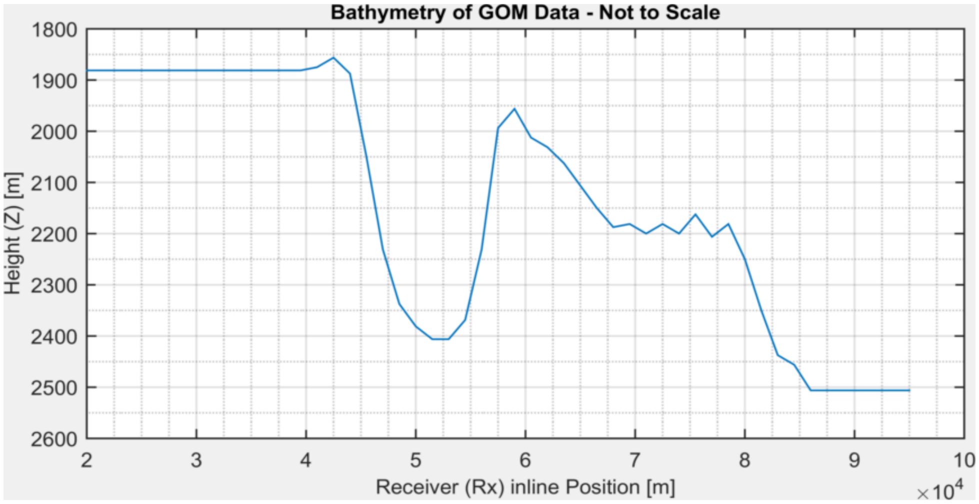

Figure 9. Bathymetry of the simulated GOM data seabed.

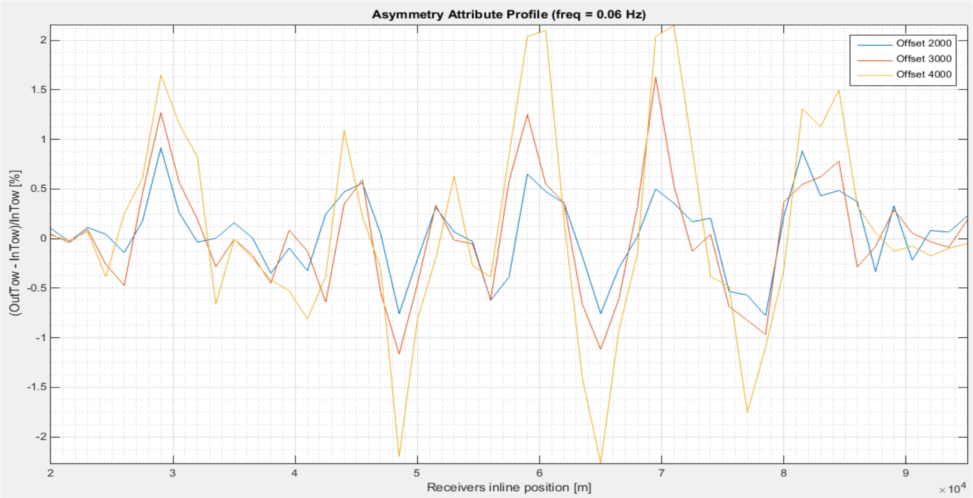

Figure 10. Inline electric component asymmetry attribute at 2 - 4 km offset for 0.06 Hz.

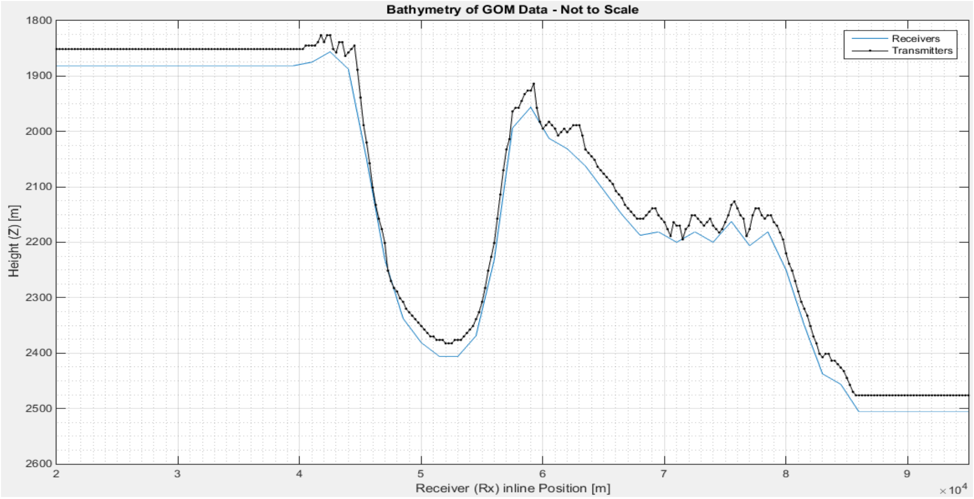

Figure 11. Bathymetry of the simulated GOM data seabed showing transmitters trajectory.

The idea behind considering the seabed bathymetry is that just like the true model, it represents reality to a reasonable level thus it is expected that the signal signature of the asymmetry profile of the inline receivers (Rx1 to Rx51) as shown in Figure 10 will exactly match the bathymetric plot, if compared or superimposed over each other, i.e., in a situation where the trend is caused by the sea bottom inhomogeneity. Otherwise, the difference between the plots under comparison (bathymetry plot and asymmetry attribute profile) will be evident, which implies that something in the subsurface, most probably a resistor and/or a resistive body contributes or causes the noticeable trend in the signal signature of the asymmetry attribute profile as can be seen in Figure 9 and Figure 10.

From the analysis of the hypothesized models of both the canonical model data and GOM benchmark dataset (i.e., resistivity model and seabed bathymetry respectively), we now have a better understanding of the possible causes of the trend in the signal signature of the asymmetry attribute profile thus will proceed with the full data processing and at the end make an informed interpretation of the results.

3.2. DATA PROCESSING

Generally, the data (Canonical and GOM benchmark datasets) was explored and processed specifically with the aid of a high performance language for technical computing, the computer Programme MATLAB. A special processing approach for handling and analyzing marine CSEM data is duly implemented on the canonical and GOM benchmark dataset respectively, following the under listed and explained sequence of steps.

3.2.1. CANONICAL DATA PROCESSING

The data processing involved the following duly explained sequence of steps.

3.2.1.1. Data Partitioning

The MATLAB algorithm implemented in this processing step separates the electric field data with no resistive anomaly (termed the background) from the electric field data with resistive anomaly, creating a structural array of the partitioned data in a way that each contains detailed information of the electric field components at each receiver (101 receivers in this case) and at each of the utilized frequencies.

Also, it separates the vector of receivers and transmitters, creating a structural array of the receivers and transmitters inline position and height, x and z coordinates respectively.

3.2.1.2. Electric field components Extraction

The implemented algorithms accesses the previously created structural array of the background and resistive anomalous field data, extracting their corresponding electric field components i.e., amplitude (in linear scale) and phase (in degrees) at each receiver and specified frequency. The expected output is amplitude with anomaly, amplitude with no anomaly, phase with anomaly and phase without anomaly.

3.2.1.3. Computation of Rx-Tx Distances

Here, the implemented algorithm, individuates each receiver alongside the transmitters which it responds to. The transmitters emitting electric field to each receiver are identified and the offsets (i.e., distances) between the inline position of each of the 101 receivers and the inline position of these transmitting sources are computed with the following underlying computational formula

$$\text{Offset (TxiRxi)} = \text{Transmitter inline position} - \text{Receiver inline position (in meters)}$$

Where "Tx" is transmitter/s of interest, "Rx" is receiver of interest and "i" is the transmitter and receiver index.

Figure 12 below is a pictorial example of Rx-Tx distances. The receiver labelled Rx1 responds to electric field generated from Tx1 to Tx5 thus the offset is computed with respect to Rx1 and each of Tx1 to Tx5.

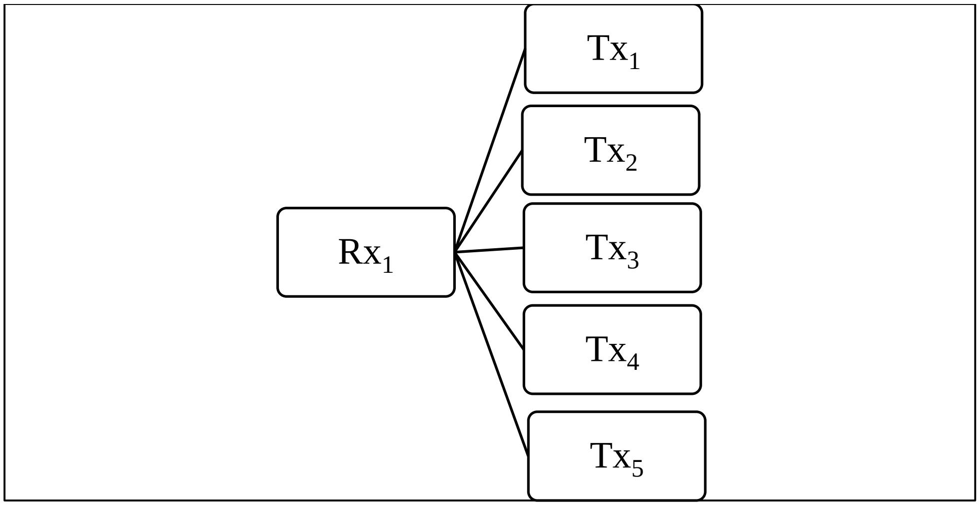

Figure 12. Example of a receiver responding to electric field signals from different transmitters.

3.2.1.4. Electric field (Ex) Magnitude profiling

Selecting a specified fixed range of offsets, information about the resistive anomalous amplitude and the background amplitude (without resistive anomaly) component of the electric field observation corresponding to the offsets that falls within the selected range is extracted and subsequently plotted, superimposing the observations. These plots which are mirror images of the electric field behaviour of the subsurface with and without the presence of resistive anomaly at each receiver is generated at the four different frequencies used in the simulated marine CSEM acquisition.

3.2.1.5. Asymmetry Attribute Extraction

The implemented algorithm divides the magnitude versus offset (MVO) plot of each receiver into two parts; a negative part which corresponds to the in-towing data (when the source approaches the receiver) and the positive part which corresponds to the out-towing data (when the source leaves the receiver). By defining different offsets of interest, short and long respectively, amplitude/magnitude of the electric field corresponding to the specified offsets are extracted and the difference of both amplitude data computed, producing a single parameter output which is termed the asymmetry attribute.

The underling computational principle is as follows:

- Non-normalized Principle:

$$Asymmetry\ attribute = OutTow\ data - InTow\ data$$

- Normalized Principle:

$$Asymmetry\ attribute = (OutTow\ data - InTow\ data)/InTow\ data$$

Figure 13 below is an example of an MVO plot showing both the in-towing and out-towing parts of the recorded magnitude.

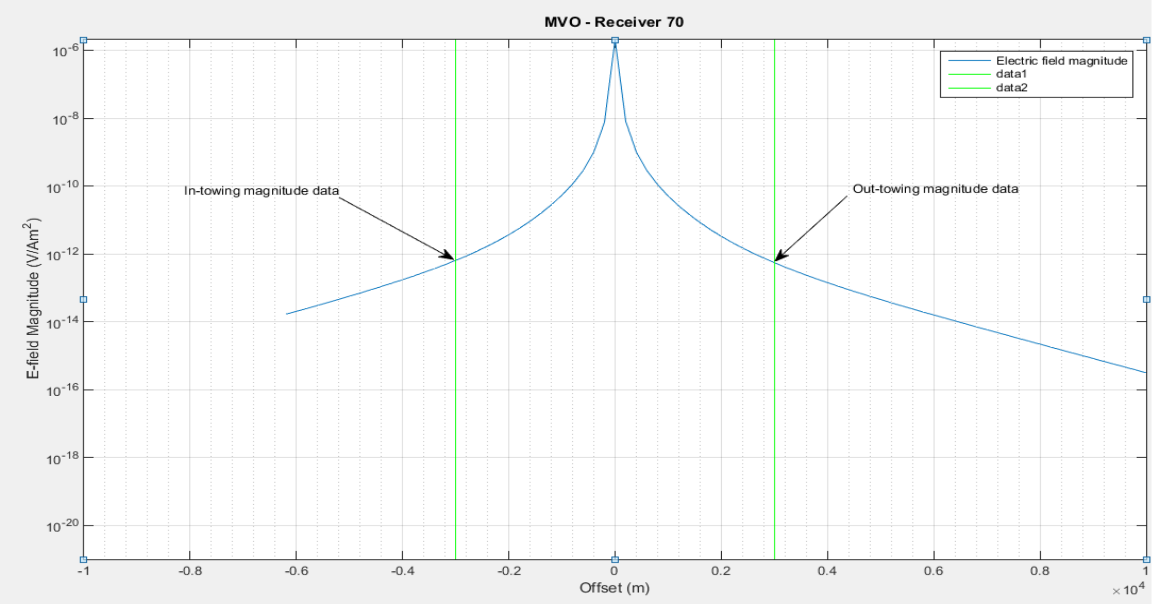

Figure 13. MVO of Rx70 showing in-towing and out-towing data.

Furthermore, the out-towing and in-towing magnitude data are normalized by computing the difference of the two and dividing by the in-towing data, expressed in percentage. The non-normalized and normalized asymmetry attribute or parameters are plotted against the receivers inline positions i.e., each parameter estimated by computations involving the magnitude versus offset of a particular receiver is plotted against the inline position of that particular receiver thus giving rise to the asymmetry or symmetry attribute profile. This asymmetry attribute profile is created at the different simulated frequencies utilized for the marine CSEM acquisition and at different offsets of interests, short and long respectively, making it possible to have a better understanding and clearer picture of the distribution of the resistivity anomaly and/or the anomalous body in either the shallow or deep subsurface layers.

3.2.1.6. Asymmetry at Integrated Range of Offsets

The implemented codes and algorithm selects a range of target offsets from a predefined offsets of interest, a combination of short and long offsets or increasing intervals of offsets, extracts and integrates the in-towing and out-towing data in the selected range of offsets and normalizes it by dividing by the integral of the in-towing data, finally producing an asymmetry attribute plot of the integrated offsets at both computational approach (non-normalized and normalized respectively). This plots are generated at different specified frequencies.

3.2.2. GOM BENCHMARK DATA PROCESSING

This dataset being much more similar to what is obtainable in reality while exploring for hydrocarbon deposits with mCSEM acquisition method, the implemented processing approach involved more steps as explained below.

3.2.2.1. PRE-PROCESSING

Most times in marine CSEM acquisition, the deployed seafloor receivers also record natural magnetotelluric fields that have propagated downward through the seawater layer. The simulated GOM benchmark dataset file as earlier mentioned in the data description contains MT data i.e., phase and apparent resistivity in TE and TM mode respectively and this part of the data has to be removed before the data processing proper.

Prior to the main data processing, the following steps were carried out on the dataset file:

3.2.2.1.1. File Reformatting

The GOM data file, originally in .data format is converted to a standard .txt format so as to enable data sorting, editing and easier processing.

3.2.2.1.2. Data Editing

The mCSEM data/observations of the GOM dataset file had discrepancies in naming convention, as some of the transmitters position and coordinates (y;z) were mislabeled as receivers and vice versa thus editing the data in the new file format was necessary to resolve the inconsistencies. The MT data and observations were deleted and the marine CSEM data/ observations were reorganized.

3.2.2.1.3. Data Sorting

The mCSEM dataset file content i.e., transmitters and receivers coordinates, frequencies and electric field observations of the phase and amplitude are sorted, partitioned and saved, each in different file for ease of usage in the subsequent actual processing.

3.2.2.2. ACTUAL PROCESSING

After the afore-mentioned preliminary processing steps were carried out on the GOM benchmark dataset, the saved clean data file was duly processed following the same steps implemented in the canonical dataset processing, i.e., computation of Rx-Tx distances, Electric field (Ex) Magnitude profiling, Asymmetry Attribute Extraction and Asymmetry at Integrated Range of Offsets. Due to the dataset very close resemblance to real dataset, the following extra processing was also implemented.

3.2.2.2.1. Data Partitioning

Since the data block in the GOM dataset is tabulated in six columns, each specifying the data type (phase and amplitude), frequency index, transmitter index, and receiver index, the data itself (electric field observations corresponding to the data type respectively i.e., phase and amplitude) and the standard error, there is need to separate each column, individuating the information contained therein. The implemented codes and algorithm specifies the unique amplitude, phase, frequencies and the number of channels occupied by different receivers and transmitters, consequently allocating each phase and amplitude to its corresponding indexes and its data observation; 44,340 recorded amplitude observation and 44,341 recorded phase observations respectively.

3.2.2.2.2. Data Structuring

In this step, the implemented MATLAB loop creates a structural array of the receivers (Rx1 – Rx51) containing information associated to the amplitude and phase at each frequency (0.06 Hz, 0.18 Hz, 0.125, 0.25Hz, and 2.25Hz). This implies that at a specific receiver (Rx index) and frequency, the array identifies the transmitters emitting signals to that specific receiver, associated distances between the transmitters and the specific receiver of interest and electric field responses recorded by that receiver, phase or amplitude depending on the electric field component one wants to access.

3.2.2.2.3. Bathymetry Profile

The implemented algorithm simply generates a diagrammatical representation of the depth of the seafloor with respect to the sea level (i.e., air-sea interface), taken at zero depth (z = 0) and increasing downwards. The output obtained which is shown in Figure 9, was achieved by inverting the predefined depth (z) and plotting the points against the predefined receiver inline positions.

3.3. Phase Processing

The phase component of the measured electric field which forms the basis of the proposed investigation being carried out in this thesis work is processed towing the under listed and explained steps.

3.3.1.1. Electric field Phase Profiling

The implemented algorithm accesses the information and data in the previously created receiver structure array of both sets of data, generating visualizable figures of the observed phase component of the electric field on y-axis and the distances (offsets) between the considered receiver and the different transmitting source/sources that the considered receiver responds to. In order to visualize the phase component observations of the inline electric field recorded by each receiver, the MATLAB algorithm is implemented in such a way that the phase versus offsets plots are generated at the different frequencies of acquisition.

3.3.1.2. Phase Component Reconstruction

The implemented algorithm compensates the numerous discontinuities of the extracted phase which was identified during the phase demodulation in the PVO plots. The wrapped phase variation usually occurs when an extreme value, of positive pi (+ π) or negative pi (- π) is reached causing a phase jump of one cycle to the other end of the interval. By defining an arbitrary starting point of mutilation at offset of 1000 meters in the phase map, the algorithm reconstructs the physical continuous phase variation by addition of positive pi (+ π) when both in-towing and out-towing data are negative and a negative pi (- π) when the in-towing and out-towing data are positive resulting to an unwrapped phase (suppressed phase jumps) with reliable information.

4. RESULTS ANALYSIS AND DISCUSSION

After duly processing the simulated mCSEM acquisition dataset, i.e., the canonical data and the GOM benchmark data, the following results which are explicitly analyzed and explained were obtained. The results presented are categorised under two subheadings corresponding to each of the processed dataset, canonical and GOM benchmark dataset respectively.

4.1. Canonical Data Results

4.1.1. MVO PLOTS ANALYSIS

The first major analysis performed on this dataset is the extraction of the magnitude component of the electric fields electromagnetic measurements and subsequent profiling against the offset (MVO) for both the background without resistive anomaly and the data with anomaly. The outcome of this processing is the superimposed mapping of the extracted magnitude/amplitude component of the electric field responses of the background and anomalous data for the grid of 101 receivers at a fixed offset and different acquisition frequencies, 0.125 Hz, 0.25 Hz, 0.5 Hz and 1 Hz. Shown below in Figure 14 to Figure 16 are some of the mapped MVO for certain receivers (Rx1, Rx50 and Rx101) corresponding to receivers at the beginning, middle and end of the acquisition geometry respectively. The trend seen in the MVO plots below are qualitatively similar to the trend in the other receivers MVO plots.

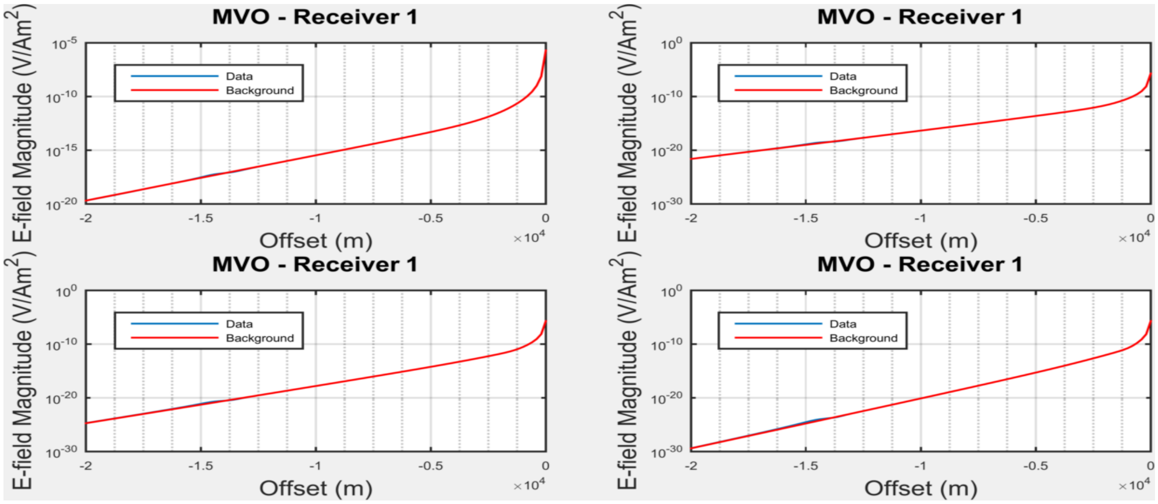

Figure 14. MVO of Rx1 showing the background and the resistive anomalous data. (Top left) MVO at 0.125 Hz (Top right) MVO at 0.25 Hz (Bottom left) MVO at 0.5 Hz (Bottom right) MVO at 1 Hz.

Relatively at all acquisition frequencies (low and high), the observed trend in the magnitude response of MVO plot of RX1 (Figure 14) shows more of the background with no or insignificant noticeable response from the resistive layer (in this case, the resistive data). This observed trend suggests that the receiver (Rx1) and most probably other receivers at the start of the acquisition line does not feel the presence of the embedded resistor or the resistive layer/body. Based on this, the resistor is not expected within the location or inline position of Rx1 and other receivers within RX1.

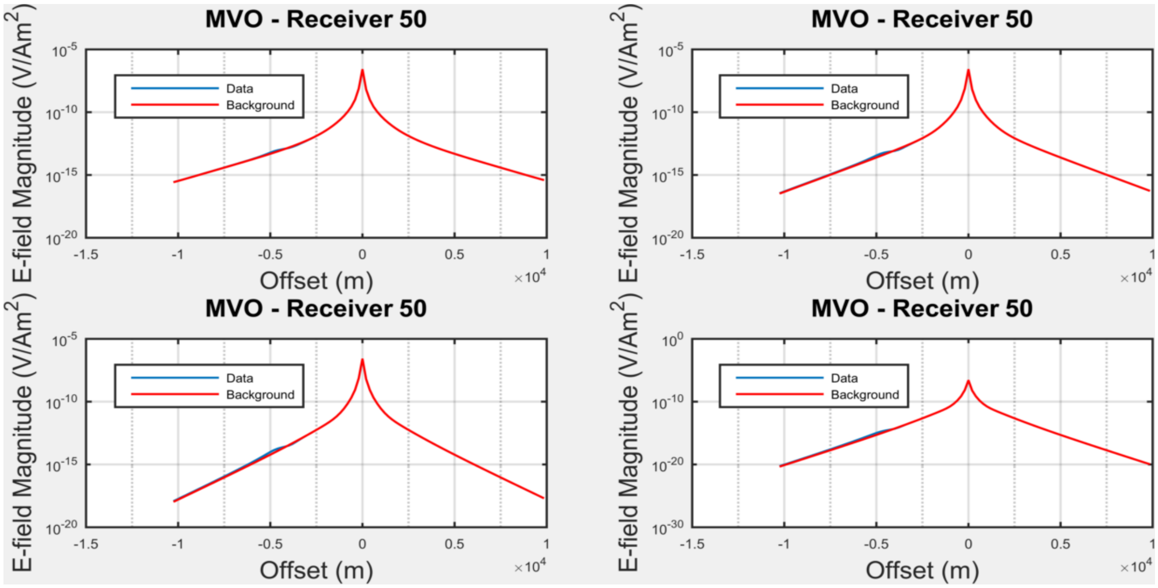

Figure 15. MVO of Rx50 showing the background and the resistive anomalous data. (Top left) MVO at 0.125 Hz (Top right) MVO at 0.25 Hz (Bottom left) MVO at 0.5 Hz (Bottom right) MVO at 1 Hz.

As the source begin to approach the middle of the acquisition line, there is a noticeable detection of the anomalous or resistive data as revealed by the MVO of Rx50 in Figure 15. The detected resistive response is seen at the in-towing part of the receiver at all frequencies which is qualitatively similar to the trend observed at other receivers within the middle of the acquisition line and/or within RX50. Based on this observation, there is a possibility that the embedded resistor will be detected by receivers within the middle of the acquisition line.

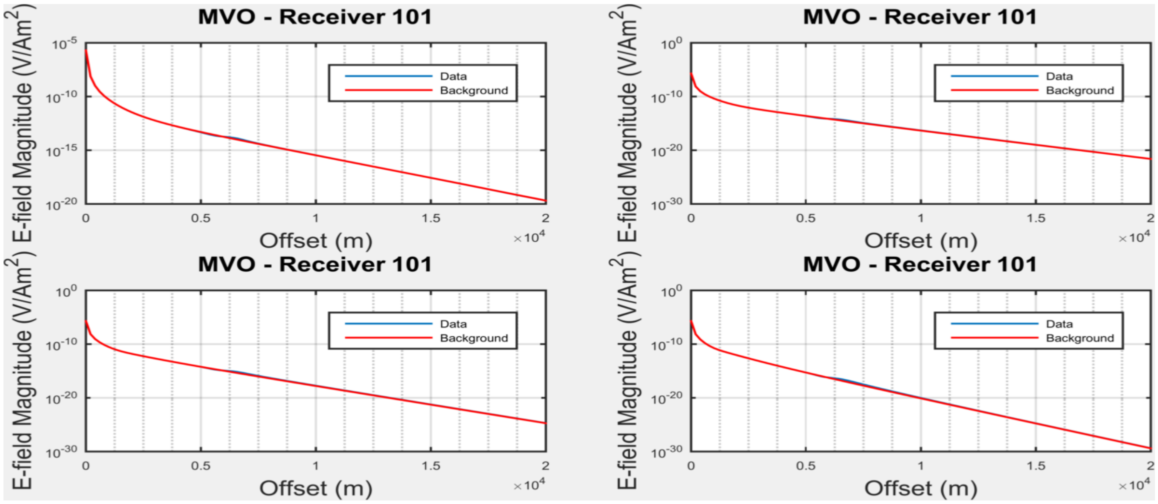

Figure 16. MVO of Rx101 showing the background and the resistive anomalous data. (Top left) MVO at 0.125 Hz (Top right) MVO at 0.25 Hz (Bottom left) MVO at 0.5 Hz (Bottom right) MVO at 1 Hz.

At the end or within the end of the acquisition line, the trend of the magnitude response is similar to that at the beginning of the acquisition line, with the MVO plot of RX101 (Figure 16) showing conspicuously the background response, with no or insignificant response from the resistive data/layer. This observed trend suggests that receiver (Rx101) and most probably other receivers within the end of the acquisition line does not feel the presence of the embedded resistor or the resistive layer/body. Based on this, the embedded resistor is not expected within the location or inline position of Rx101 and other receivers within RX101.

Generally, the smooth trend in the magnitude response of all the receivers MVO plots at all frequencies is as a result of the unavailability of noise in the simulated canonical data thus unlike what is obtainable in reality the response from the reservoir is clearly sensed without any effect of disturbances.

4.1.2. ASYMMETRY ATTRIBUTE PROFILE ANALYSIS

Prior to the analysis of the computed data asymmetry attributes and profiles, a table showing some of the receivers within the area of influence of the buried resistive body and their inline positions are presented below. Table 2 will aide understanding of the result analysis involving the receiver's inline position as discussed in this section.

Table 2. Inline positions of synthetic data receivers within lateral extent of subsurface resistor [m]

Receiver (Rx)	68	69	70	71	72	73
Rx inline Position (m)	14900	15100	15300	15500	15700	15900

The asymmetry parameter extracted and profiled against the receivers inline positions, which was obtained through further processing and analysis of the mapped MVO of the grid of receivers at each frequency (frequencies corresponds to that used in the simulated acquisition) and different offsets are presented in Figure 17, Figure 18, Figure 19 and Figure 20. These asymmetry attribute profiles which are the results of this processing step, are presented for both the normalized and non-normalized computational approach and for the lowest and highest frequencies, i.e., 0.125 Hz and 1Hz respectively. For further understanding of the response at other frequencies, attached in "appendix A" are some figures showing asymmetry attribute profile at other frequencies.

4.1.2.1. Frequency of 0.125 Hz

The asymmetry attribute profiled at specified offsets and acquisition frequency of 0.125 Hz are shown below in Figure 17 and Figure 18.

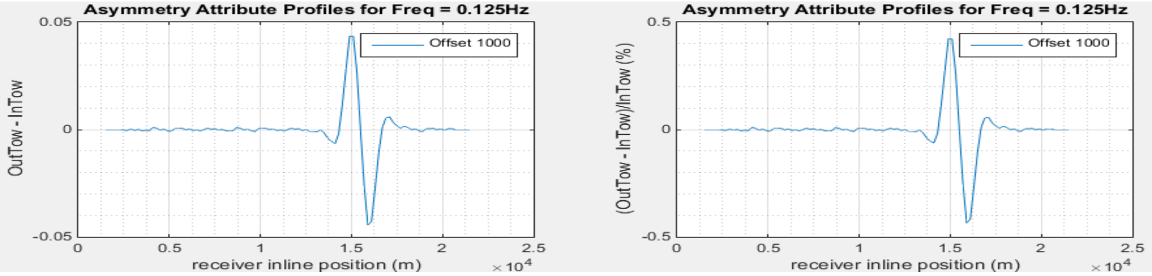

Figure 17. Non-normalized and normalized Asymmetry attribute profile at 0.125Hz and offset of 1000 m.

At offset of 1000 m (Figure 17) and 0.125 Hz, there is a clear trend in the signature of the asymmetry attribute response with the absolute maximum and minimum conspicuously revealed at receiver inline positions 14,900 m and 15,900 m respectively. This receiver inline positions of the absolute maximum and minimum corresponds to receivers (Rx68) and (Rx73). It can be seen that a perfect symmetry exists between the absolute maximum and minimum with respect to a vertical axis crossing Rx70 and Rx71 at inline positions 15300 m and 15500 m respectively. This perfect symmetry suggests the presence of a uniform resistivity distribution, thus the possibility of the embedded resistor being within this region. In fact, the absolute maximum and minimum locations is seen to match the position of the opposite polarity of the embedded resistor, which implies that the boundaries of the resistor are within and/or between Rx68 and Rx73. Meanwhile, beyond the position/location of the resistive anomaly/resistor, asymmetry is evenly low, gradually approaching zero due to unavailability or low to none influence of the resistive anomaly at other receivers. However, it should be noted that in reality offsets of 1000 m are usually disregarded, because the information obtained at this low offset is usually marred by air wave effect but since the simulated data is devoid of such effects, asymmetry attribute profiled at offset of 1000 m is considered acceptable in this case.

At low frequency of 0.125 Hz and offset of 2000 m (Figure 18), the asymmetry attribute response shows qualitatively similar trend to that at offset of 1000 m (Figure 17). There is a noticeable approximate correspondence in the locations of the receiver inline position of the actual maximum and minimum, with same receivers seen to be at the positions of the opposite polarity of the embedded resistive body/resistor.

For both computational approach, the buried resistor is detected within Rx68 and Rx73, at inline positions 14900 m and 15900 m

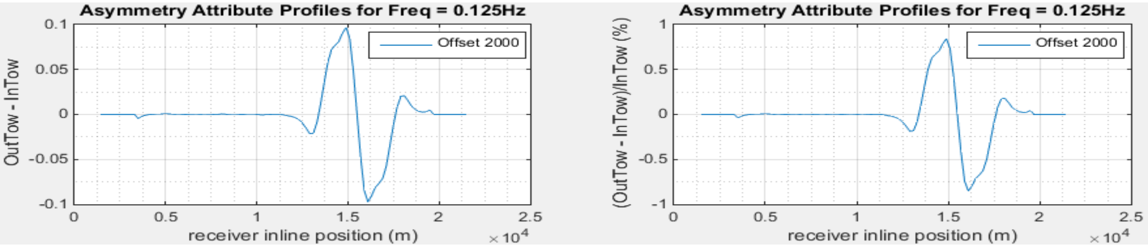

Figure 18. Non-normalized and normalized Asymmetry attribute profile at 0.125Hz and offset of 2000 m

Figure 19 and Figure 20 shows the outcome of the asymmetry attribute extracted and profiled at integrated range of offsets for the normalized and non-normalized computational approach at low frequency of 0.125 Hz.

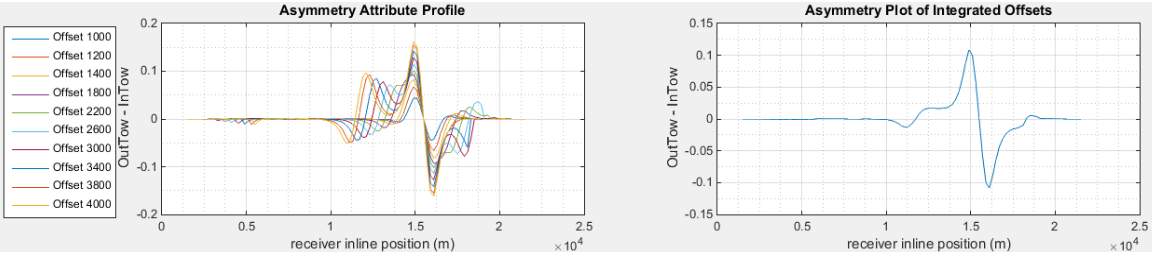

Figure 19. Non-normalized Asymmetry profile at integrated range of offsets for frequency of 0.125 Hz.

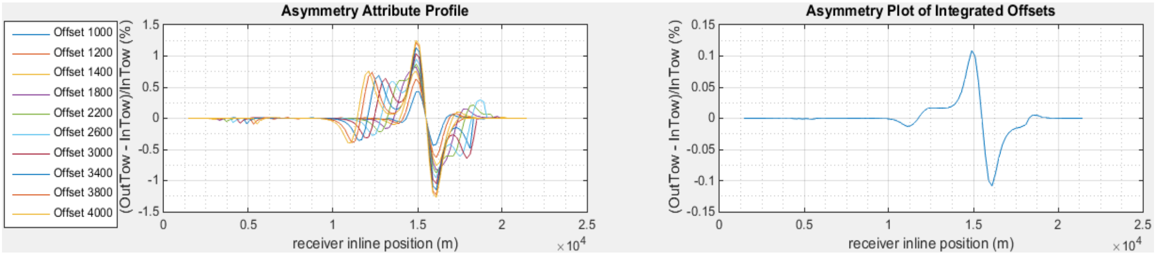

Figure 20. Normalized Asymmetry profile at integrated range of offsets for frequency of 0.125 Hz.

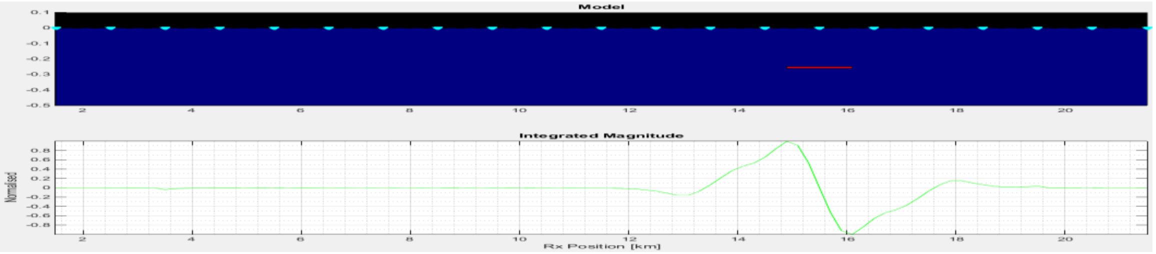

Figure 21. Superimposed model and asymmetry attribute of the magnitude.

These asymmetry attributes computed and profiled at these integrated range of offsets and low frequency of 0.125 Hz for both computational methods (Figure 19 and Figure 20) shows a qualitative similarity to that at the individual offsets of 1000 m and 2000 m but with quite smoother and clearer trend in the attribute response, with the locations of the absolute maximum and minimum matching the position of the opposite polarities of the embedded resistor. The left and right boundaries of the resistor also matches the asymmetry maximum and minimum at Rx68 and Rx73 and the point of perfect symmetry lies within Rx70 and Rx71 as depicted in the superimposed asymmetry attribute profile and resistivity model of Figure 21 above.

4.1.2.2. Frequency of 1 Hz

The asymmetry attribute profiled at specified offsets and acquisition frequency of 0.125 Hz are shown below in Figure 22 and Figure 23.

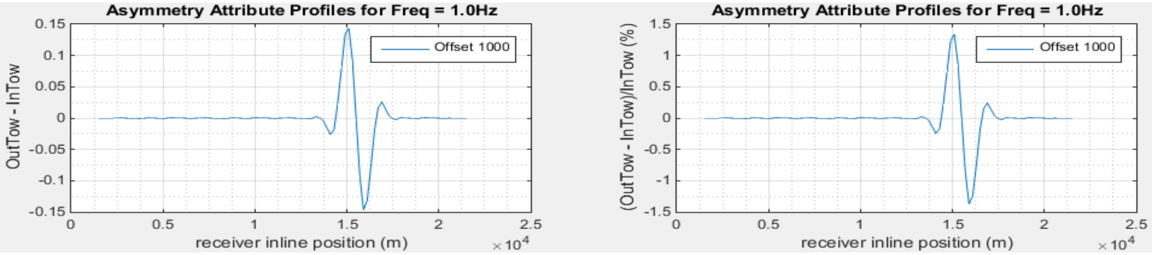

Figure 22. Non-normalized and normalized Asymmetry attribute profile at 1Hz and offset of 1000 m.

At high frequency of 1 Hz and offset of 1000 m (Figure 22), there is a clear and qualitative similar trend in the signature of the asymmetry attribute response in this high frequency with that at low frequency of 0.125Hz (Figure 17), with the absolute maximum and minimum conspicuously revealed at receiver inline positions 14,900 m and 15,900 m respectively. Due to sampling, there is a relatively insignificant shift in the location of the absolute maximum, but the discontinuities are identifiable with good approximation within Rx68 and Rx73. Similar to the attribute response in Figure 17, it can be seen that a perfect symmetry exists between the absolute maximum and minimum with respect to a vertical axis crossing Rx70 and Rx71 which suggests the presence of a uniform resistivity distribution and the possibility of the embedded resistor being within this region. In fact, the lateral boundaries of the embedded resistor matches the absolute maximum and minimum of the asymmetry attribute response with reasonable small errors of approximation within and/or between receivers (Rx68) and (Rx73). Meanwhile, beyond the location of the resistive anomaly or resistor, asymmetry is evenly low, gradually approaching zero due to unavailability or low to none influence of the resistive anomaly at other receivers. However, as earlier mentioned in the analysis of the asymmetry attribute of 0.0125 Hz, in reality offsets of 1000 m are usually disregarded because the information obtained at this very low offset is usually marred by air wave effect but since the simulated data is devoid of such effects, asymmetry attribute profiled at offset of 1000 m is considered acceptable in this case.

The asymmetry attribute response at frequency of 1 Hz and offset of 2000 m (Figure 23), shows qualitatively similar trend to that at offset of 1000 m (Figure 22) but appears with relatively higher intensity, i.e., smoother and clearer response. There is a noticeable approximate correspondence in the locations of the receiver inline position of the actual maximum and minimum at 14900 m and 15900 m, with same receivers seen to be within the positions of the opposite polarity of the embedded resistor

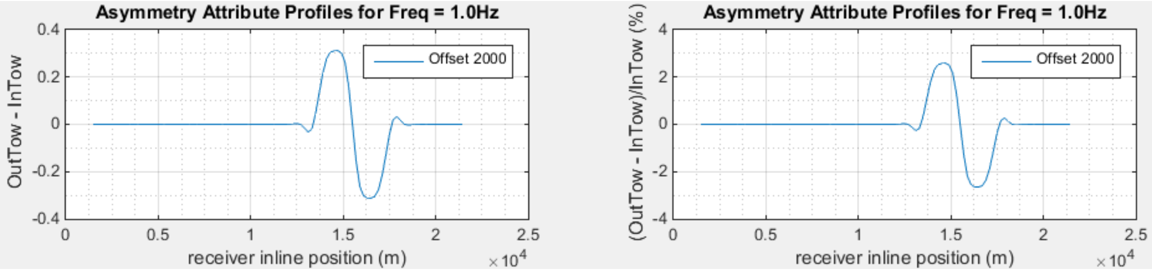

Figure 23. Non-normalized and normalized Asymmetry attribute profile at 1Hz and offset of 2000 m.

Figure 24 and Figure 25 shows the outcome of the asymmetry attribute extracted and profiled at integrated range of offsets for the normalized and non-normalized computational approach at high frequency of 1 Hz.

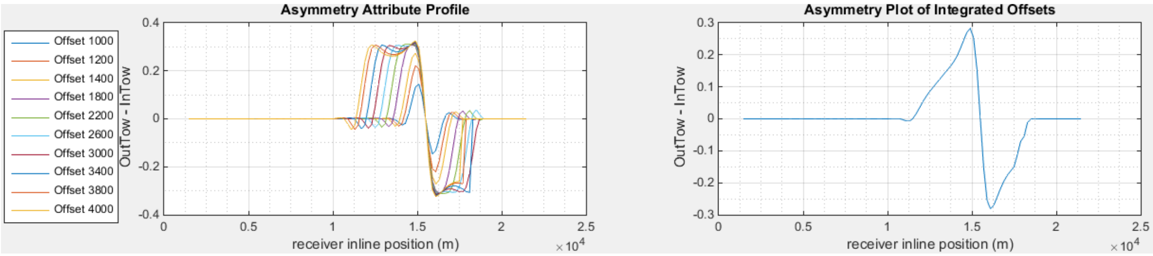

Figure 24. Non-normalized Asymmetry profile at integrated range of offsets for frequency of 1 Hz.

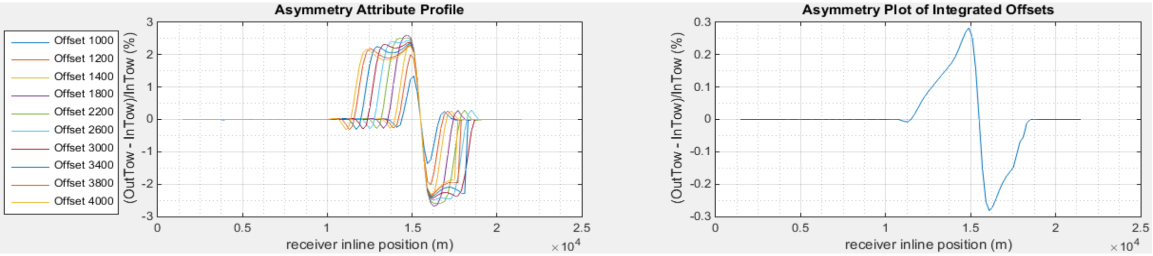

Figure 25. Normalized Asymmetry profile at integrated range of offsets for frequency of 1 Hz.

These asymmetry attributes computed and profiled at these integrated range of offsets and high frequency of 1 Hz for both computational methods (Figure 24 and Figure 25 above) shows a qualitative similarity to that at the individual offsets of 1000 m and 2000 m but with quite smoother and clearer trend in the attribute response and with the locations of the absolute maximum and minimum approximately matching the position of the opposite polarities of the embedded resistor.

Generally, the qualitative congruence in the asymmetry attribute responses at offsets of 1000 m, 2000 m and at integrated range of offsets in the considered frequencies (0.125 Hz and 1 Hz) and other frequencies (see appendix A), shows the efficacy of the asymmetry attribute computations and profiles in the detection of the lateral extent of buried resistive bodies and/or resistors.

4.2. Canonical model: Phase Processing Results

The outcome of the data processing involving the phase component of the electric field are presented and discussed as follows.

4.2.1. PVO PLOTS ANALYSIS

The first set of figures show the results of the extracted phase component mapped at different receivers-transmitters distances (offsets) and at the different acquisition frequencies. Figure 26 and Figure 27 presented here are for analysis and discussion of the noticeable trend of the recorded phase. Other receivers PVO plot show similar trend to the ones presented here thus similar information is deduced when other receivers are considered.

There are variations in the trend of the recorded phase of Rx50, with phase jumps of full cycle noticeably present at all frequencies as depicted in Figure 26 below. Also there is a noticeable difference between both represented curves, i.e., the background and the anomalous data at approximately 5000 m offset. This difference in the curves is due to the influence of the embedded resistor. In Figure 27, an almost evenly distributed trend exists in the recorded phase of RX68 in both the background and data curves at all acquisition frequencies and offsets. This trend in the phase response suggests that Rx68 highly senses the presence of the embedded resistor thus is expected to be within the lateral extent of the resistor

Subsequently, by unwrapping the originally recorded phase, it is reconstructed and the varying jumps suppressed, thereby restoring the physical continuity of the recorded phase of each of the receivers. The information obtained from the PVO plots forms the basis for further processing carried out on the phase in order to extract reasonable information about the simulated subsurface.

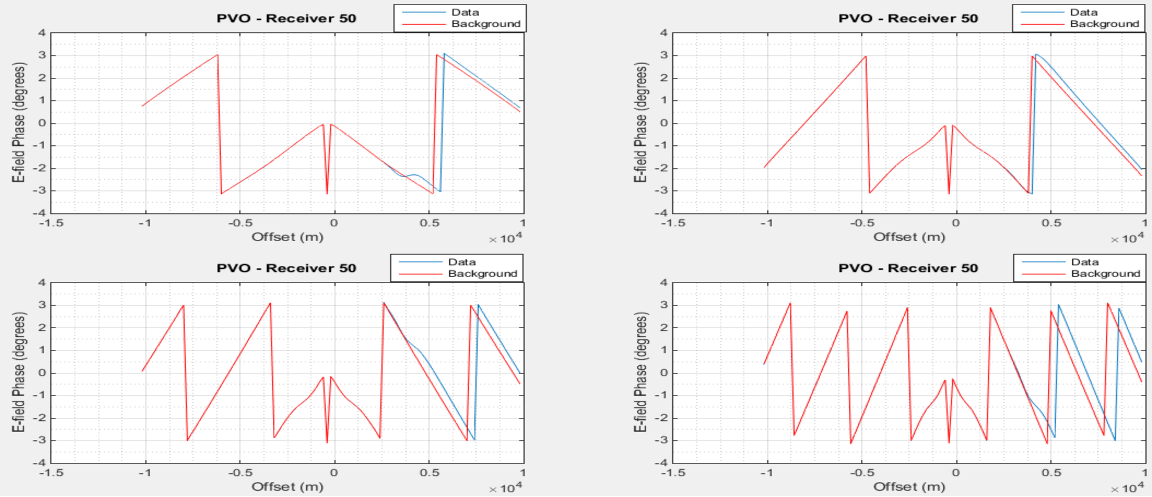

Figure 26 PVO of Rx50 showing the background and the resistive anomalous data. (Top left) PVO at 0.125 Hz (Top right) PVO at 0.25 Hz (Bottom left) PVO at 0.5 Hz (Bottom right) PVO at 1 Hz.

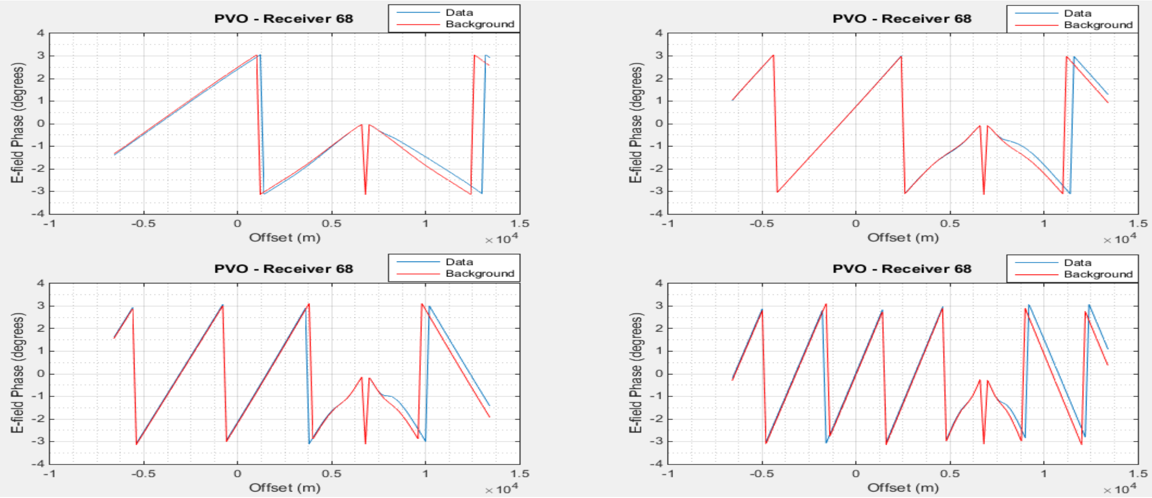

Figure 27. PVO of Rx68 showing the background and the resistive anomalous data. (Top left) PVO at 0.125 Hz (Top right) PVO at 0.25 Hz (Bottom left) PVO at 0.5 Hz (Bottom right) PVO at 1 Hz.

4.2.2. PHASE ASYMMETRY ATTRIBUTE PROFILE

For the phase asymmetry attribute profile, the acquisition frequency of 0.25 Hz at specified offsets is considered for analysis and discussion. At other frequencies and offsets, the same information revealed by the asymmetry attribute profile of 0.25 Hz is obtainable, due to the qualitative similarity in the trend of the asymmetry attribute profiles of each acquisition frequency.

4.2.2.1. Frequency of 0.25 Hz

Figure 28 shows the non-normalized and normalized asymmetry attribute computed and profiled with the phase component of the electric field observation at acquisition frequency of 0.25 Hz.

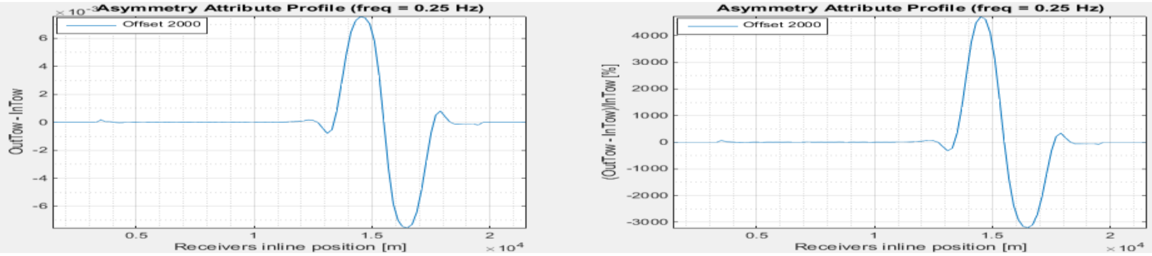

Figure 28. Non-normalized and normalized Asymmetry attribute profile at 0.25Hz and offset of 2000 m.

The phase asymmetry attribute computed at short offsets of 2000 m and frequency of 0.25 Hz shows qualitatively similar trend to asymmetry attribute computed with the magnitude of the electric field at same offset and frequencies of 0.125 Hz and 1 Hz, revealing same information about the locality and lateral extent of the embedded resistor in the synthetic model. The locations of the actual maximum and minimum which corresponds to the positions of opposite polarity of the embedded resistor is noticeably within receiver inline positions 14,900 m and 15,900 m, i.e., within Rx68 and Rx73. The noticeable high values in the normalized asymmetry attribute profile is possibly due to effects of very small in-towing phase data values, thus when the difference of the out-towing and in-towing data is normalized with these very small in-towing data values, the resulting output are very high normalized attribute values.

Figure 29 and Figure 30 shows the outcome of the asymmetry attribute extracted from the phase data and profiled at integrated range of offsets for the normalized and non-normalized computational approach at low frequency of 0.25 Hz.

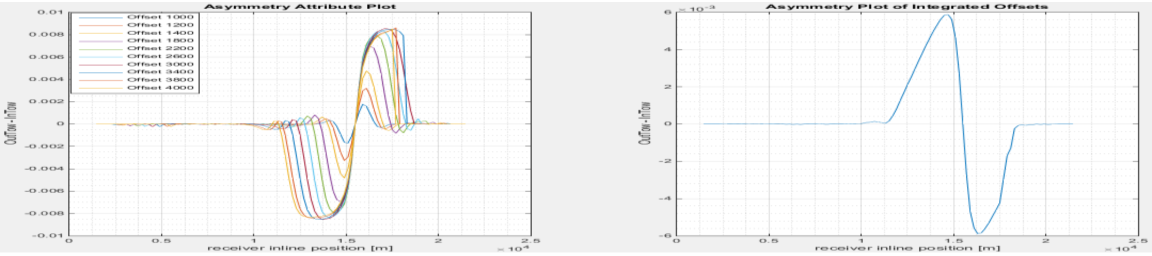

Figure 29. Non-normalized Asymmetry profile at integrated range of offsets for frequency of 0.25 Hz.

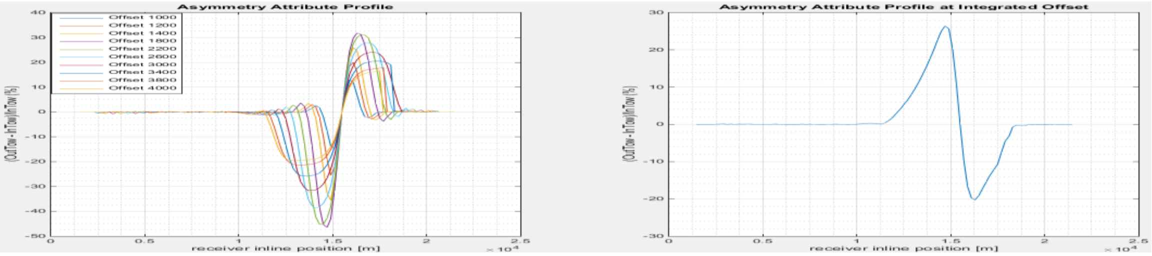

Figure 30. Normalized Asymmetry profile at integrated range of offsets for frequency of 0.25 Hz.

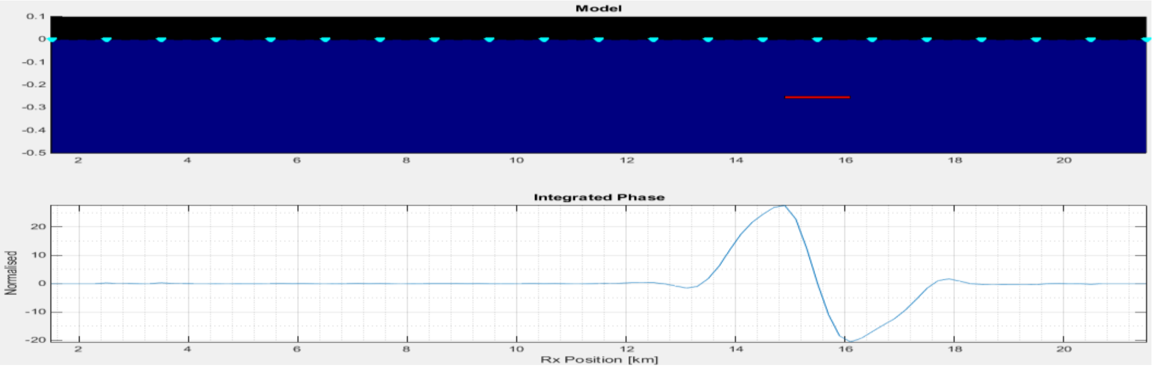

Figure 31. Superimposed model and asymmetry attribute of the phase.

These asymmetry attributes extracted from the phase component of the electric field observations and profiled at integrated range of offsets and low frequency of 0.25 Hz for both computational approach shows qualitative similarity to that computed at the individual offsets of 2000 m with the locations of the absolute maximum and minimum seen to match the positions of the opposite polarities of the embedded resistor in the synthetic model i.e., at receiver inline positions 14,900 m and 15,900 m respectively The inline positions corresponds to Rx68 and Rx73 and a point of perfect symmetry noticeably lies within Rx70 and Rx71. The observed trend in the signature of the asymmetry attribute responses of the phase components of the electric field clearly reveals similar information as the asymmetry attribute computed with the magnitude as can be seen in the superimposed plot of Figure 31 above.

4.3. GOM Benchmark Data Results

4.3.1. MVO PLOTS ANALYSIS

After the preliminary processing of this set of data, the first important and major processing carried out on this dataset involved the extraction and mapping of amplitude component of the electric field responses at each receiver with respect to the distances between the receiver and the electromagnetic field transmitting source/ sources which the considered receiver responds to. The outcome of this stage of the data processing which happens to be the basis for further processing of this dataset is shown below in Figure 32, Figure 33 and Figure 34. The three figures (Figure 32, Figure 33 and Figure 34) are considered for explanation and corresponds to receivers in the beginning, middle and end of the acquisition geometry respectively. In "appendix B" are figures corresponding to some of the other receivers MVO, for further understanding of the trend of the mapped magnitude. Each figure illustrates the magnitude/amplitude responses of the electric field versus offsets for each receiver at the frequencies (0.06 HZ, 0.18 Hz, 0.125 Hz, 0.25 Hz and 2.25 Hz) utilized in the simulated mCSEM acquisition.

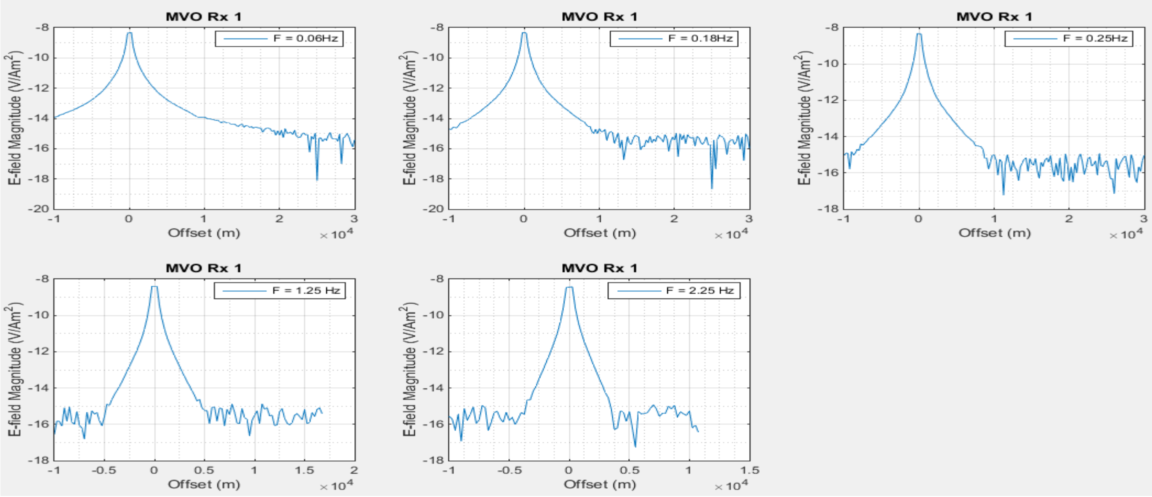

Figure 32. Magnitude versus Offset of Rx1 showing the resistive anomalous data at different acquisition frequency.

The observed MVO response of Rx1 in Figure 32 shows an increasing noisy trend in the in-towing and out-towing parts of the measured magnitude/amplitude component of the electric field as the acquisition frequency increases from 0.06 Hz to 2.25 Hz. This noise is prominent at higher frequencies (rapidly varying magnitude trend) because of higher attenuation at increased distances and offsets from the source. Clearly, at larger offsets noise start to dominate over highly attenuated signals and as attenuation gets higher at increased frequencies, the noise location encroaches into the shorter offsets.

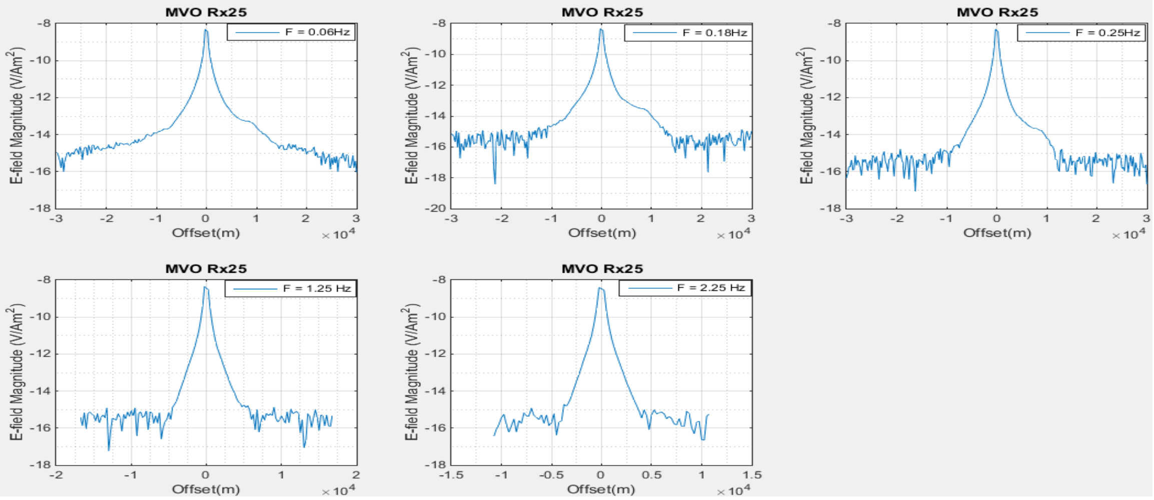

Figure 33. Magnitude versus Offset of Rx25 showing the resistive anomalous data at different acquisition frequency.

The observed MVO response of Rx25 in Figure 33 shows a clear noisy trend at the extremes of both parts of the measured magnitude component of the electric field in all acquisition frequencies. The prominent attenuation of the measured field at both low and high frequencies can be said to be as a result of the effect of the resistivity distribution within the source positions and receiver location. It is seen that the same trend appears in receivers located within the middle of the acquisition geometry of this survey as they all have a noticeable high attenuation of the responses and domination of noise at larger offsets.

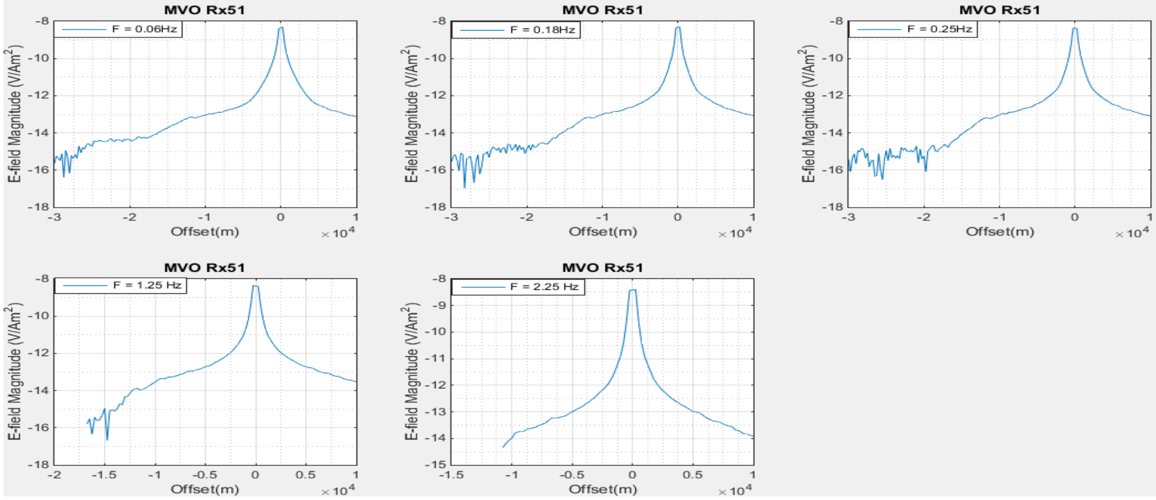

Figure 34. Magnitude versus Offset of Rx51 showing the resistive anomalous data at different acquisition frequency.

The observed MVO response of Rx51 in Figure 34 shows a noisy and attenuating trend in the in-towing part of the measured magnitude of the electric field at high offsets and at frequencies of 0.06 Hz, 0.18 Hz and 0.25 Hz respectively, while at shorter distances and/or offsets the attenuation trend gradually reduces at frequency of 1.25 Hz until it is completely lost at frequency 2.25 Hz. This could be as a result of the receiver being located at the end of the acquisition geometry thus it records electric field responses coming from few transmitting sources located at short distances from the receiver.

Generally, it should be noted that the attenuation trends of the measured fields with offsets observed in the MVO plots of the receivers at various acquisition frequencies is also a function of resistivity distribution in the space between the actual source position and receiver locations thus the prominent attenuating trends in most of the MVO plots of this dataset confirms the actual presence of a resistive body in the simulated subsurface of the mCSEM acquisition.

4.3.2. ASYMMETRY ATTRIBUTE PROFILE ANALYSIS

Prior to the analysis of the computed GOM data asymmetry attributes and profiles, a table showing some of the receivers within the area of influence of possible subsurface resistive layers or resistors and their inline positions are presented below. Table 2 will aide understanding of the result analysis involving the receiver's inline position as discussed in this section.

Table 3 Inline positions of GOM data receivers [m]

Receiver (Rx)	2	4	5	7	8	15	17	19	20	26	27
Rx inline Position (m)	21500	24500	26000	29000	30500	41000	44000	45500	47000	57500	59000
Receiver (Rx)	34	39	40	42	43	44	45	46	47	49	
Rx inline Position (m)	69500	77000	78500	81500	83000	84500	86000	87500	89000	92000	

The outcome of the normalized and non-normalized computations carried out on the extracted asymmetry data at specified offsets from each parts of the magnitude versus offset plot of the grid of receivers is a mapping of the variation of subsurface resistive anomaly in plots termed asymmetry or symmetry attribute profile. The sets of results obtained are that of symmetry attribute profile developed at fixed frequencies (frequencies corresponds to that used in the simulated acquisition) and varying offsets (short and long offsets) and at integrated range of offsets respectively. In "appendix C" are figures showing asymmetry attribute profiled at other integrated range of offsets for reference and further understanding of the asymmetry attribute responses. The analysis and discussion of these set of results are presented under subheadings corresponding to each frequency, i.e., 0.06 Hz, 0.18 Hz, 0.25 Hz, 1.25 Hz and 2.25 Hz respectively.

4.3.2.1. Frequency of 0.06 Hz

The asymmetry attribute profiled at specified short and long offsets and combination of offsets at this frequency are shown below in Figure 35 to Figure 38, while the asymmetry attribute computed at integrated range of offsets are shown in Figure 39 and Figure 40.

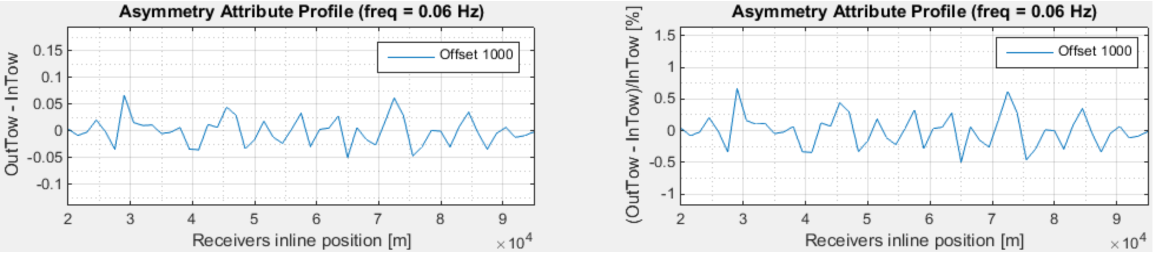

Figure 35. Non-normalized and normalized Asymmetry attribute profile at 0.06 Hz and offset of 1000 m.

At very low frequency of 0.06 Hz and offset of 1000 m (Figure 35), there is an undulating trend in the signature of the asymmetry attribute with slightly noticeable and identifiable maximum and minimum, but the information as regards the presence or location of resistors or resistive layers obtainable at this very short offsets can be unreliable as the magnitude of the electric field responses are usually affected by the attenuation effects of the air waves at very short offset of 1000 m.

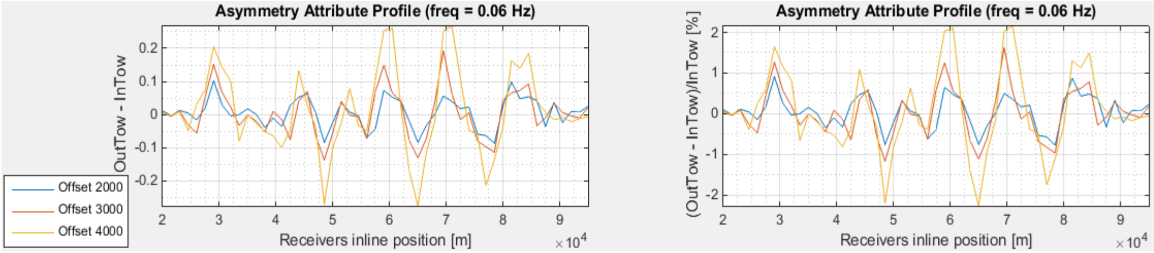

Figure 36. Non-normalized and normalized Asymmetry attribute profile at 0.06 Hz and offsets of 2000, 3000 and 4000 m.

On the other hand, as the offset increases to 2000 m, 3000 m and 4000 m (Figure 36), the asymmetry attribute signatures becomes progressively clearer with the responses noticeably elongated. The asymmetry attribute responses at offset of 2000 meters and 3000 meters show a clear qualitative similarity with actual and local maximums and minimums which corresponds to the boundaries of possible resistors around receiver inline positions 29,000 m, 48,500 m, 59,000 m and 78,500 m respectively. A minor peak and trough can be seen around receiver inline positions 81,500 meters and 87,500 m. While at offset of 4000 m there is a noticeable slight shift in the location of the actual maximum, with other features illuminated towards the right of the profile. The slight change in the location of the actual maximum suggests that other possible resistors or resistive layers exists (probably overlapping) within the simulated subsurface. Based on this observation and the knowledge of the possible receiver inline positions, it can be inferred that at least three resistors or resistive layers exists in this simulated subsurface; one between Rx7 and Rx20, the other between Rx27 and Rx40 and possibly another starting at the minor peak around Rx42 with identifiable right boundary at Rx46. Also, from the clear trend that exists along the profile at 4000 m, there is a possibility that other resistors probably overlap each other within the layers of this simulated subsurface.

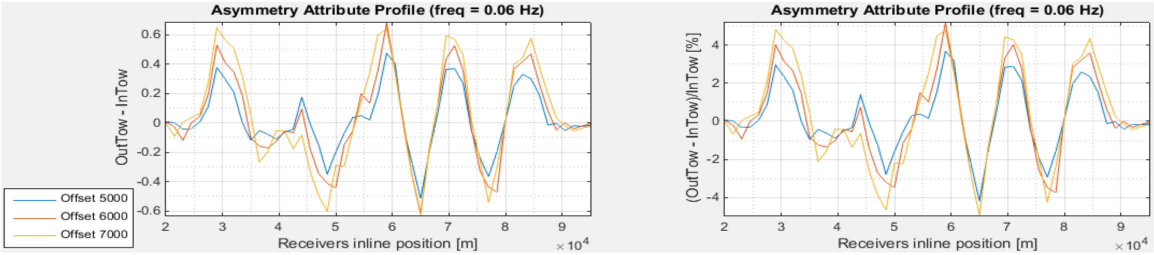

Figure 37. Non-normalized and normalized Asymmetry attribute profile at 0.06 Hz and offsets of 5000, 6000 and 7000 m.

The asymmetry attribute profile at offsets of 5000 m, 6000 m and 7000 m (Figure 37) shows similar trend in the signature, with positions of the resistors and there boundaries quite pronounced. There is a noticeable elongation in the signature of the responses as offset progressively increases and there is a clearer illumination of the asymmetry attribute responses which suggests possible presence of other subsurface features not clear at short offsets and low frequency. The asymmetry attribute plot at these long offsets actually has same trend shown in figure (Figure 36) but depending on the considered offset there is a slight change in the positions of the actual and local maximum and minimum. Considering the response at offset of 7000 m, the actual and local maximum and minimum are at receiver inline positions 29,000 m, 48,500 m, 59,000 m and 77,000 m and a minor peak also exists at receiver inline position 84,500 m. These receiver inline positions corresponds to Rx7 and Rx20 for the actual maximum and minimum, Rx27 and Rx39 for the relative maximum and minimum and Rx 44 for the minor peak. Also from the observation, it can be inferred that at least three resistive layers or resistors exist in the simulated subsurface. This inference tally with what was obtained at offsets of 2000 m, 3000 m and 4000 m in Figure 36.

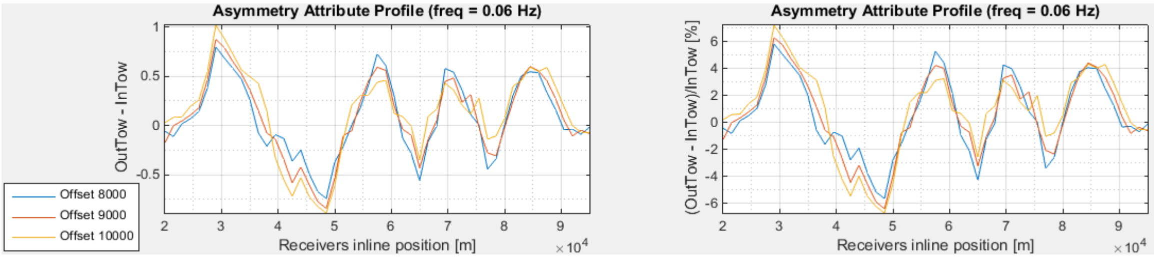

Figure 38. Non-normalized and normalized Asymmetry attribute profile at 0.06 Hz and offsets of 8000, 9000 and 10000 m.

The signature of the asymmetry attribute profile at very long offsets of 8000 meters, 9000 m and 10000 m (Figure 38) has similar trend as that profiled at 5000 m, 6000 m and 7000 m (Figure 37) but with a slight change in the location of the relative maximum and an increased and clearly illuminated minor peak. The elongated shape of the asymmetry attribute response and the slight change in position of the relative maximum at these longer offsets suggests that deeper layers of the subsurface is being probed and probably the presence of overlapping resistors or resistive layers. The positions of the actual and local maximum and minimum are around receiver inline positions 29,000 m, 48,500 m, 57,500 m, 77,000 m and the minor peak is at receiver inline position 84,500 m, implying the possible boundaries of the resistors are between Rx7 and Rx20; Rx26 and Rx39, and one starting at Rx44 respectively. In congruence to the inference made at other offsets, the positions of the opposite polarities (i.e., positions of actual and local maximum, minimum and illuminated minor peak) at this very long offset suggests the presence of at least three resistive layers or resistors in the simulated subsurface.

Figure 39 and Figure 40 below are the asymmetry attribute computed and profiled at integrated range of offsets for the non-normalized and normalized computation approach and at frequency of 0.06 Hz.

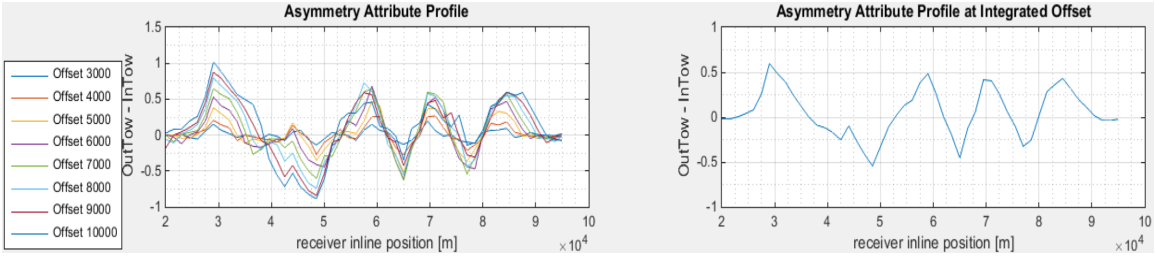

Figure 39. Non-normalized Asymmetry profile at integrated range of offsets for frequency of 0.06 Hz.

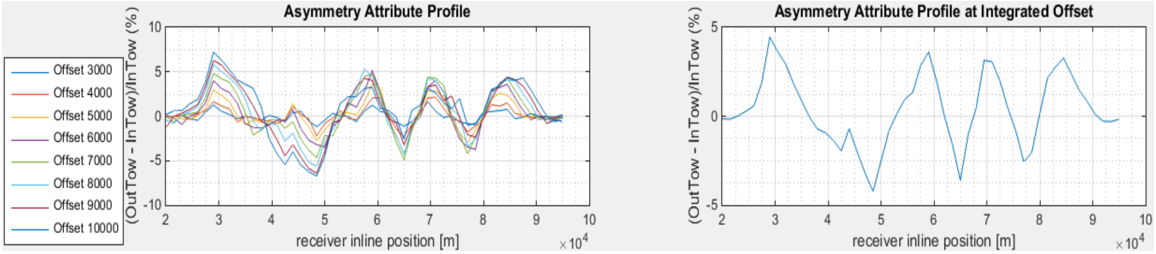

Figure 40. Normalized Asymmetry profile at integrated range of offsets for frequency of 0.06 Hz.

The signature of the asymmetry attribute computed and profiled at a range of integrated offsets (Figure 39 and Figure 40) and this low frequency (0.06 Hz), shows a clear and qualitatively similar trend for both computational approach. There is a pronounced actual maximum and minimum around receiver inline positions 29,000 m and 48,500 m while a local maximum and minimum is seen around receiver inline positions 59,000 m and 77,000 m. Another peak can be seen at receiver inline position of 84,500 m, but with no identifiable minimum, this could be another resistive body or an anomaly arising from attenuation effect of seawater at long offsets, in this case 10,000 m. The presence of the maximums (actual and local), minimums (actual and local) and minor peak suggests that at least three resistors or resistive layers of opposite polarity exists and there boundaries are around Rx7 and Rx20 for the first resistor and around Rx27 and Rx39 for the second resistor and another resistive anomaly starting around

Rx44. The receivers are identifiable from the inline positions where the opposite polarities are located.

4.3.2.2. Frequency of 0.18 Hz

The asymmetry attribute profiled at specified short and long offsets and combination of offsets at this frequency are shown below in Figure 41 to Figure 44, while the asymmetry attribute computed at integrated range of offsets are shown in Figure 45 and Figure 46.

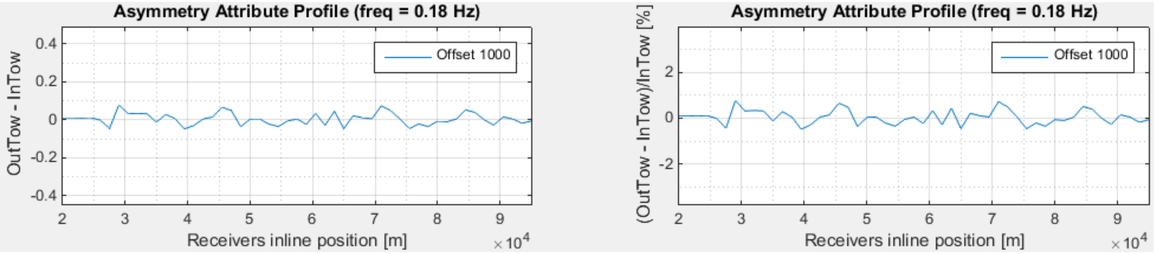

Figure 41. Non-normalized and normalized Asymmetry attribute profile at 0.18 Hz and offset of 1000 m.

At offset of 1000 m (Figure 41), the signature of the asymmetry attributes shows an increased attenuation with not so distinguishable actual and local maximums and minimums. Thus, no clear information as regards the presence or location of a resistive discontinuity or anomaly can be obtained at this very short offset and this frequency (0.18 Hz). This attenuating trend could be as result of contributions from air wave (airwave effect) which is usually common at very short offset.

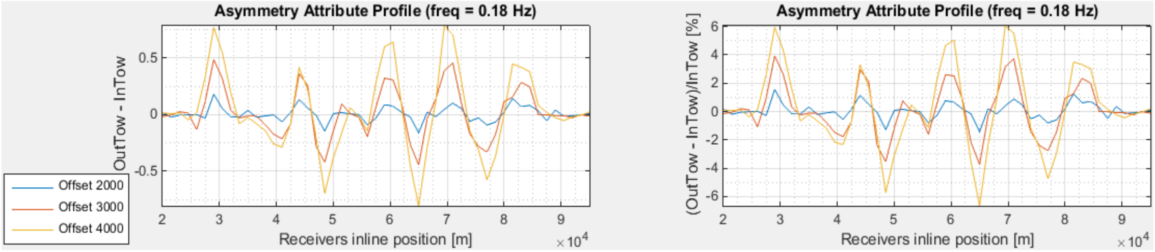

Figure 42. Non-normalized and normalized Asymmetry attribute profile at 0.18 Hz and offsets of 2000, 3000 and 4000 m.

Similar to the asymmetry attribute profile at 0.06 Hz, at the combination of offsets of 2000 m, 3000 m and 4000 m (Figure 42), the asymmetric attribute responses becomes progressively clearer, illuminating the maximums and minimums with less attenuation. The locations of the actual and local/relative maximum and minimum are around same receiver inline positions to that of the asymmetry attribute profiled at 0.06 Hz (Figure 36). This qualitative similarity between the asymmetry attribute response at 0.06 Hz and 0.18 Hz justifies the earlier inference about the existence of embedded resistors in the simulated subsurface.

From the asymmetry attribute response at offsets of 4000 m, it can be said that deeper layers of the simulated subsurface is being probed because the signature extends farther than at the shorter offsets. Also, the trend of the asymmetry attribute response at the offset of 4000 m and this frequency (0.18 Hz) shows a clear qualitative similarity to that at same offset but profiled at 0.06 Hz (Figure 36). Considering all the asymmetry signature in Figure 42, i.e., with all the depicted offsets (2000 m, 3000 m and 4000 m), there is a clear suggestion of the presence of different resistors/ resistive layers which could be overlapping each other and/or located at different depths. The asymmetry attribute signature is clearer at this low frequency (0.18 Hz) and longer offset of 4000 m, making it possible for probable deep discontinuities to be detected.

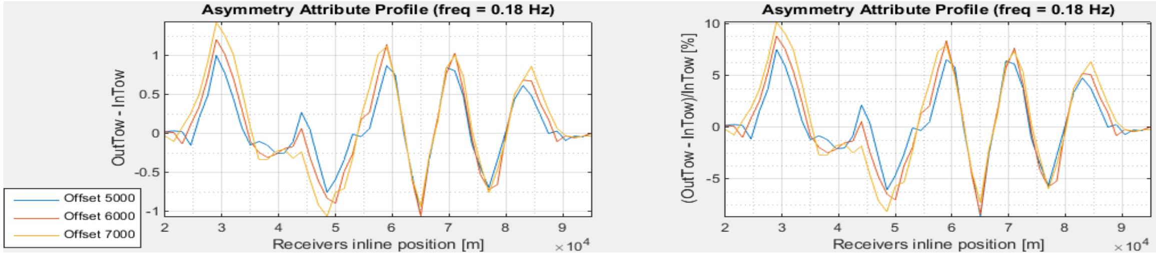

Figure 43. Non-normalized and normalized Asymmetry attribute profile at 0.18 Hz and offsets of 5000, 6000 and 7000 m.

Considering the asymmetry attribute profile at offsets of 5000 m, 6000 m and 7000 m (Figure 43), there is an almost absolute similarity in the trend of the discontinuity with that profiled at frequency of 0.06 Hz. The locations of the receiver inline positions are same with the asymmetry profile at 0.06 Hz thus same receivers, i.e., Rx7, Rx20, Rx27, Rx39 and another peak at Rx44 are inferred to be detecting the presence of possible resistive layers or resistors. Also from the observation, it can be inferred that at least three resistive layers or resistors exist in the simulated subsurface. This inference tally with what was obtained at offsets of 2000 m, 3000 m and 4000 m in Figure 42.

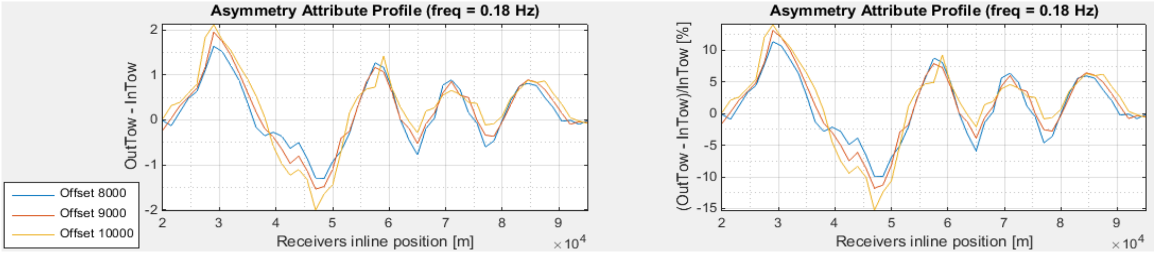

Figure 44. Non-normalized and normalized Asymmetry attribute profile at 0.18 Hz and offsets of 8000, 9000 and 10000 m.

The response of the asymmetry attribute profile at very long offsets of 8000 meters, 9000 m and 10000 m (Figure 44) has qualitative similar trend as that in Figure 38, i.e., same combination of offsets and at frequency of 0.06 Hz. Also, it reveals similar information as that obtainable from Figure 43. Based on this similarity, the same inference can be made concerning the possible presence of at least three resistors in the simulated subsurface.

Figure 45 and Figure 46 below are the asymmetry attribute computed and profiled at integrated range of offsets for the non-normalized and normalized computation approach and at frequency of 0.18 Hz.

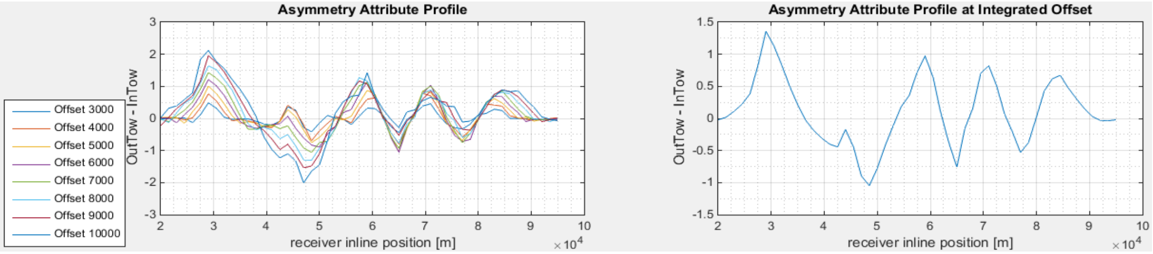

Figure 45. Non-normalized Asymmetry profile at integrated range of offsets for frequency of 0.18 Hz.

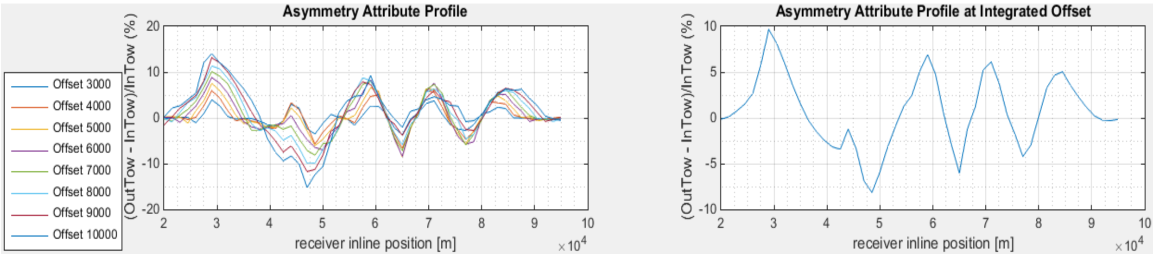

Figure 46. Normalized Asymmetry profile at integrated range of offsets for frequency of 0.18 Hz.

The signature of the asymmetry attribute computed and profiled at a range of integrated offsets (Figure 45 and Figure 46) and at this frequency (0.18 Hz), shows a clear and qualitatively similar trend for both computational approach, and tally with the trend seen in the asymmetry attribute computed in integrated range of offsets at frequency of 0.06 Hz. Thus, the congruence in location of receivers suggests and justifies the existence of resistors or resistive layers in the subsurface. The right and left boundaries of these resistors are at locations of distinguishable opposite polarities which is around the receivers at the inline positions corresponding to that at the asymmetry attribute computed in integrated range of offsets at frequency of 0.06 Hz (Figure 39 and Figure 40).

4.3.2.3. Frequency of 0.25 Hz

The asymmetry attribute profiled at specified short and long offsets and combination of offsets at this frequency are shown below in Figure 47 to Figure 50, while the asymmetry attribute computed at integrated range of offsets are shown in Figure 51 and Figure 52.

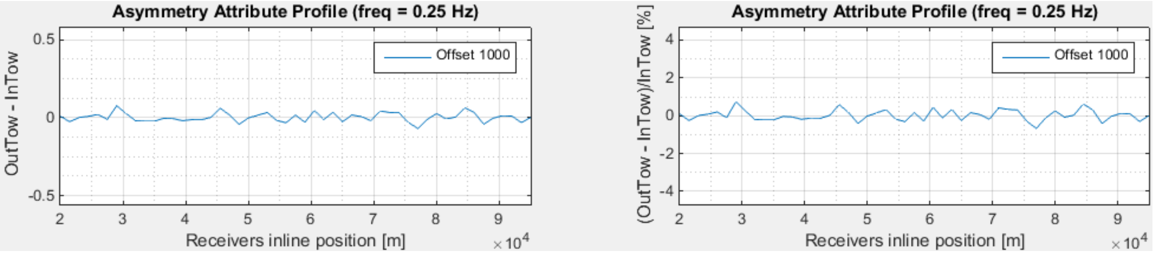

Figure 47. Non-normalized and normalized Asymmetry attribute profile at 0.25 Hz and offset of 1000 m.

There is a qualitative similarity in the trend of the asymmetry attribute profiled at frequency of 0.25 Hz (Figure 47) and that profiled at frequency of 0.18 Hz and at offset of 1000 m (Figure 41), thus, no clear information as regards the presence or location of a resistive discontinuity or anomaly can be obtained from this very short offset.

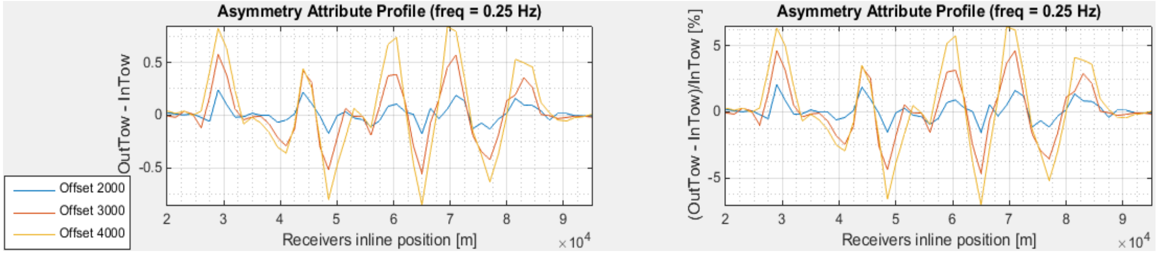

Figure 48. Non-normalized and normalized Asymmetry attribute profile at 0.25 Hz and offsets of 2000, 3000 and 4000 m.

Similar to asymmetry attributes computed and profiled at 0.06 Hz and 0.18 Hz, as the offset increases to 2000 m, 3000 m and 4000 m respectively (Figure 48), the responses of the asymmetry attribute at this frequency of 0.25 Hz becomes progressively clearer, illuminating the maximums and minimums with less attenuation. The locations of the actual and local maximum and minimum are almost exactly the same with the asymmetry attribute profiled at frequency of 0.18 Hz (Figure 42), with boundaries around the same receivers, i.e., between Rx7 and Rx20 for the actual maximum and minimum and between Rx27 and Rx39 for the relative maximum and minimum, while the minor resistive layer is suspected within receivers Rx44 and Rx49. The congruence in the trend along the profiles reconfirms the inference that possible resistive layers exists within the simulated subsurface. Also, from the minor trends in the signature of the asymmetry attribute responses, there is a clear suggestion of the presence of other possible resistors which could be overlapping each other and/or located at different depths.

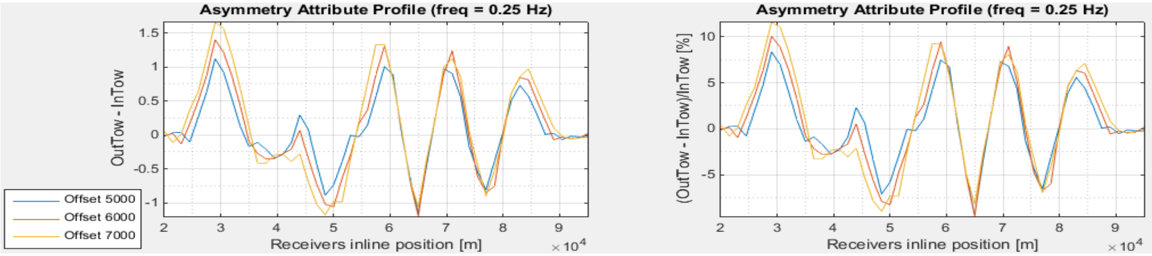

Figure 49. Non-normalized and normalized Asymmetry attribute profile at 0.25 Hz and offsets of 5000, 6000 and 7000 m.

The asymmetry attribute profile at offsets of 5000 m, 6000 m and 7000 m (Figure 49) shows similar trend in the response to that of the asymmetry attributes profiled at frequency of 0.18 Hz and same offsets (Figure 43), with the actual and local maximum and minimums and minor peak located at about same receiver inline positions. This similarity in the attribute response clearly supports the earlier inference that something resistive exists in the simulated subsurface.

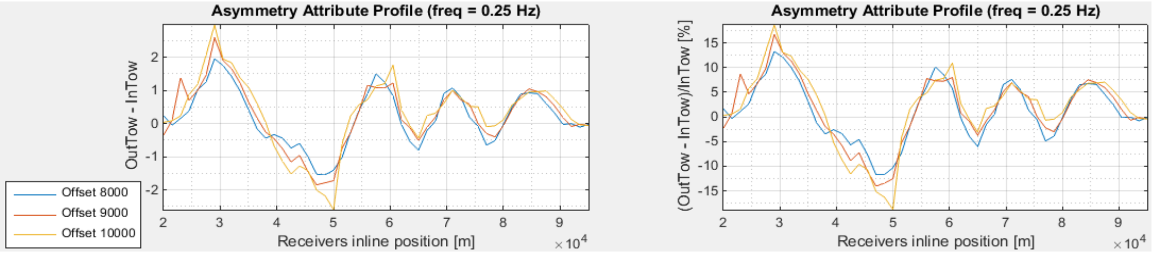

Figure 50. Non-normalized and normalized Asymmetry attribute profile at 0.25 Hz and offsets of 8000, 9000 and 10000 m.

As the offset progressively increases to 8000 m, 9000 m and 10000 m (Figure 50), there is a noticeable slight increase in the attenuation of the asymmetry attribute response, though the trend maintains similarity to the asymmetry attribute profile at frequencies 0.18 Hz and 0.06 Hz in Figure 38 and Figure 44 respectively. The information obtained from this asymmetry attribute response and this frequency also suggests the presence of resistors or resistive layers in the simulated subsurface. In congruence to the inference made at other offsets, the positions of the opposite polarities (i.e., positions of actual and local maximum and minimum) and the minor peak at this very long offset suggests the presence of at least three resistive layers or resistors in the simulated subsurface.

Figure 51 and Figure 52 below are the asymmetry attribute computed and profiled at integrated range of offsets for the non-normalized and normalized computation approach and at frequency of 0.25 Hz.

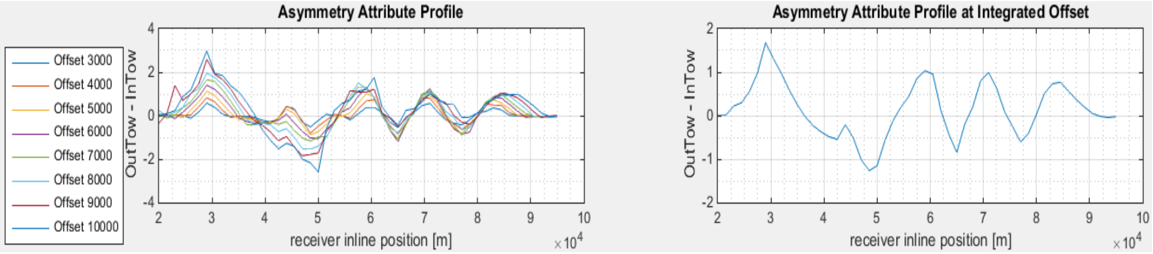

Figure 51. Non-normalized Asymmetry profile at integrated range of offsets for frequency of 0.25 Hz.

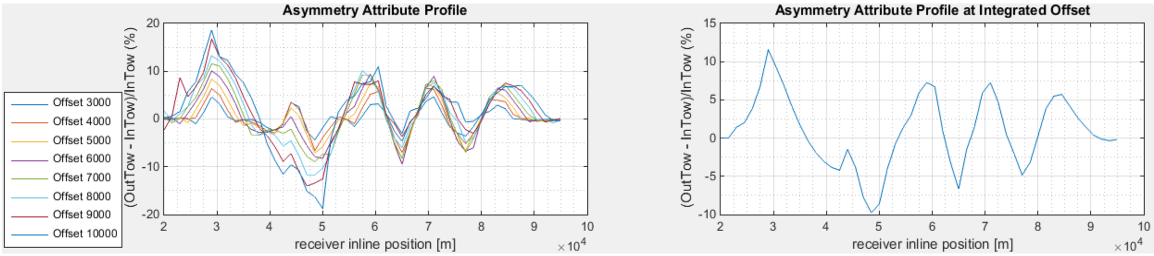

Figure 52. Normalized Asymmetry profile at integrated range of offsets for frequency of 0.25 Hz.

The signature of the asymmetry attribute computed and profiled at a range of integrated offsets (Figure 51 and Figure 52) and at this frequency shows a qualitatively clear and similar trend for both normalized and non-normalized computational approach. There is also an evident trend existing along the profile at this frequency which is similar to that of asymmetry attribute profiled at frequencies 0.06 Hz and 0.18 Hz (Figure 39, Figure 40 and Figure 45, Figure 46 respectively), with same information about the actual and local maximums, minimums and minor peak. The congruence in the location of the receivers suggests and justifies the existence of resistors or resistive layers in the subsurface. The right and left boundaries of these resistors are at locations of distinguishable opposite polarities which is around the receivers at the inline positions corresponding to that at the asymmetry attribute computed at integrated range of offsets at frequencies of 0.06 Hz and 0.18 Hz.

4.3.2.4. Frequency of 1.25 Hz

The asymmetry attribute profiled at specified short and long offsets and combination of offsets at this frequency are shown below in Figure 53 to Figure 56, while the asymmetry attribute computed at integrated range of offsets are shown in Figure 57 and Figure 58.

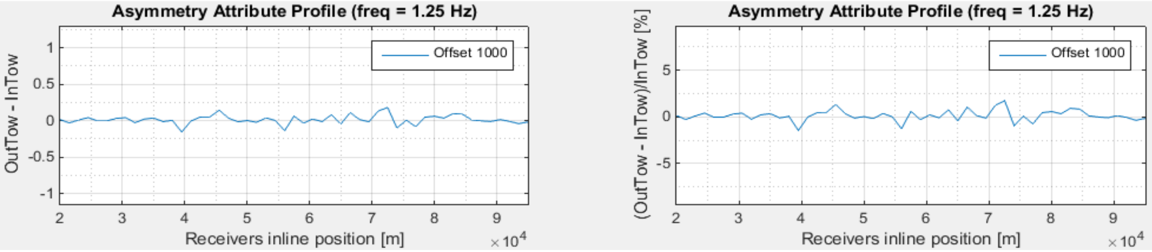

Figure 53. Non-normalized and normalized Asymmetry attribute profile at 1.25 Hz and offset of 1000 m.

At offset of 1000 m (Figure 53), there is an undulating trend in the signature of the asymmetry attribute with slightly identifiable maximum and minimum, but as earlier mentioned, the information as regards the presence or location of resistors or resistive layers obtainable at this very short offsets can be unreliable as the magnitude of the electric field responses are usually affected by the attenuation effects of the air waves and sea waves at very short offset of 1000 m and at high frequency.

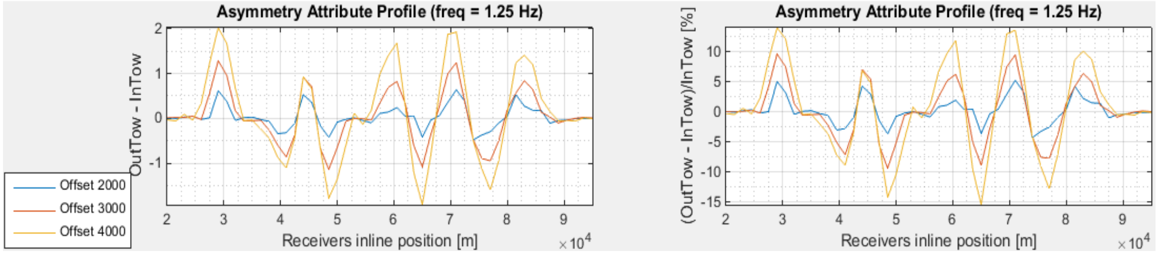

Figure 54. Non-normalized and normalized Asymmetry attribute profile at 1.25 Hz and offsets of 2000, 3000 and 4000 m.

On the other hand, as the offset increases to 2000 m, 3000 m and 4000 m (Figure 54), the asymmetry attribute responses becomes progressively clearer with suggestion of the presence of different resistors/ resistive anomalies which could be overlapping each other and/or located at different depths. The actual and relative maximum and minimum of the asymmetry attribute response is around the same receiver inline positions as that of the asymmetry attribute profiled at frequencies 0.25 Hz and 0.18 Hz but with clearer intensity. This observation and the clear congruence in the trend along the profile i.e., knowledge of the receiver inline positions, justifies the earlier inference that at least three resistive layers or resistors exists at/within the same receivers at lower frequencies but with a suggestive last layer between the minor locations at Rx43 and Rx47 respectively.

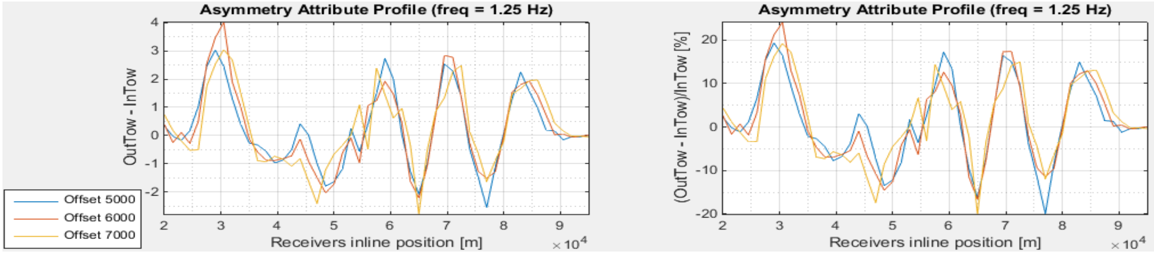

Figure 55. Non-normalized and normalized Asymmetry attribute profile at 1.25 Hz and offsets of 5000, 6000 and 7000 m.

The asymmetry attribute profile at offsets of 5000 m, 6000 m and 7000 m (Figure 55) shows quite similar trend in the response to that of the attributes profiled at frequencies of 0.25 Hz and 0.18 Hz, but with a noticeable attenuation in the attribute response. This attenuation in the response at these long offsets could be possibly due to contributions from the sea at long offsets. The actual and local maximums and minimums are at receiver inline positions 30,500 meters, 47,000 meters, 57,500 meters and 77,000 meters respectively while the relatively minor peak is at 86,000 meters. These corresponds to Rx8 and Rx19 for the actual maximum and minimum and Rx26 and Rx39 for the relative maximum and minimum and around Rx45 for the minor peak. The number of actual and local maximum and minimums, and the minor peak of the attribute response, justifies the inference that resistive layers exists within the simulated subsurface.

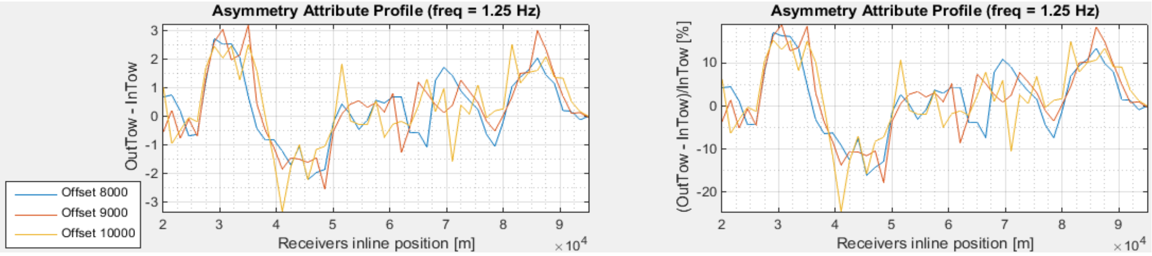

Figure 56. Non-normalized and normalized Asymmetry attribute profile at 1.25 Hz and offsets of 8000, 9000 and 10000 m.

There is an obvious increased attenuation in the response of the asymmetry attribute as the offset progressively increase to 8000 m, 9000 m and 10000 m as seen in Figure 56. This high discontinuity in the attribute response could be as a result of contributions by the attenuation effect of the sea water at very long offsets, which could mar the output or information deduced from the asymmetry attribute profile. Nevertheless, the general trend in the asymmetry profile is similar to that profiled at shorter offset, for example in Figure 55.

Figure 57 and Figure 58 below are the asymmetry attribute computed and profiled at integrated range of offsets for the non-normalized and normalized computation approach and frequency of 1.25 Hz.

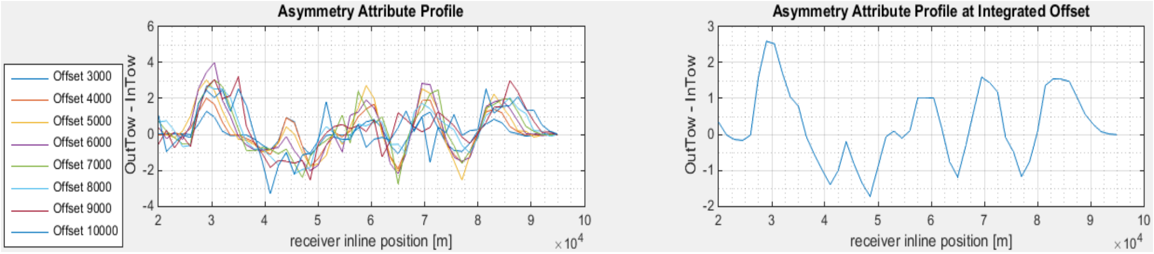

Figure 57. Non-normalized Asymmetry profile at integrated range of offsets for frequency of 1.25 Hz.

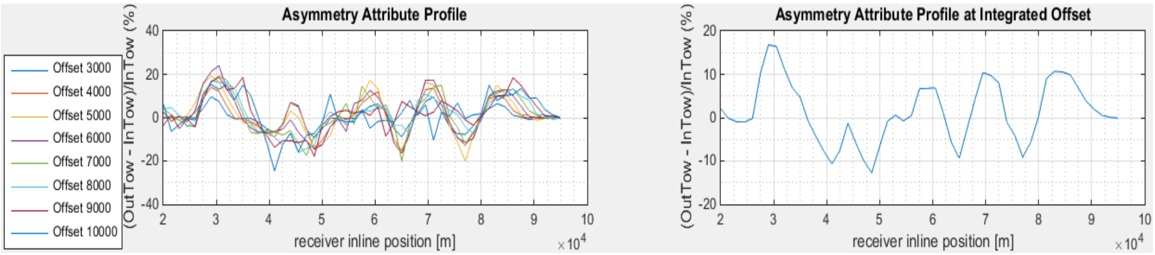

Figure 58. Normalized Asymmetry profile at integrated range of offsets for frequency of 1.25 Hz.

There is a clear and qualitative similarity in trend of the asymmetry attribute computed and profiled at a range of integrated offsets (Figure 57 and Figure 58) and at this frequency, utilizing both normalized and non-normalized computational approach. At this relatively high frequency, the locations of the relative maximum, minimum and the minor peak slightly changes while the locations of the actual maximum and minimum still tally with the location at the integrated attribute profile at the lower frequencies i.e., at 0.06 Hz, 0.18 Hz and 0.25 Hz. The new location of the receiver inline positions of the relative maximum and minimum are at 69,500 m and 77,000 m, corresponding to Rx34 and Rx39 respectively, while the minor peak is at receiver inline position 83,000 m corresponding to Rx43. The slight change in the relative positions can be related to possible existence of overlapping resistive layers in the simulated subsurface. Again, the clear qualitative similarity in the trends suggests the possibility of resistive layers between Rx7 and Rx20; and between Rx34 and Rx39, with another resistive anomaly starting from Rx43.

4.3.2.5. Frequency of 2.25 HZ

The asymmetry attribute profiled at specified short and long offsets and combination of offsets at this frequency are shown below in Figure 59 to Figure 62, while the asymmetry attribute computed at integrated range of offsets are shown in Figure 63 and Figure 64.

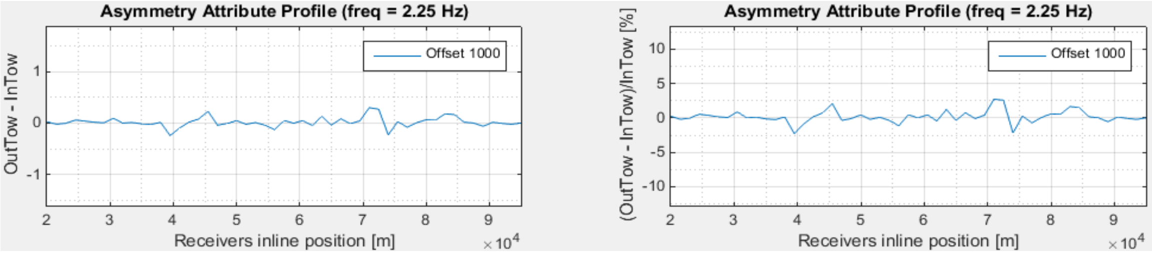

Figure 59. Non-normalized and normalized Asymmetry attribute profile at 2.25 Hz and offset of 1000 m.

The signature of the attribute profiled at this high frequency of 2.25 Hz (Figure 59) shows almost a clear qualitative similarity with that profiled at frequency of 1.25 Hz and offset of 1000 m (Figure 53). Therefore, same analysis and inference is applicable at this frequency.

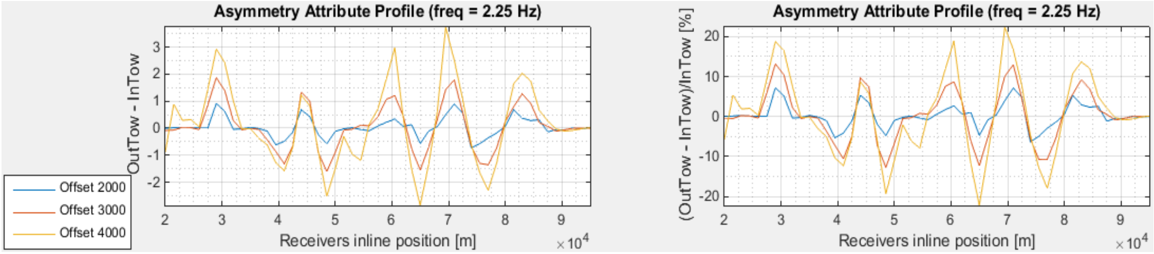

Figure 60. Non-normalized and normalized Asymmetry attribute profile at 2.25 Hz and offsets of 2000, 3000 and 4000 m.

Asymmetry attribute profiled at a combination of offsets of 2000 m, 3000 m and 4000 m (Figure 60), clearly shows the possible positions of the discontinuities and it's up and down polarities. Signature of asymmetry attribute response at offset of 4000 m and frequency of 2.25 Hz illuminates some features which were not identifiable at other frequencies. The newly illuminated features which could be the position of shallow resistor is located around receiver inline positions 21,500 m and 26,000 m, which corresponds to Rx2 and Rx5. Generally, there is a clear suggestion of the presence of different resistors/ resistive layers which could be overlapping each other and/or located at different depths as inferred from the analysis of asymmetry attributes at 2000 m and 3000 m.

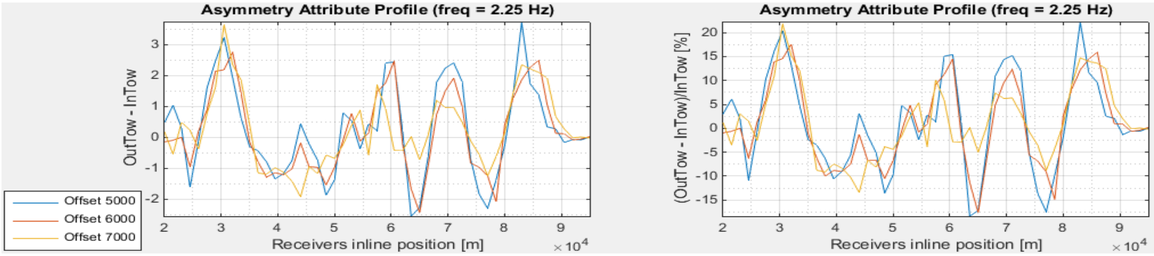

Figure 61. Non-normalized and normalized Asymmetry attribute profile at 2.25 Hz and offsets of 5000, 6000 and 7000 m.

The asymmetry attribute profile at offsets of 5000 m, 6000 m and 7000 m (Figure 61) shows relatively similar trend in signature as that profiled at frequencies of 1.25 Hz and 0.25 Hz with slight change in the position of the actual and local maximum and minimum. Based on the asymmetry attribute response, other possible discontinuities not seen at the other frequencies (i.e., lower frequencies and long offset) will begin to illuminate at this higher frequency and long offsets. The signature of the asymmetry attribute response also suggests the presence of possible resistors in the simulated subsurface and based on the number of actual and local maximums and minimum and the newly illuminated feature, the earlier inference about possible existence of at least three resistors/resistive layers in the subsurface is justified. The actual and local maximums and minimums are at receiver inline positions 30,500 m, 44,000 m, 57,500 m and 77,000 m respectively while the newly illuminated minor peak at the left is at receiver inline position 23,000 m and the relatively minor peak at the right is at receiver inline position 83,000 m. These inline positions corresponds to Rx8 and Rx17 for actual maximum and minimum, Rx26 and Rx39 for relative maximum and minimum. The minor peak at the left of the profile is at Rx3 while that at right of the profile is at Rx43. The locations of the actual and local maximum and minimum and the relatively minor peaks is expected to correspond to the boundaries of the inferred resistors.

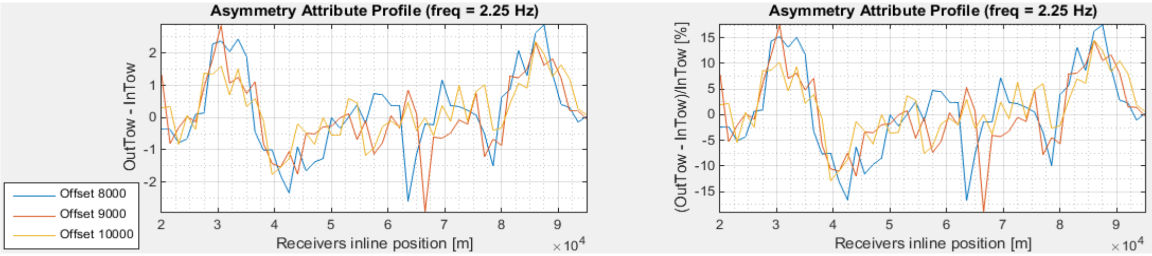

Figure 62. Non-normalized and normalized Asymmetry attribute profile at 2.25 Hz and offsets of 8000, 9000 and 10000 m.

Similar to the asymmetry attribute response at frequency of 1.25 Hz in Figure 56, there is an obvious increased attenuation in the asymmetry attribute response as the offset progressively increase to 8000 m, 9000 m and 10000 m as seen in Figure 62. This high variation in the attribute response could be as a result of contributions by the attenuation effect of the sea water at very long offsets, which could mar the output or information deduced from the asymmetry attribute profile. Nevertheless, the general trend in the asymmetry profile is similar to that profiled at shorter offset, for example in Figure 61.

Figure 63 and Figure 64 below are the asymmetry attribute computed and profiled at integrated range of offsets for the non-normalized and normalized computation approach and at frequency of 2.25 Hz.

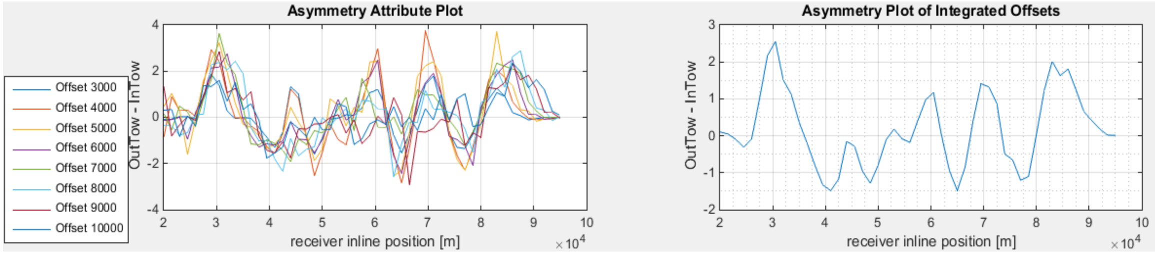

Figure 63. Non-normalized Asymmetry profile at integrated range of offsets for frequency of 2.25 Hz.

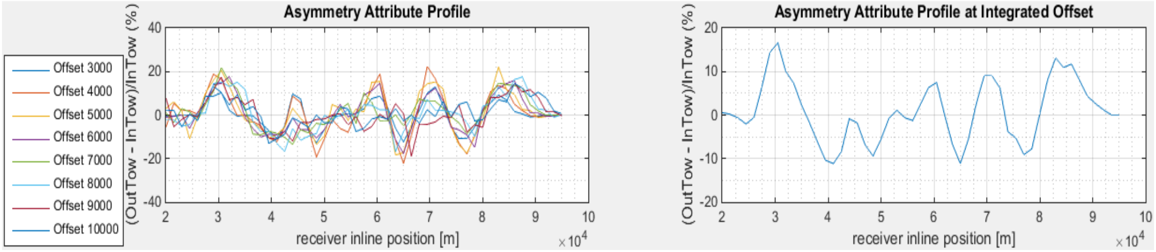

Figure 64. Normalized Asymmetry profile at integrated range of offsets for frequency of 2.25 Hz.

The signature of the asymmetry attribute computed and profiled at a range of integrated offsets (Figure 63 and Figure 64) and at this frequency (2.25 Hz), shows a clearly similar trend for both computational approach. At this high frequency of 2.25 Hz, there is a slight shift in the locations of the actual maximum and minimum but the relative maximum and minimum and the minor peak are in exact same position as that of frequency of 1.25 Hz. The locations of the actual maximum and minimum are at 30,500 m and 41,000 meters, corresponding to Rx8 and Rx15 respectively. The slight change in the relative positions can be related to possible existence of overlapping resistive layers in the simulated subsurface. Again, the clear qualitative similarity in the trends suggests the possibility of resistive layers between Rx8 and Rx15; and between Rx34 and Rx39, with another resistive anomaly starting from Rx43.

4.4.GOM Dataset Phase Processing Results

The outcome of the GOM dataset processing involving the phase component of the electric field are presented and discussed in this section.

4.4.1. PVO PLOTS ANALYSIS

The first set of figures show the results of the extracted phase component mapped at different receivers-transmitters distances (offsets) and at the different acquisition frequencies, i.e., the phase versus offset profiles. Figure 65, Figure 66 and Figure 67 presented here are for analysis and discussion of the noticeable trend of the recorded phase. Each figure illustrates the phase component of the electric field versus offsets for each receiver at the frequencies utilized in the simulated mCSEM acquisition, i.e., 0.06 HZ, 0.18 Hz, 0.125 Hz, 0.25 Hz and 2.25 Hz.

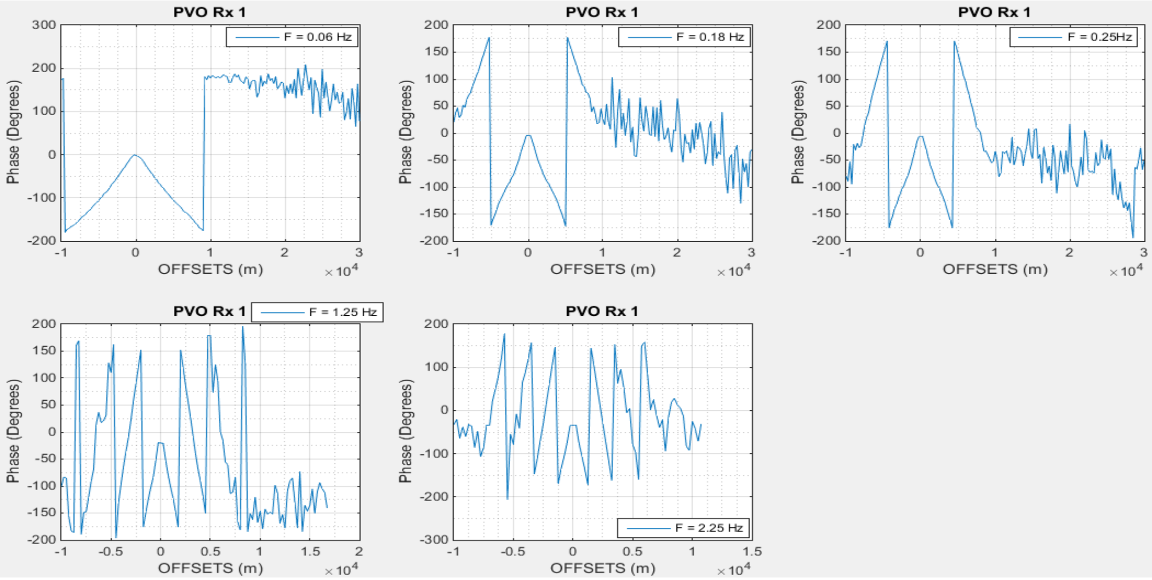

Figure 65. Phase versus Offset of Rx1 showing phase variations at different acquisition frequency.

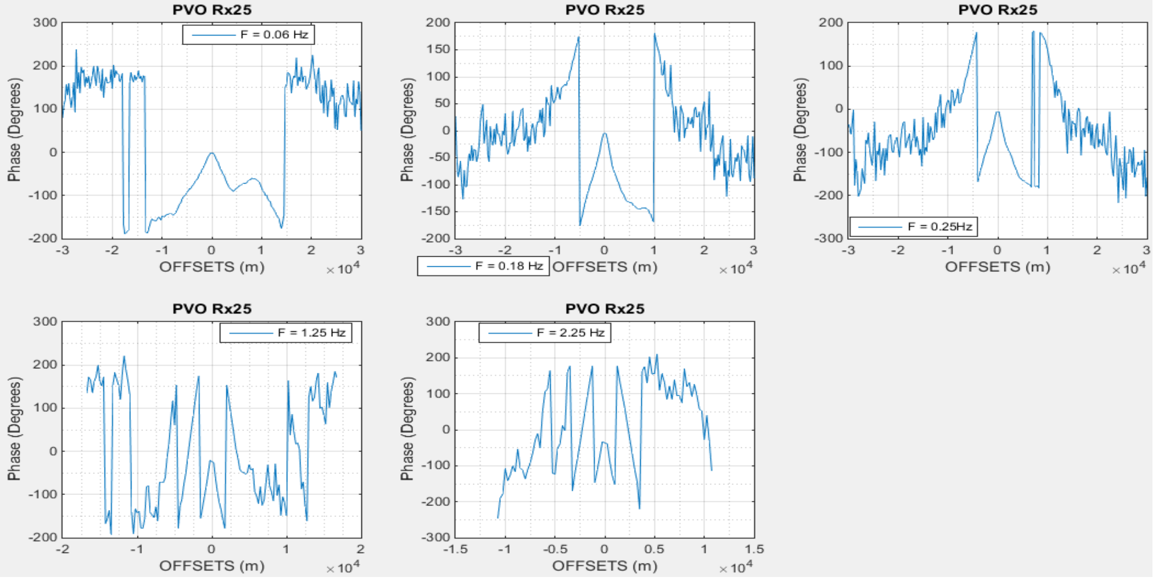

Figure 66. Phase versus Offset of Rx25 showing phase variations at different acquisition frequency.

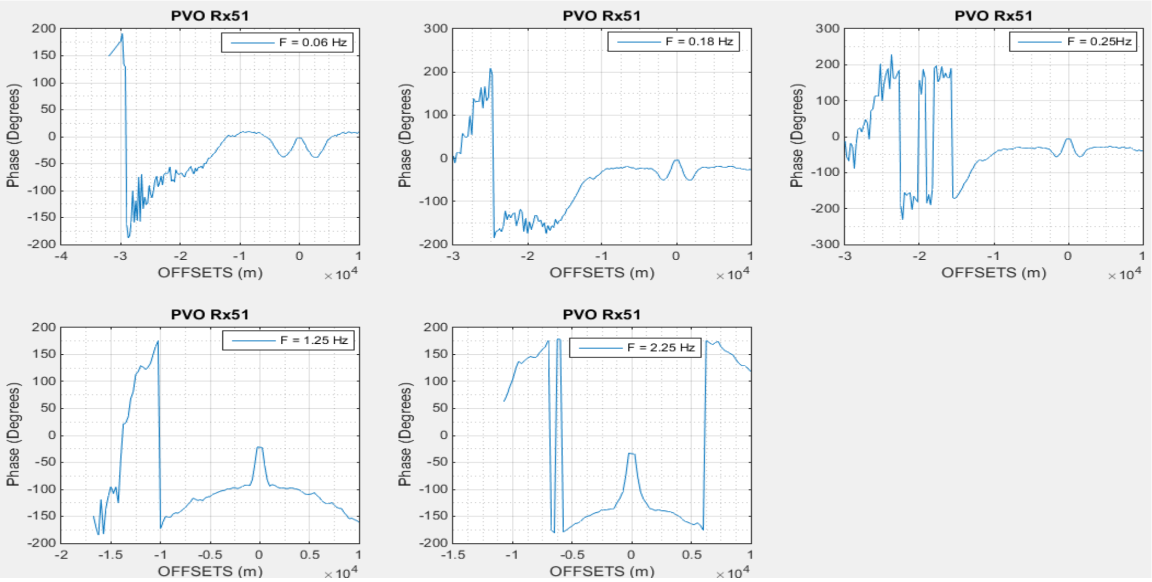

Figure 67. Phase versus Offset of Rx51 showing phase variations at different acquisition frequency.

The phase profile represented in Figure 65, Figure 66 and Figure 67 above, reveals quite same information as regards the repeated attenuation and high continuous variations of the measured phase response. Depending on the offset (short or long) and frequency being considered the attenuation of the recorded phase is either increasing or decreasing with high jumps of full cycle noticeably present. The information obtained from the phase versus offsets plots forms the basis for further processing carried out on the phase in order to extract reasonable information about the simulated subsurface. Other receivers PVO plots show similar trend to the ones presented here thus same or similar information is obtained when other receivers are considered.

4.4.2. UNWRAPPED PHASE

Figure 68 and Figure 69 shows lines of the phase map obtained after unwrapping the phase component of the electric field observation at specified offset and frequency.

Parallel green lines indicates the specified offset of interest at which the phase data is being unwrapped The phase data recorded by the other receivers were also unwrapped and qualitatively similar outcome to that of Rx40 and Rx9 explained below was obtained.

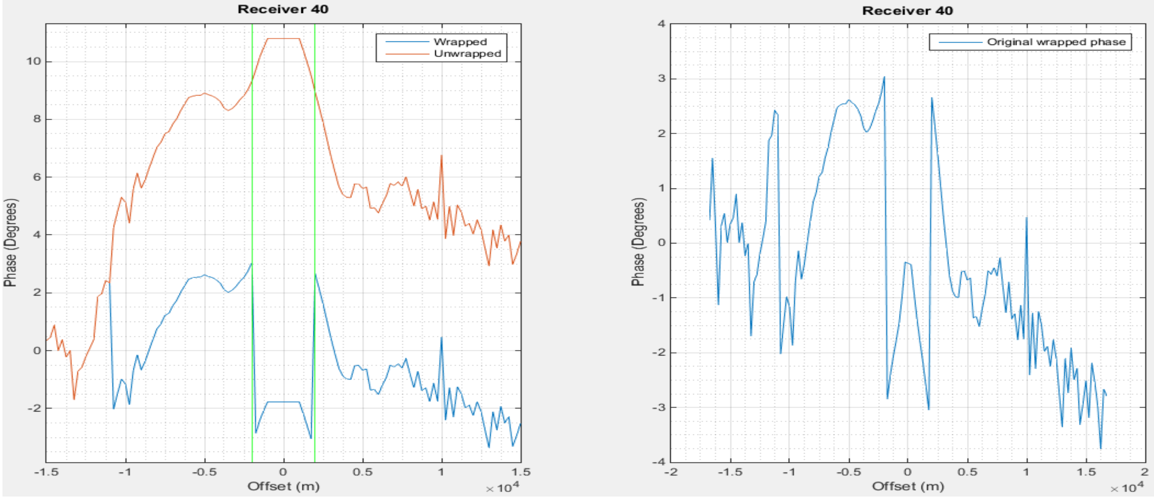

Figure 68. Phase unwrapping of Rx40 at frequency 1.25 Hz and offset 2000 m.

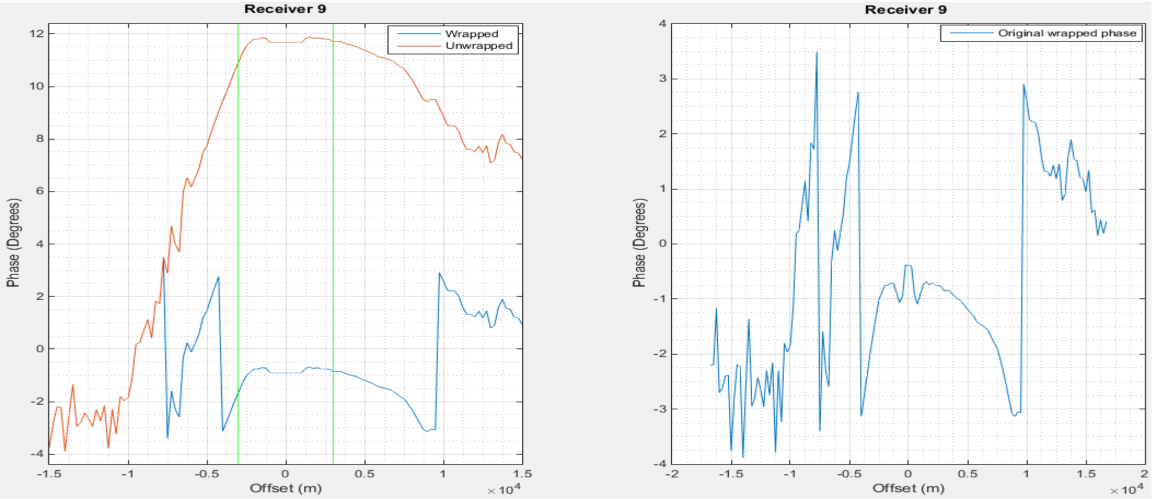

Figure 69. Phase unwrapping of Rx9 at frequency 1.25 Hz and offset 3000 m.

The measured phase which shows a highly varying trend suggests the presence of noise which is marring the information carried by the transmitting phase. This bias in the recorded phase which is possibly as a result of contributions of the air wave from the direct arrival is removed, restoring the physical continuity of the phase as seen in the figures. This continuous phase obtained after reconstruction and suppression of the jumps in the originally measured phase data is important for reliable results to be obtained in the subsequent asymmetry attribute computations and profiling.

4.4.3. PHASE ASYMMETRY PROFILE ANALYSIS

For the phase asymmetry attribute profile, two different frequencies i.e. low frequency of 0.25 Hz and high frequency of 2.25 Hz at short and long offsets are considered for analysis and discussion. At other frequencies and offsets, the same qualitative similarity seen in the asymmetry attribute profiles of 0.25 Hz and 2.25 Hz exists. Therefore, same information is obtainable.

4.4.3.1. Frequency of 0.06 Hz

Figure 70 and Figure 71 shows the non-normalized and normalized asymmetry attribute computed and profiled with the phase component of the electric field observation at low acquisition frequency of 0.06 Hz.

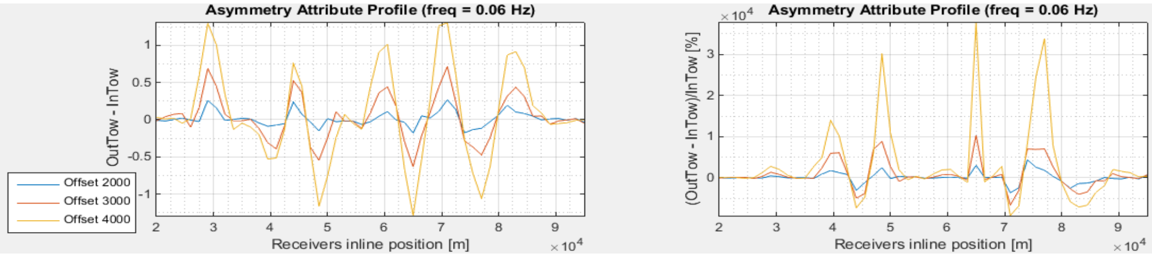

Figure 70. Non-normalized and normalized Phase Asymmetry attribute profile at 0.06 Hz and offsets of 2000, 3000 and 4000 m.

The non-normalized phase asymmetry attribute computed at short offsets of 2000 m, 3000 m and 4000 m (Figure 70) shows qualitatively similar trend to asymmetry attribute computed with the magnitude of the electric field at same frequency and combination of offsets as can be seen in Figure 36. The locations of the actual maximum and minimum are noticeably within same receiver inline positions, revealing similar information about the possibly embedded resistors. This qualitative similarity between the trend of the asymmetry attribute computed with the phase component and that computed with the magnitude component of the electric field justifies the earlier inference that at least three resistors or resistive layers exists in this simulated subsurface. The trend of the phase response also reveals other ups and down which suggests presence of other possible resistors in the simulated subsurface. On the other hand when normalized, the asymmetry attribute response is obscured thus doesn't provide any reasonable and reliable information as regards possible resistive layers. This obscurity in trend is possibly caused by the frequent change in the sign (positive and negatives) of the extracted in-towing and out-towing phase data which causes frequent change in sign of the computed ratio with high order of magnitude.

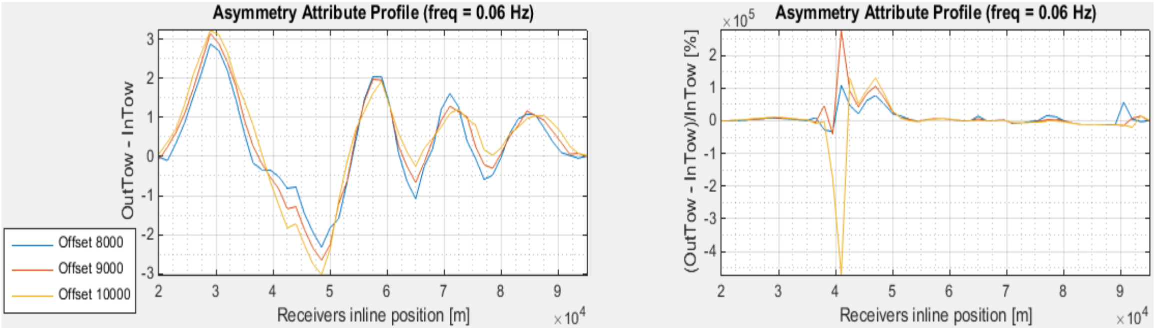

Figure 71. Non-normalized and normalized Phase Asymmetry attribute profile at 0.06 Hz and offsets of 8000, 9000 and 10000 m.

Also, when asymmetry attribute is computed with the phase data at very long offsets (Figure 71), there is a noticeable qualitative congruence in the trend with the asymmetry attribute computed with the magnitude component of the electric field at same frequency and combination of long offset as can be seen in Figure 38. The locations of the opposite polarities i.e., the inferred possible boundaries of the suggestive resistive layers are seen to be around almost same receivers i.e., at Rx7 and Rx20; Rx26 and Rx39, and one starting at Rx44 respectively. On the other hand, the normalized computational approach showed relatively obscured attribute response, with absolutely unreliable information about the subsurface layers of the simulated area.

Figure 72 and Figure 73 below shows the phase asymmetry attribute computed and profiled at integrated range of offsets for the non-normalized and normalized computation approach and frequency of 0.06 Hz.

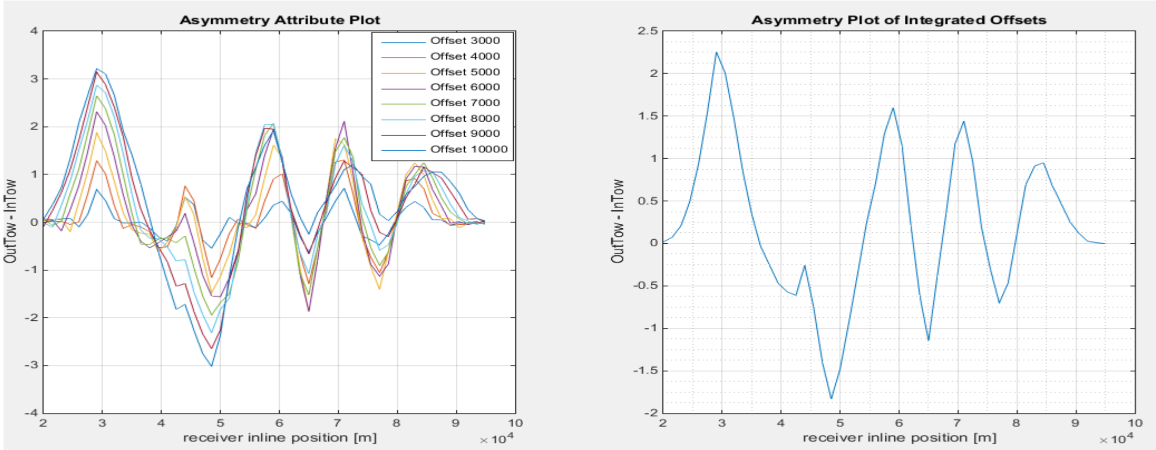

Figure 72. Non-normalized phase Asymmetry profile at integrated range of offsets for frequency of 0.06 Hz.

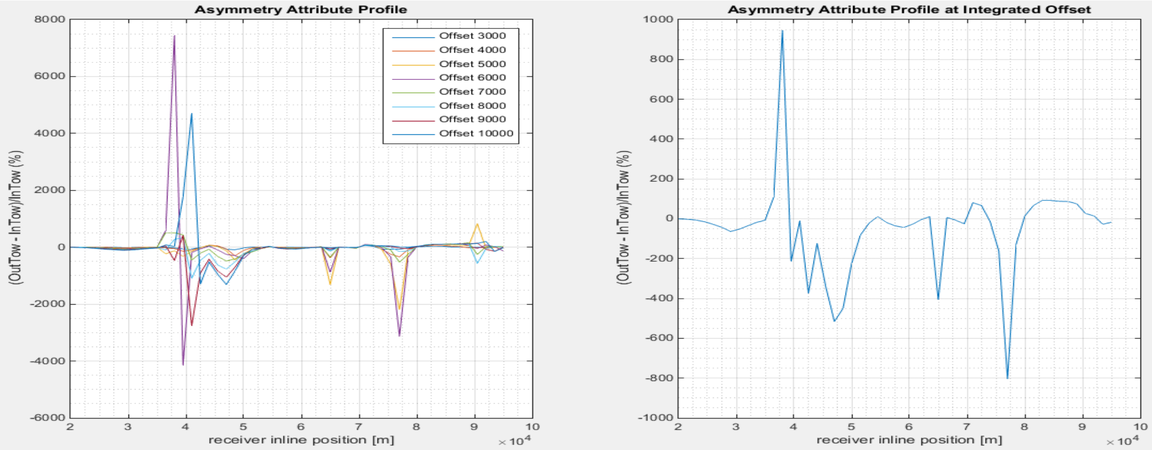

Figure 73. Normalized phase Asymmetry profile at integrated range of offsets for frequency of 0.06 Hz.

At integrated range of offsets, the phase asymmetry attribute computed with the non-normalized approach show relatively clear qualitative similarity to that computed with the magnitude component of the electric field observations in Figure 40. The locations of the actual maximum and minimum and other peak is clearly illuminated, tallying with the information obtained when the asymmetry attribute was computed with the magnitude at the same frequency and range of offsets. The normalized computation (Figure 73) gives no reasonable or reliable information as regards the features in the subsurface. As earlier mentioned, the obscurity in the response is possibly as a result of the frequent change in the sign (positive and negatives) of the extracted in-towing and out-towing phase data which causes frequent change in sign of the computed ratio with high order of magnitude.

4.4.3.2. Frequency of 2.25 Hz.

Figure 74 and Figure 75 shows the non-normalized and normalized asymmetry attribute computed and profiled with the phase component of the electric field observation at high acquisition frequency of 2.25 Hz.

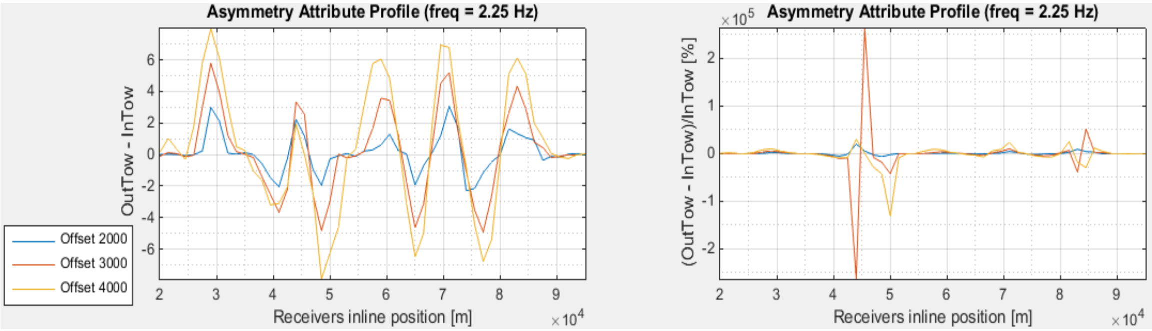

Figure 74. Non-normalized and normalized Phase Asymmetry attribute profile at 2.25 Hz and offsets of 2000, 3000 and 4000 m

The non-normalized phase asymmetry attribute computed at short offsets of 2000 m, 3000 m and 4000 m (Figure 74) shows qualitatively similar trend to asymmetry attribute computed with the magnitude of the electric field at same frequency and combination of offsets as can be seen in Figure 60. The trend of the phase asymmetry attribute response also reveals almost same possible positions of opposite polarity thus suggesting similar information as regards the presence of resistive layers in the simulated subsurface. On the other hand, when normalized, the asymmetry attribute response is also obscured and doesn't provide any reasonable and reliable information as regards possible resistive layers. As earlier mentioned, this obscurity in trend is possibly caused by the frequent change in the sign (positive and negatives) of the extracted in-towing and out-towing phase data which causes frequent change in sign of the computed ratio with high order of magnitude.

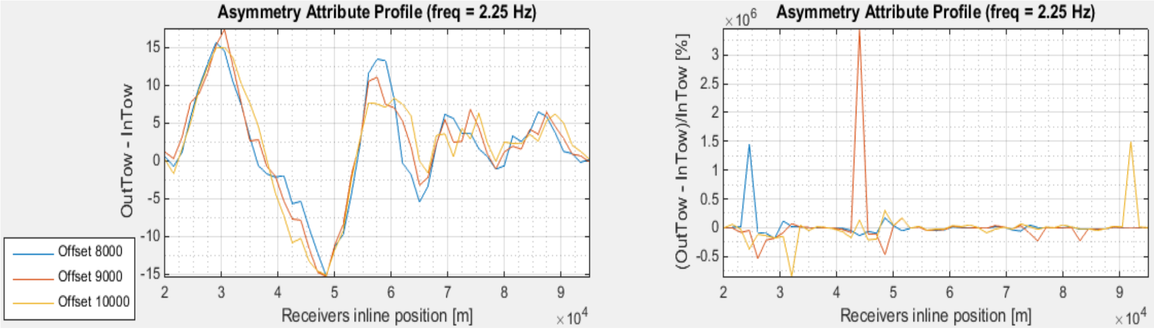

Figure 75. Non-normalized and normalized Phase Asymmetry attribute profile at 2.25 Hz and offsets of 8000, 9000 and 10000 m.

Also, when asymmetry is computed with the phase at very long offsets (Figure 75), there is a qualitative congruence in the trend with the asymmetry attribute computed with the magnitude of the electric field at this same frequency and combination of long offsets as can be seen in Figure 62. Though the phase asymmetry attribute profile show a less attenuation in the trend of the response when compared to the magnitude asymmetry attribute profile, the possible boundaries of the suggestive resistive layers are seen to be within the same inferred receivers in the analysis of the asymmetry profile computed with the magnitude component of the electric field. Also, the normalized computational approach shows relatively high obscured attribute response, with absolutely unreliable information about the subsurface layers of the simulated area.

Figure 76 and Figure 77 shows the phase asymmetry attribute computed and profiled at integrated range of offsets for the non-normalized and normalized computation approach and frequency of 2.25 Hz.

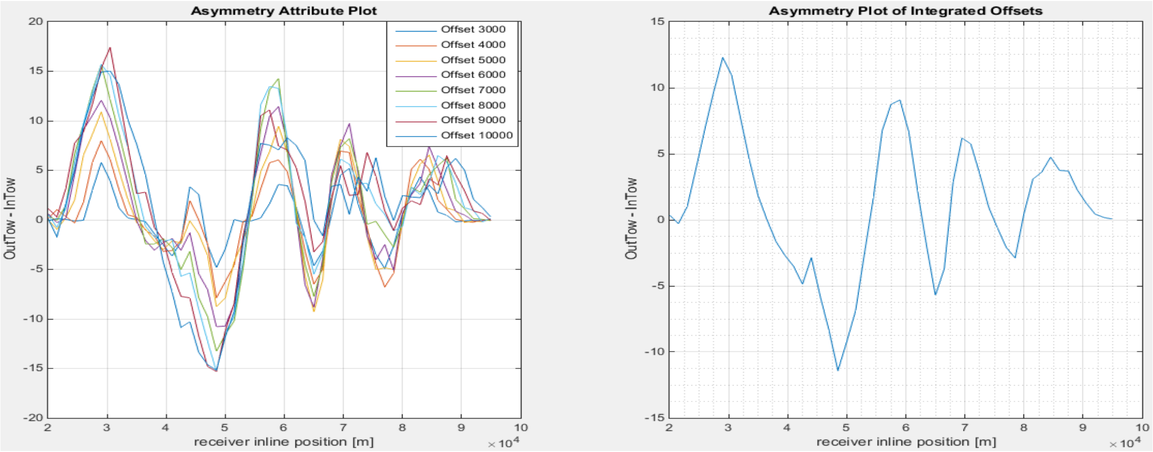

Figure 76. Non-normalized phase Asymmetry profile at integrated range of offsets for frequency of 2.25 Hz.

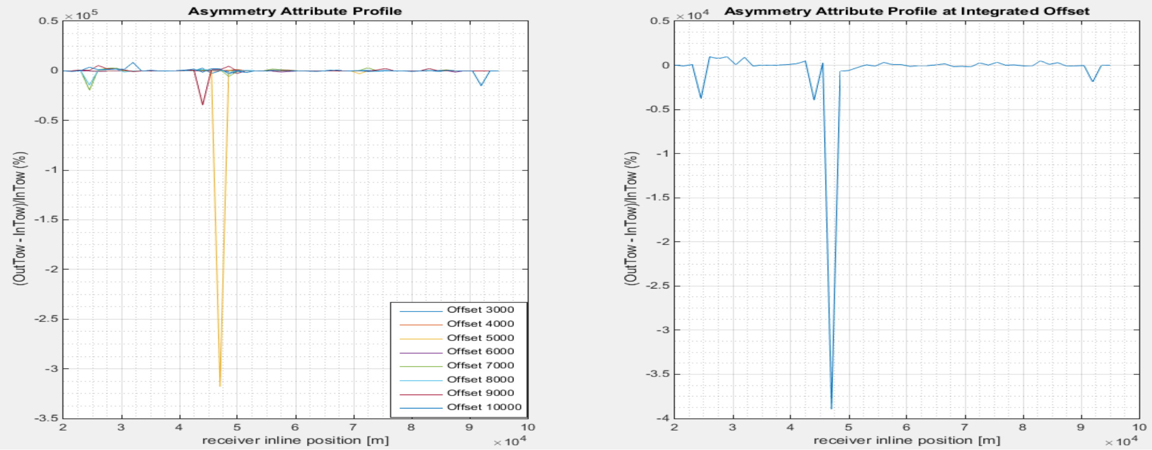

Figure 77. Normalized phase Asymmetry profile at integrated range of offsets for frequency of 2.25 Hz.

At integrated range of offsets, the phase asymmetry attribute computed with the non-normalized approach (Figure 76) reveals reliable information about the possible existence of subsurface resistors which is relatively similar to the information obtained from the asymmetry attribute computed at integrated range of offsets with the magnitude of the electric field observation. On the other hand, no reasonable information is obtainable from the phase asymmetry attribute computed with the normalized approach at integrated range of offsets (Figure 77) most probably due to same reasons earlier stated in the analysis and discussion of the normalized phase asymmetry attribute at the considered offsets and frequencies.

5. CONCLUSION AND RECOMMENDATIONS

5.1. CONCLUSION

The analysis of the asymmetry attribute extracted from both the magnitude and phase components of the electric field at different frequencies and offsets for the canonical model data showed a qualitative congruence in the location of the symmetry response and the position of the resistive anomaly in the provided 2.5D model as can be seen in the superimposed plot of Figure 78.

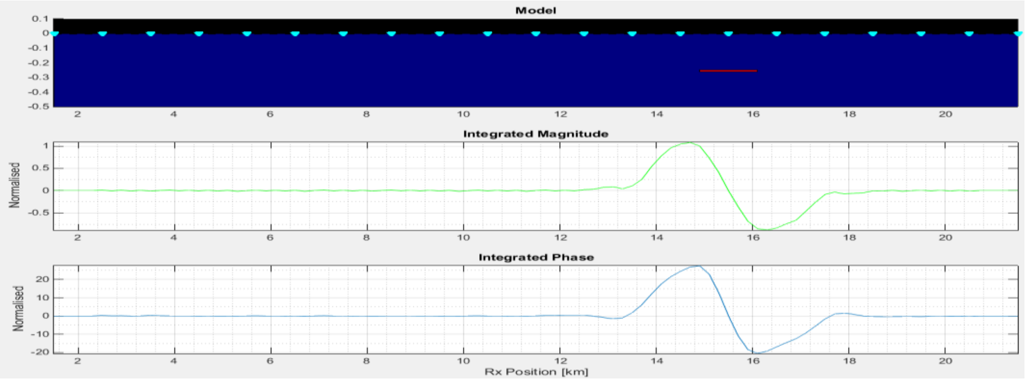

Figure 78 Superimposed resistivity model and normalised asymmetry plots of magnitude and phase data.

In fact, the locations of the absolute maximum and minimum of the asymmetry attribute response appear at the position of opposite polarity of the discontinuity, i.e., the embedded resistor in the 2.5D model of figure 1. This congruence in the positions of the asymmetry response and the embedded resistor validates the efficacy of the proposed approach as a fast imaging tool.

Based on the analysis carried out on the GOM dataset, the inferred and suggested boundaries of the possible resistive layers or resistors embedded in the subsurface appear to be within the same location and covered by the same receivers at all frequencies and differing offsets for the asymmetry attribute computed with the magnitude and phase thus rendering the obtained results relatively valid.

The GOM dataset probabilistic conclusion is based on the unavailability of true subsurface resistive model and/or the true seismic section along the CSEM line crossing the simulated prospect, which should provide clear and real pictorial information about the embedded resistors and their boundaries. The true model and the seismic section would have made it possible for a realistic comparative conclusion (i.e., with the asymmetry attribute responses) to be reached with a high level of certainty knowing that the boundaries of any existing discontinuities (based on the true model and seismic section) should/would correlate with the locations of the actual and relative maximums and minimums and any other peaks revealed by the asymmetry attribute profiles analyzed in this thesis. Nevertheless, the results obtained from the analysis of this dataset are comparatively valid based on the theory of interpretation of the asymmetry attribute proposed in literatures.

Also, the asymmetry attribute computed on the phase (GOM dataset) being qualitatively similar to that computed with the magnitude, can represent a useful tool for supporting the analysis of mCSEM data thus increasing the degree of certainty in decision making about drilling prospects.

Finally, the analysis of the asymmetry attribute carried out in this thesis provides not just the synoptic view of the simulated subsurface but also a base for quality checking and quality control of the mCSEM dataset for possible noise and/or artefacts. As seen from the analysis of the MVO and PVO plots of the GOM data, the noise in the data was highlighted at high offsets in some of the receivers, which was later evident in the computed asymmetry attribute at high offsets and frequencies.

5.2. RECOMMENDATIONS

The phase asymmetry attribute profile should be considered while making decisions about the lateral distribution of resistors in the subsurface when analyzing mCSEM data.

The normalized phase should be re-evaluated to determine possible approach to remove the obscurity in the phase response of the asymmetry attribute profiles, so as to obtain reasonable and reliable information of the subsurface layers.

Future studies on the phase measurements should be carried out on real dataset with the true resistive model or seismic section of the prospect made available so that obtained results will/can be clearly justified.

In subsequent studies, asymmetry attribute should be extracted and computed for a selected range of receivers and/or receiver inline positions, so as to obtain a clear trend in the profiled response.

Bibliography

Andréis, David, and Lucy MacGregor. "Controlled-source electromagnetic sounding in shallow water: Principles and applications." *Geophysics 73, no.1*, 2007: F21-F32.

Avdeeva, Anna, Micheal Commer, and A. Gregory. "Hydrocarbon reservoir detectability study for marine CSEM methods: time domain versus frequency domain." *In SEG 2007 Annual Meeting, SEG, San Antonio,*, 2007: 628-632.

Black, Noel, and Micheal S. Zhdanov. "Monitoring of hydrocarbon reservoirs using marine CSEM method." *In SEG Technical Program Expanded Abstracts: 79th Annual International Meeting*, 2009: 850-854.

Boerner, David E. "Controlled source electromagnetic deep sounding: Theory, results and correlation with natural source results." *Surveys in geophysics 13, no. 4-5*, 1992: 435-488.

Chave, Alan D., Steven C. Constable, and R. Nigel Edwards. "Electrical exploration methods for the seafloor." *Society of Exploration Geophysicists* Electromagnetic methods in applied geophysics , Volume 2 (1991): 931-966.

Chiadikobi, K.C., Chiaghanam O. I., Omoboriowo A.O., Etukudoh M.V., and Okafor N. A. "Detection of hydrocarbon reservoirs using the Controlled-source Electromagnetic (CSEM) method in the “BETA” field deep water offshore Niger delta, Nigeria." *International Journal of Science & Emerging Technologies 3, no.1*, 2012.

Chopra, Satinder, Kurt Strack, Cengiz Esmersoy, and Normal Allegar. "Introduction to this special section: CSEM." *The Leading Edge 26, no. 3:*, 2007: 323 -325.

Constable, S. and Cox, C. "Marine controlled source electromagnetic sounding - II:The PEGASUS experiment." *Journal of Geophysical Research, 92*, 1996: 5519-5530.

Constable, Steven. "Marine EM Methods." *Search and Discovery Article #40175*, 2005.

Constable, Steven, and Leonard J. Srnka. "An introduction to marine controlled-source electromagnetic methods for hydrocarbon exploration." *Geophysics 72, no. 2:*, 2007: WA3-WA12.

Constable, Steven. "Marine electromagnetic methods—A new tool for offshore exploration." *The Leading Edge 25, no. 4:* , 2006: 438-444.

Cox, C. S., Constable, S. C., Chave, A. D., and Webb, S. C. "Conrolled source electromagnetic sounding of the oceanic lithosphere." *Nature, 320*, 1986: 52-54.

Cox, C. S., Filloux, J. H., and Larsen, J. "Electromagnetic studies of ocean currents and electrical conductivity below the ocean floor." Edited by A. In Maxwell. *The Sea,* (John Wiley) 4 (1971): 637–693.

Dawoud, Mohamed, Stephen Hallinan, Rolf Herrmann, and Frank van Kleef. "Near-surface electromagnetic surveying." *Oilfield Review 21, no. 1*, 2009.

De Lerma, D., M. Fedi, L. Mapelli, and P. Dell’Aversana. "Singular Function Normalization-A Method for a Fast International of CSEM Data." *In 75th EAGE Conference & Exhibition incorporating SPE EUROPEC* , 2013.

Dell’Aversana, P., and F. Zanoletti. "Accurate detection of reservoir boundaries using electromagnetic attributes and inversion of marine CSEM data." *In 70th EAGE Conference & Exhibition*, 2008.

Dell’Aversana, P., and F.Zanoletti. "Multi-frequency symmetry analysis of marine CSEM data for separating the effects of multiple resistors." *In EGM 2010 International Workshop*, 2010.

Dell’Aversana, Paolo. "Accurate detection of resistivity anomalies using the symmetry attribute and inversion of marine CSEM data." *The Leading Edge 29, no. 6*, 2010: 662-669.

Dell’Aversana, Paolo. "Marine CSEM data interpretation: Pitfalls and possible solutions." *The Leading Edge 26, no. 6*, 2007: 686-691.

Dell’Aversana, Paolo. "Marine CSEM in shallow water: acquisition and interpretation strategies." *In 2006 SEG Annual Meeting. Society of Exploration Geophysicists*, 2006.

Dell’Aversana, Paolo. "The importance of using geometrical constraints in marine Controlled Source Electromagnetic data inversion." *In 75th SEG meeting, Houston, Texas, Expanded Abstracts, EMP, vol. 1*, 2005.

Dell’Aversana, Paolo, and Francesco Zanoletti. "Spectral analysis of marine CSEM data symmetry." *First Break 28, no. 3*, 2010.

Edwards, Nigel. "Marine controlled source electromagnetics principles, methodologies, future commercial applications." *Surveys in Geophysics 26, no. 6* , 2005: 675-700.

Eidesmo, T., S. Ellingsrud, L. M. MacGregor, Sinha Constable, M. C. Sinha, S. E. Johansen, F. N. Kong, and H. Westerdahl. "Sea bed logging (SBL), a new method for remote and direct identification of hydrocarbon filled layers in deepwater areas." *First break 20, no. 3* , 2002.

Ellingsrud, S., T. Eidesmo, S. Johansen, M. C. Sinha, L. M. MacGregor, and S. Constable. "Remote sensing of hydrocarbon layers by seabed logging (SBL): Results from a cruise offshore Angola." *The Leading Edge 21, no. 10:*, 2002: 972-982.

Ellingsrud, S., T.Eidesmo, and K.M. Strack. "CSEM: a fast growing technology." *Presented at the 78th Annual International Meeting*, 2008.

Gola, Andrea, and Giancarlo Bernasconi. "Quick qualitative CSEM data interpretation." *Signal 500, no. 700*, 2014: 1000.

Greer, A. A., L. M. MacGregor, and R. Weaver. "Remote mapping of hydrocarbon extent using marine Active Source EM Sounding." *In 65th EAGE Conference & Exhibition*, 2003.

Hesthammer, Jonny, Aristofanis Stefatos, Stein Fanavoll, and Jens Danielsen. "The Performance of CSEM as a De-risking Tool In Oil and Gas Exploration." *in 2010 SEG Annual Meeting. Society of Exploration Geophysicists*, 2010.

James, Brady, T. Campbell, A. Fenwick, M. Ganz, S.K. Sandberg, M.P.P Buonora, L.P Rodrigues, C. Campbell, L. Combee, A. Ferster, K.E. Umbach, T. Labruzzo, A. Zerilli, E.A. Nicholas, S. Patmore and J. Stilling. "Electromagnetic Sounding for Hydrocarbons." *Schlumberger Oilfield Review*, Spring, 2009: 4-19.

Johansen, S. E., H. E. F. Amundsen, T. Røsten, S. Ellingsrud, T. Eidesmo, and A. H. Bhuiyan. "Subsurface hydrocarbons detected by electromagnetic sounding." *First Break 23, no. 3*, 2005.

Johansen, Ståle E., Tor A. Wicklund, and Hans E.F. Amundssen. "Interpretation example of marine CSEM data." *The Leading Edge 26, no. 3* , 2007: 348-354.

Kong, F.N., Westerdahl, H., Ellingsrud, S., Eidesmo, T. and Johansen, S. E. "Seabed logging: A possible direct hydrocarbon indicator for deepsea prospects using EM energy." *Oil & Gas Journal, May 2013*, 2002.

Løseth, Lars Ole. "Modelling of controlled source electromagnetic data." PhD Thesis, Trondheim, 2007.

MacGregor Lucy, Neville Barker, Andy Overton, Sam Moody, and Dave Bodecott. "Derisking exploration prospects using integrated seismic and electromagnetic data—A Falkland Islands case study." *The Leading Edge 26, no. 3:*, 2007: 356-359.

MacGregor, L. M. and Sinha, M. C. "Use of marine controlled source electromagnetic sounding for sub-salt exploration." *Geophysical Prospecting, 48:*, 2000: 1091–1106.

MacLennan, Kristopher. "Methods for addressing noise and error in controlled source electromagnetic data." PhD Thesis, Colorado, 2013.

Mehta, Kurang, Misac Nabighian, Yaoguo Li, and Doug Oldenburg. "Controlled Source Electromagnetic (CSEM) technique for detection and delineation of hydrocarbon reservoirs: an evaluation." *In 2005 SEG Annual Meeting. Society of Exploration Geophysicists*, 2005.

Mittet, Rune. "Normalized amplitude ratios for frequency-domain CSEM in very shallow water." *First Break 26, no. 11*, 2008.

Mittet, Rune, and Jan Petter Morten. "Detection and imaging sensitivity of the marine CSEM method." *Geophysics 77, no. 6*, 2012: E411-E425.

Nguyen, A.K., S. Fanavoll, K.R. Hansen, J.P. Morten, and R. Tharimela. "EM anomaly detection under a high resistive, anisotropic overburden: Inversion study from the Nucula discovery in Barents Sea." *Geological Society of Norway conference: "Recent advances in interpretation of Geological data"*, 2009.

Osella, Ana, Matías de la Vega, and Eugenia Lascano. "3D electrical imaging of an archaeological site using electrical and electromagnetic methods." *Geophysics 70, no. 4 :*, 2005: G101-G107.

Palacky, G. J., I. L. Ritsema, and S. J. de Jong. "Electromagnetic Prospecting for Groundwater in Precambrian Terrains in the Republic of Upper Volta." *Geophysical Prospecting 29, no. 6:*, 1981: 932-955.

Peace, Dave, Dave Meaux, Mike Johnson, and Alan Taylor. "Controlled Source Electromagnetics for Hydrocarbon Exploration." 2004: 31-45.

Pethick, Andrew. *digital earth lab.* June 20, 2012. http://www.digitalearthlab.com (accessed May 10, 2015).

Pethick, Andrew. "Planning and 4d Visualisation of the Marine Controlled Source Electromagnetic Method." *Exploration Geophysics, Curtin University of Technology, Perth, Australia*, 2008.

Reynolds, John M. *An introduction to applied and environmental geophysics.* John Wiley & Sons, 2011.

Ridyard, Dave, Bjorn Petter Lindhom, and Tor Atle Wicklund. "Electromagnetic prospect scanning: The next frontier for exploration using Sea Bed Logging." *In 2006 SEG Annual Meeting. Society of Exploration Geophysicists*, 2006.

Roth, F., and F. Maaø. "Improving Seabed Logging Sensitivity in Shallow Water through Up-Down Separation." *In 69th EAGE Conference & Exhibition*, 2007.

Steven, Constable. "Ten years of marine CSEM for hydrocarbon exploration." *Geophysics 75, no. 5:*, 2010: 75A67-75A81.

Sundberg, Karl. "Electrical prospecting for oil structure." *AAPG Bulletin 14, no. 9*, 1930: 1145-1163.

Swift, C. M. "Fundamentals of the electromagnetic method: Electromagnetics in Applied Geophysics." *SEG*, 1991: 5-10.

Swift, Charles M. "Fundamentals of the electromagnetic method: Electromagnetics in applied geophysics." *SEG.*, 1988: 4-11.

Tite, M.S., and C. Mullins. "Electromagnetic Prospecting on archaeological sites using a soil conductivity meter." *Archaeometry 12, no. 1*, 1970: 97-104.

Tompkins, Michael J., and Richard Weaver. "Methods for the visualization and interpretation of marine controlled-source electromagnetic data." *In 2004 SEG Annual Meeting. Society of Exploration Geophysicists*, 2004.

Um, Evan Schankee, and David Lee Alumbaugh. "On the physics of the marine controlled-source electromagnetic method." *Geophysics 72, no. 2* , 2007: WA13-WA26.

Wait, James R. "A conducting sphere in a time varying magnetic field." *Geophysics 16, no. 4*, 1951: 666-672.

Young, Peter D., and Charles S. Cox. "Electromagnetic active source sounding near the East Pacific Rise." *Geophysical Research Letter 8, no. 10*, 1981: 1043-1046.

Appendix A

Canonical model Asymmetry Attribute Profiles

Figures showing non-normalized and normalized asymmetry attribute profiled at offsets of 1000 m and 2000 m for frequencies 0.25 Hz and 0.5 Hz respectively.

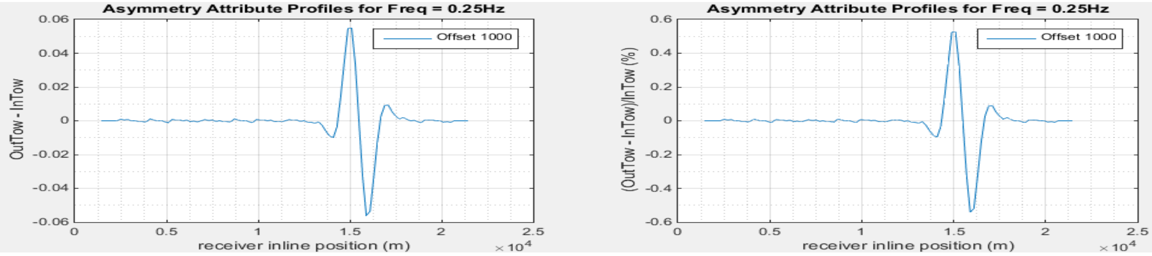

Figure 79. Non-normalized and normalized Asymmetry attribute profile at 0.25 Hz and offset of 1000 m.

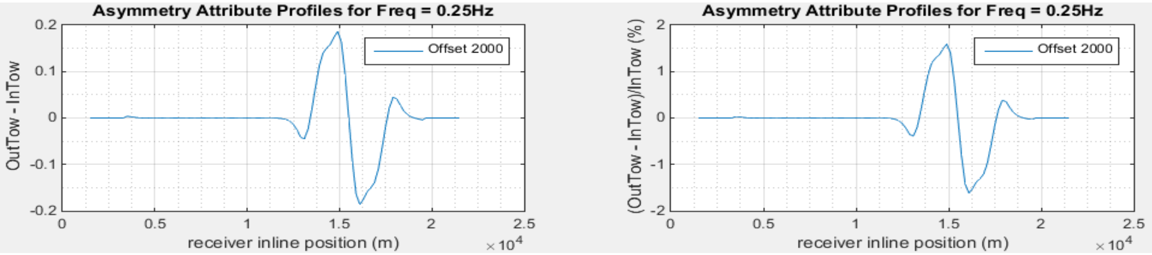

Figure 80. Non-normalized and normalized Asymmetry attribute profile at 0.25 Hz and offset of 2000 m.

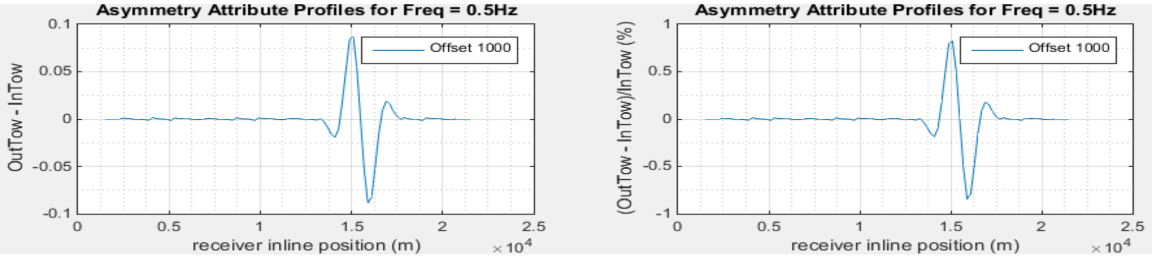

Figure 81. Non-normalized and normalized Asymmetry attribute profile at 0.5 Hz and offset of 1000 m.

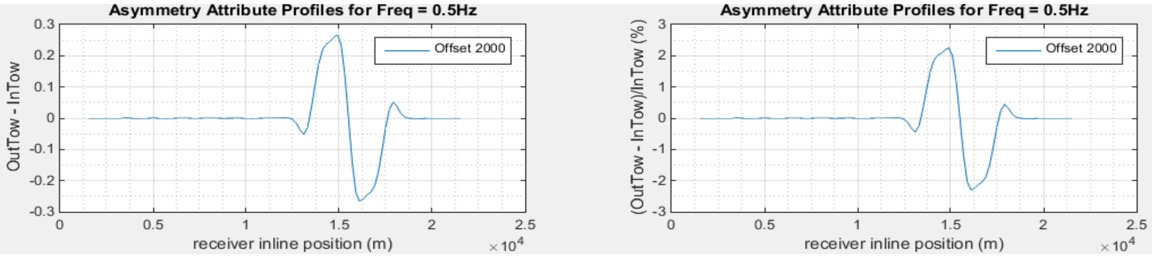

Figure 82. Non-normalized and normalized Asymmetry attribute profile at 0.5 Hz and offset of 2000 m.

Appendix B

GOM Benchmark Data MVO Plots

Mapped observations versus Rx-Tx distances at some of the receiver gather not shown in the results section are illustrated below for better understanding of the trend of the recorded magnitude component of the electric field observation.

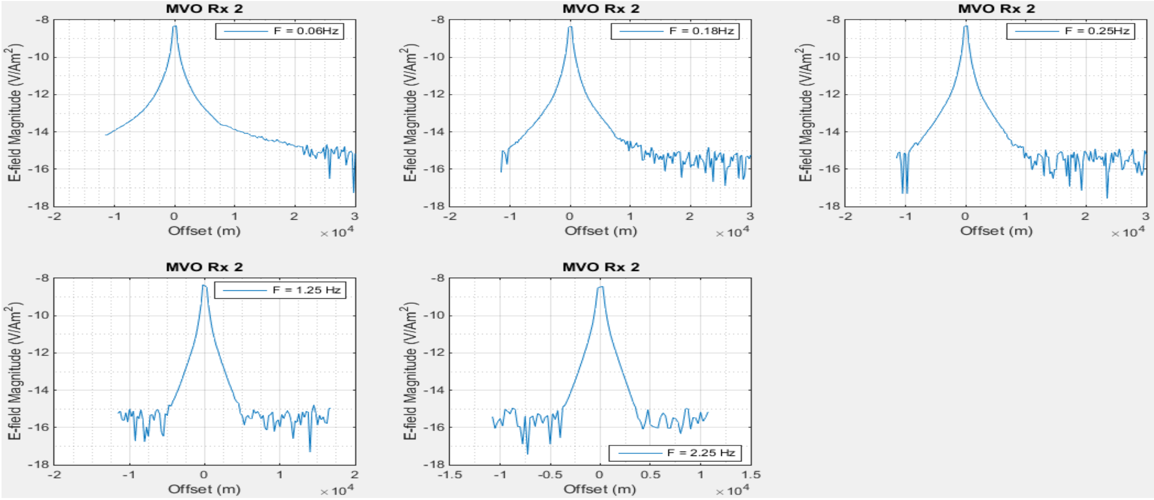

Figure 83. Magnitude versus Offset of Rx2 showing the resistive anomalous data at different acquisition frequency.

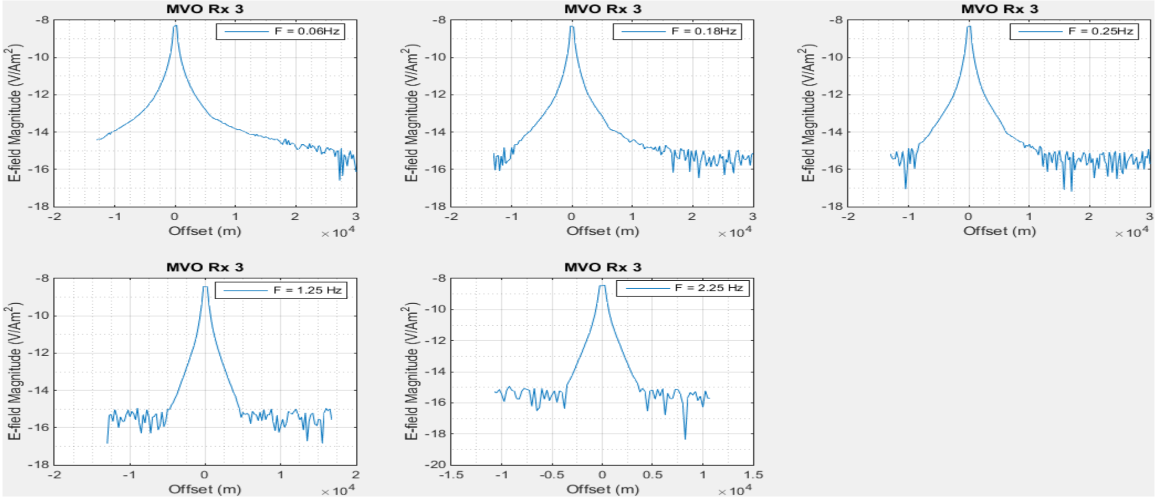

Figure 84. Magnitude versus Offset of Rx3 showing the resistive anomalous data at different acquisition frequency.

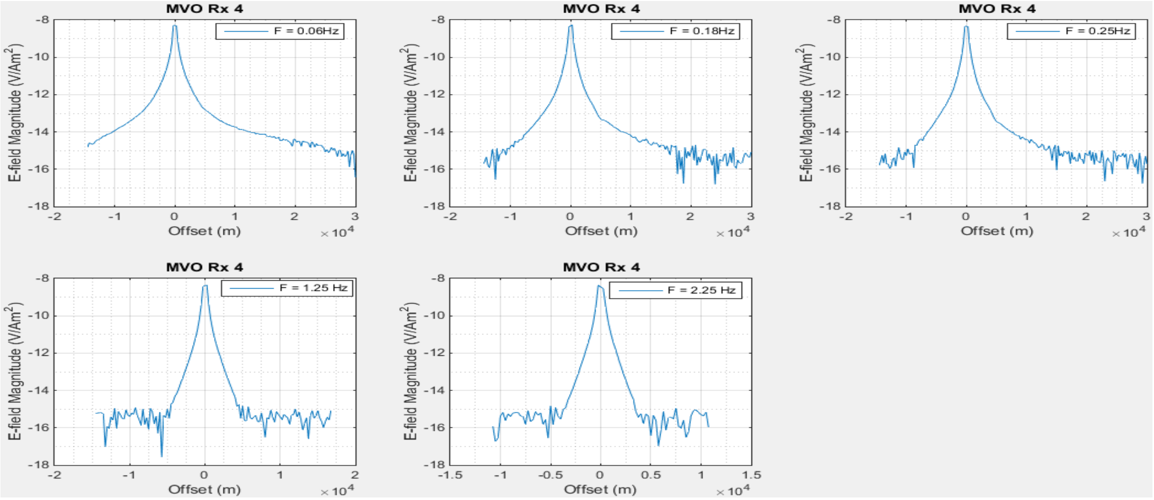

Figure 85. Magnitude versus Offset of Rx4 showing the resistive anomalous data at different acquisition frequency.

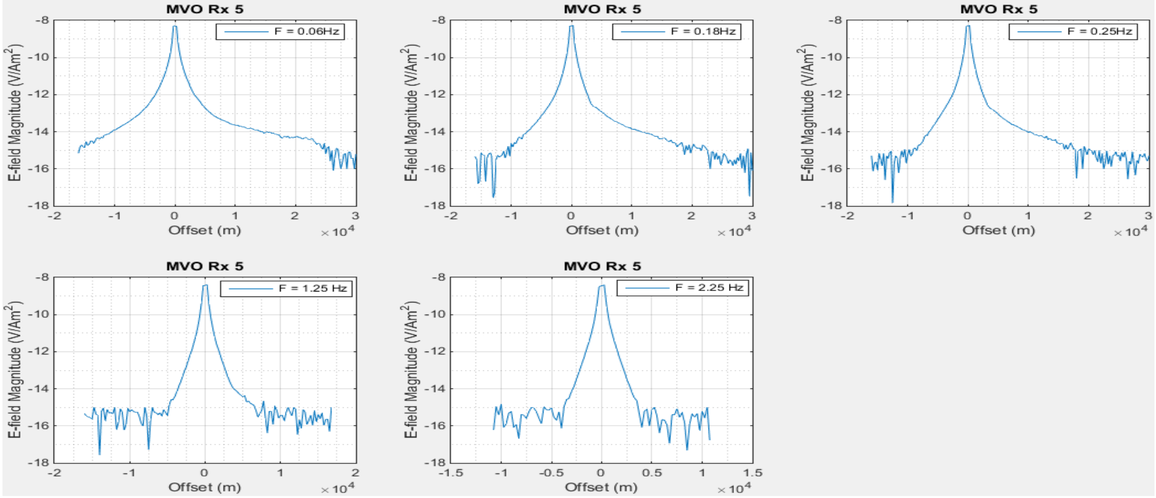

Figure 86. Magnitude versus Offset of Rx5 showing the resistive anomalous data at different acquisition frequency.

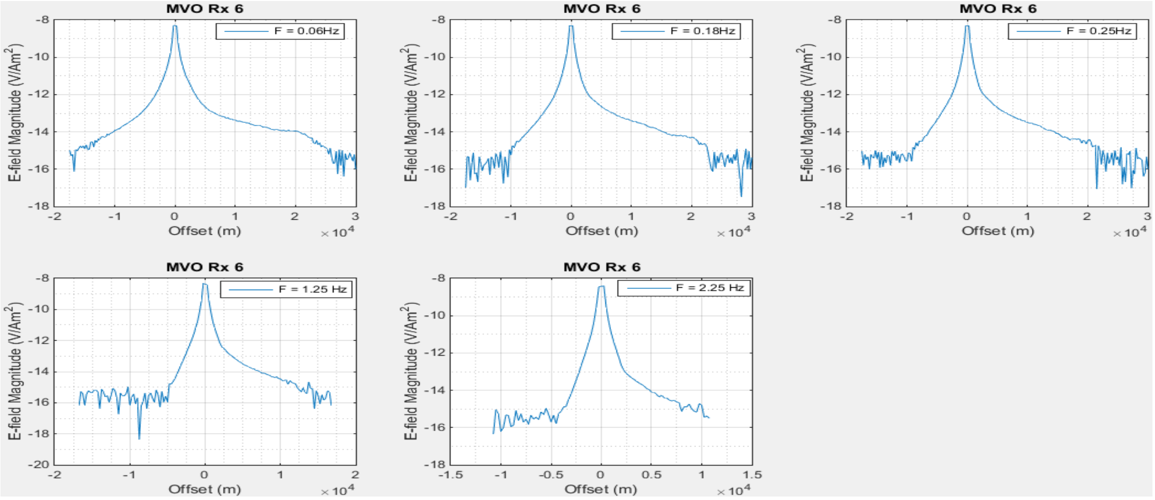

Figure 87. Magnitude versus Offset of Rx6 showing the resistive anomalous data at different acquisition frequency.

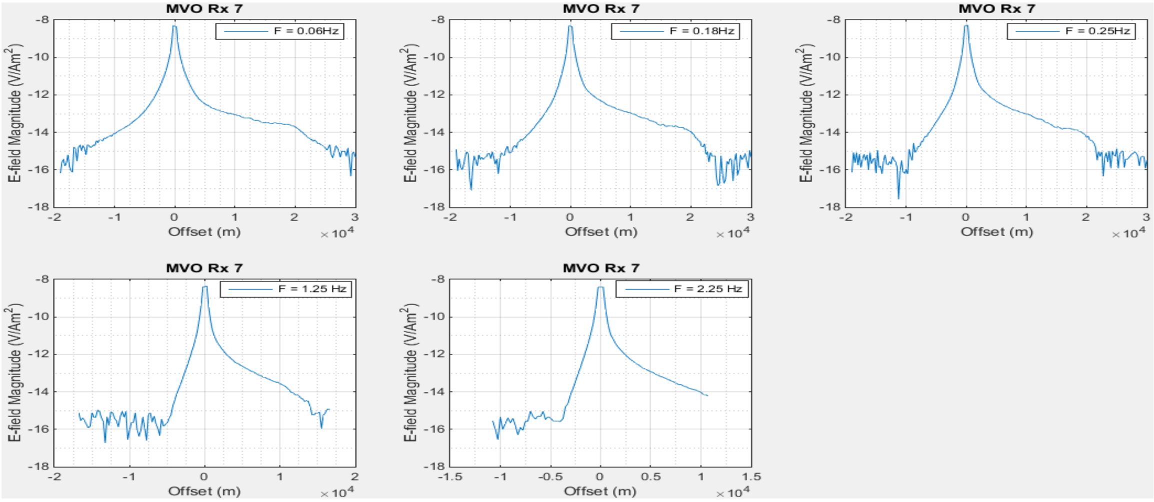

Figure 88. Magnitude versus Offset of Rx7 showing the resistive anomalous data at different acquisition frequency.

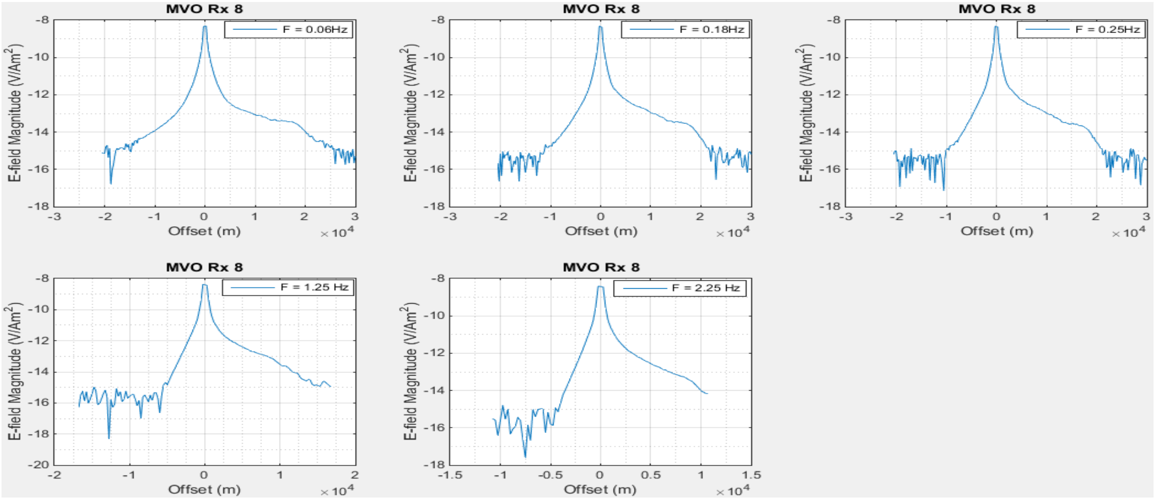

Figure 89. Magnitude versus Offset of Rx8 showing the resistive anomalous data at different acquisition frequency.

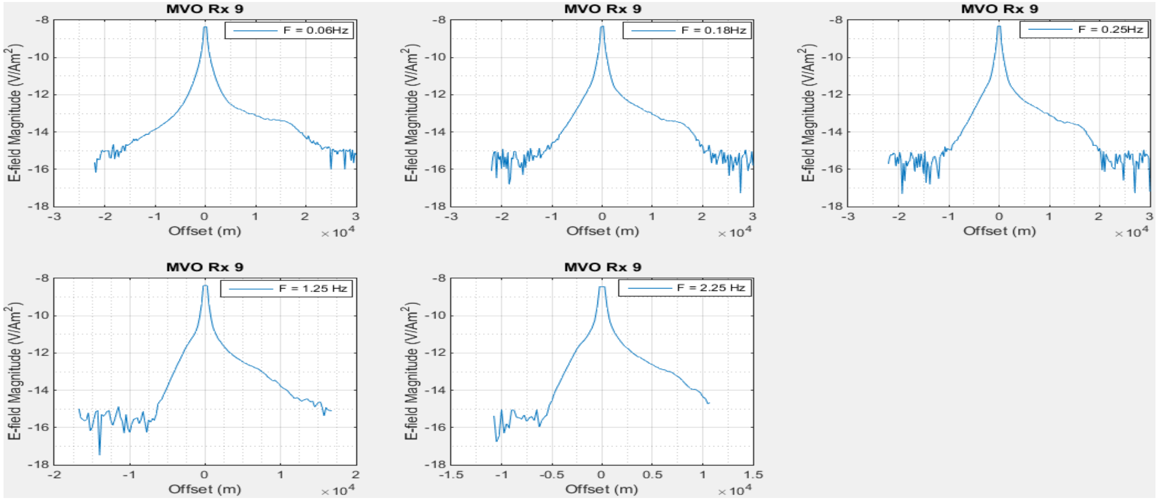

Figure 90. Magnitude versus Offset of Rx9 showing the resistive anomalous data at different acquisition frequency.

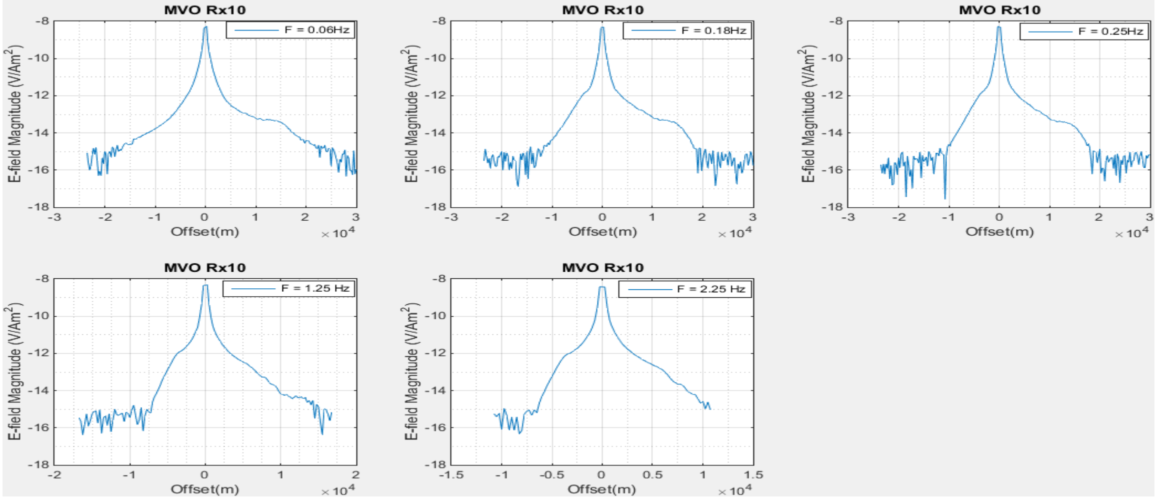

Figure 91. Magnitude versus Offset of Rx10 showing the resistive anomalous data at different acquisition frequency.

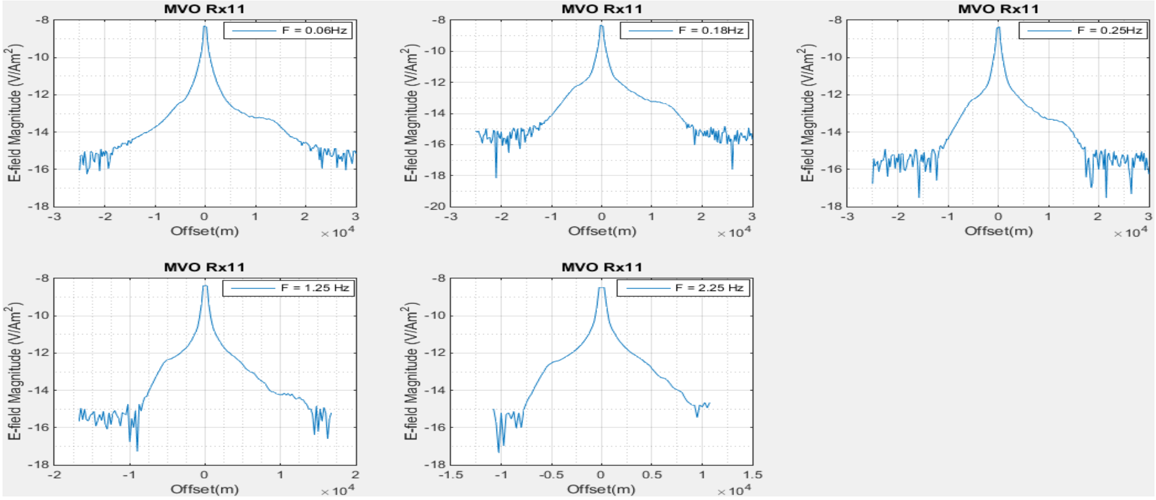

Figure 92. Magnitude versus Offset of Rx11 showing the resistive anomalous data at different acquisition frequency.

Appendix C

GOM Data Asymmetry Attribute at Integrated Offsets

Figures showing non-normalized and normalized asymmetry attribute profiled at integrated range of offsets at interval of 250 m for short offsets (3250 m to 5500 m) and long offsets (6000 m to 8250 m).

- Asymmetry attribute Profile at integrated range of short offsets, i.e., offsets from 3250 m to 5500 m.

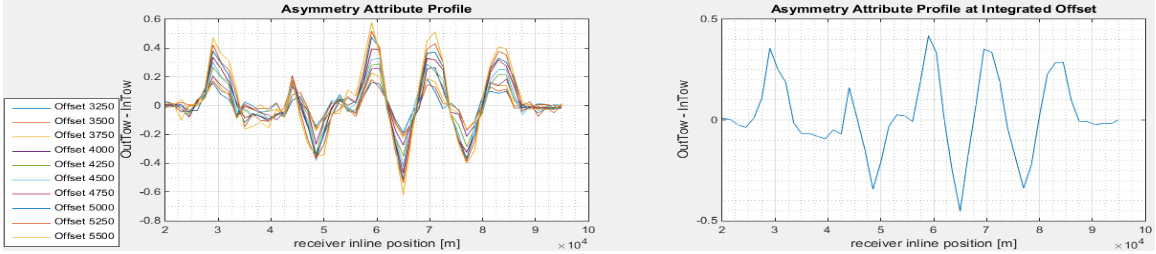

Figure 93. Non-normalized Asymmetry profile at integrated range of offsets for frequency of 0.06 Hz.

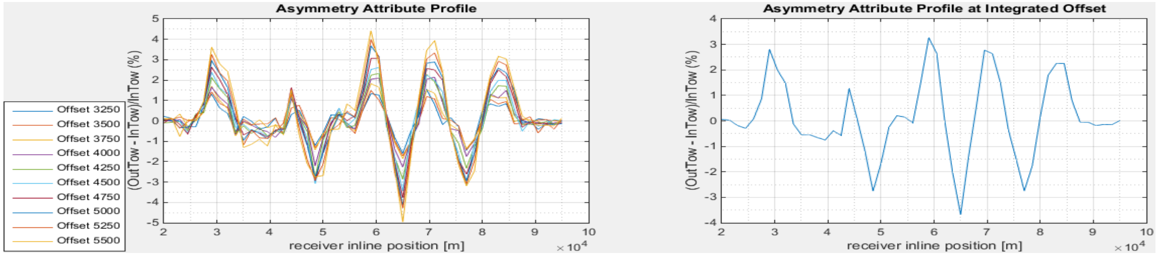

Figure 94. Normalized Asymmetry profile at integrated range of offsets for frequency of 0.06 Hz.

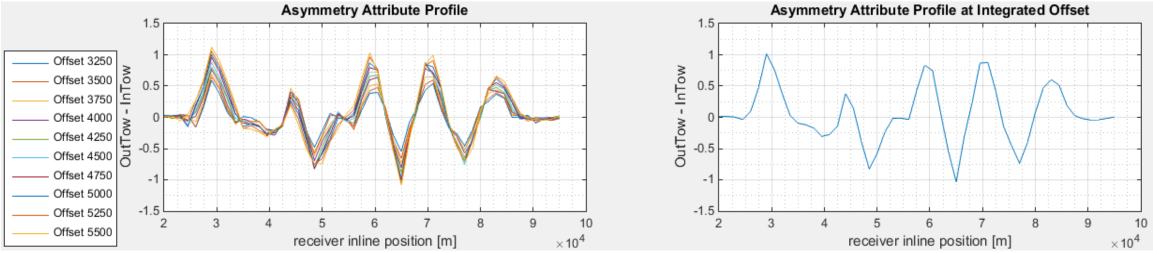

Figure 95. Non-normalized Asymmetry profile at integrated range of offsets for frequency of 0.18 Hz.

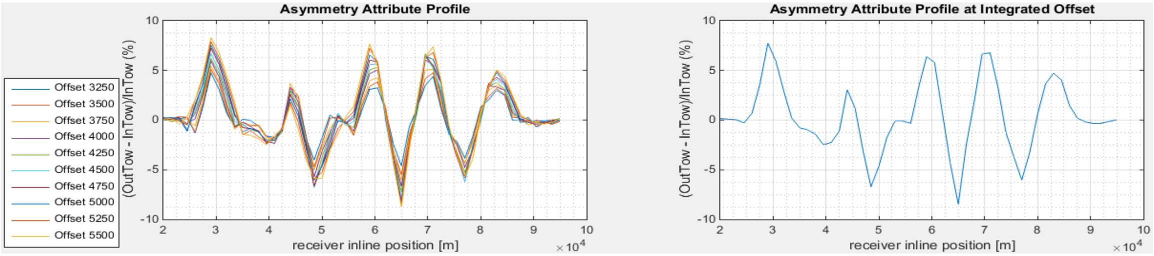

Figure 96. Normalized Asymmetry profile at integrated range of offsets for frequency of 0.18 Hz.

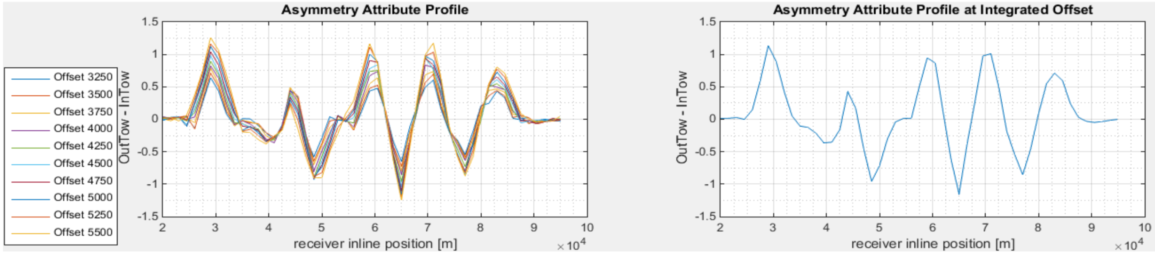

Figure 97. Non-normalized Asymmetry profile at integrated range of offsets for frequency of 0.25 Hz.

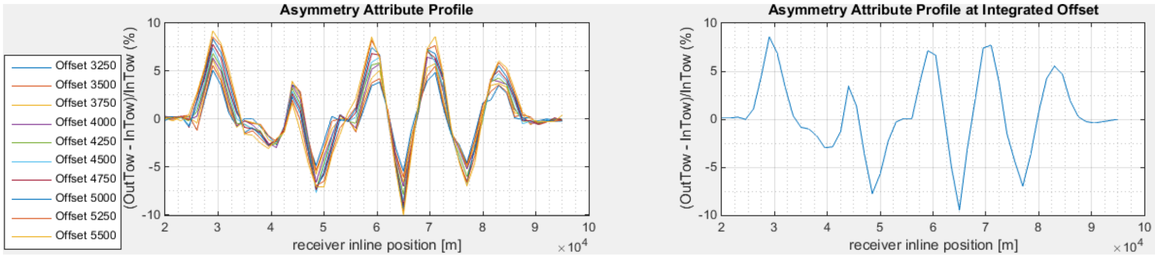

Figure 98. Normalized Asymmetry profile at integrated range of offsets for frequency of 0.25 Hz.

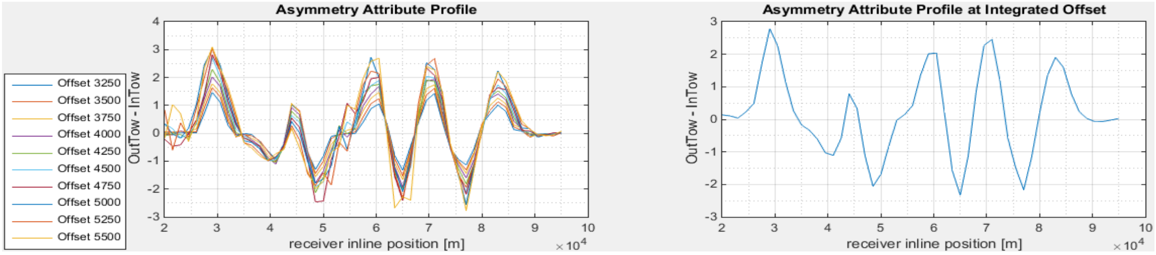

Figure 99. Non- normalized Asymmetry profile at integrated range of offsets for frequency of 1.25 Hz.

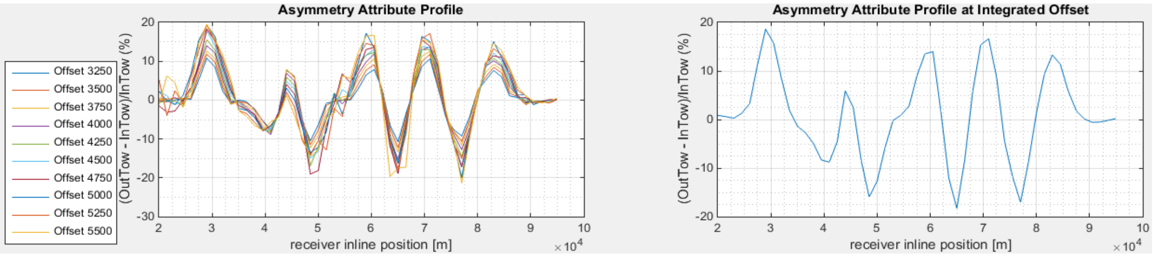

Figure 100. Normalized Asymmetry profile at integrated range of offsets for frequency of 1.25 Hz.

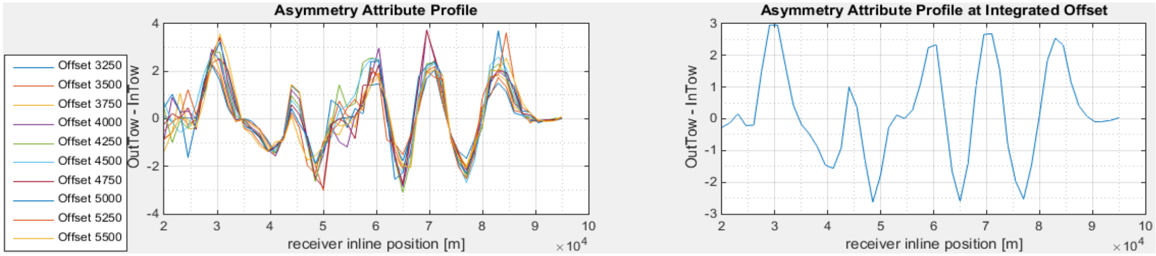

Figure 101. Non-normalized Asymmetry profile at integrated range of offsets for frequency of 2.25 Hz.

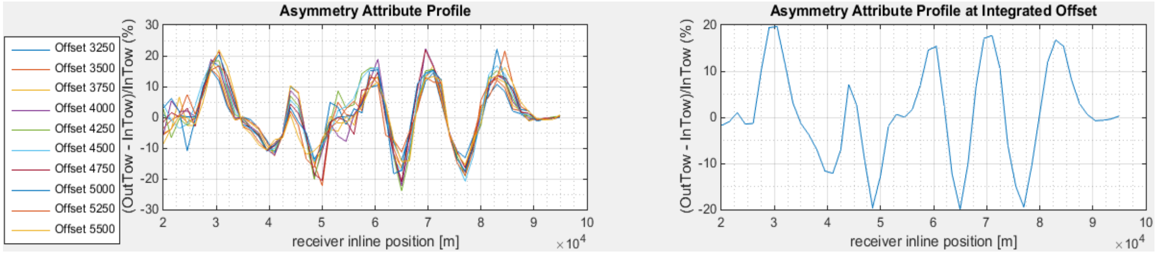

Figure 102. Normalized Asymmetry profile at integrated range of offsets for frequency of 2.25 Hz.

- Asymmetry attribute Profile at integrated range of long offsets, i.e., offsets from 6000 m to 8250 m.

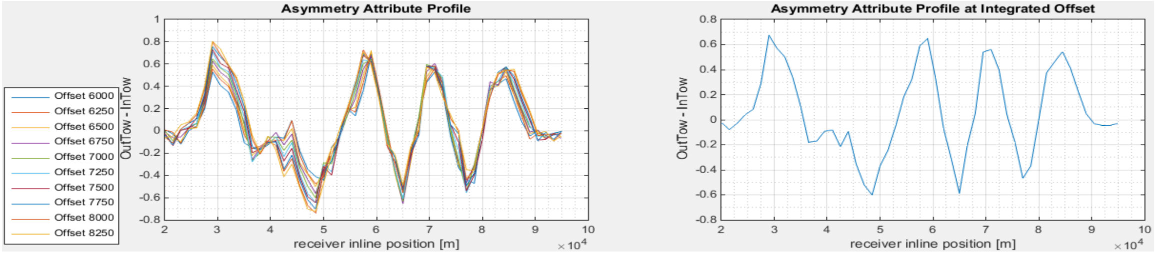

Figure 103. Non-normalized Asymmetry profile at integrated range of offsets for frequency of 0.06 Hz.

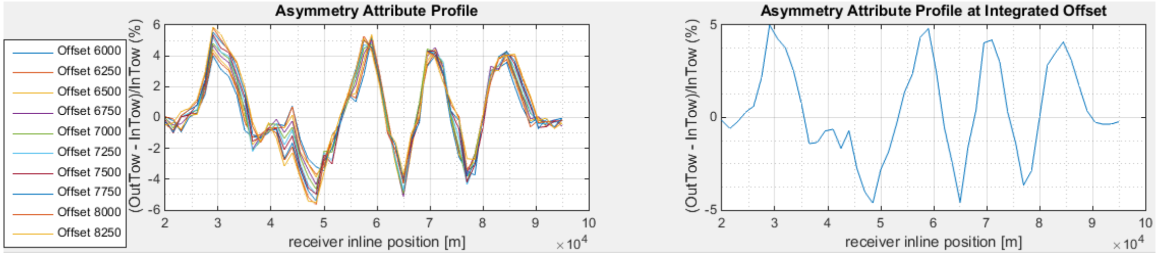

Figure 104. Normalized Asymmetry profile at integrated range of offsets for frequency of 0.06 Hz.

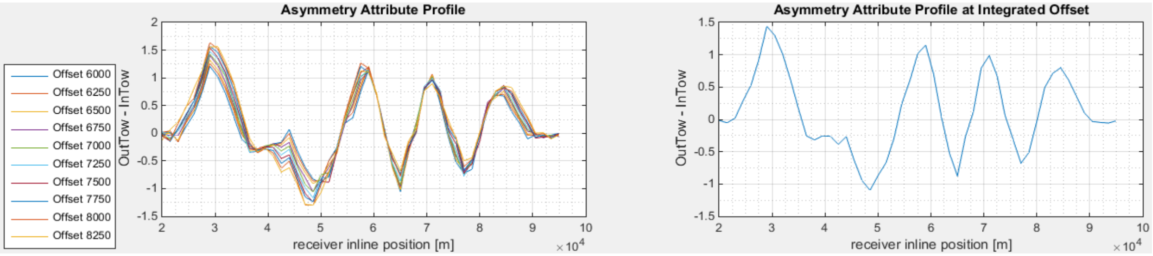

Figure 105. Non-normalized Asymmetry profile at integrated range of offsets for frequency of 0.18 Hz.

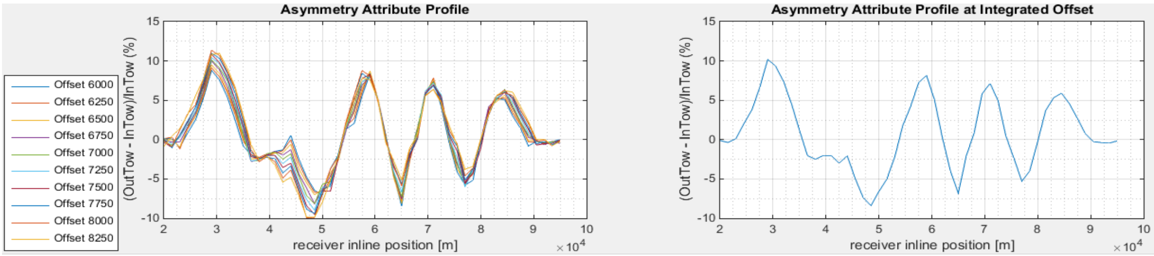

Figure 106. Normalized Asymmetry profile at integrated range of offsets for frequency of 0.18 Hz.

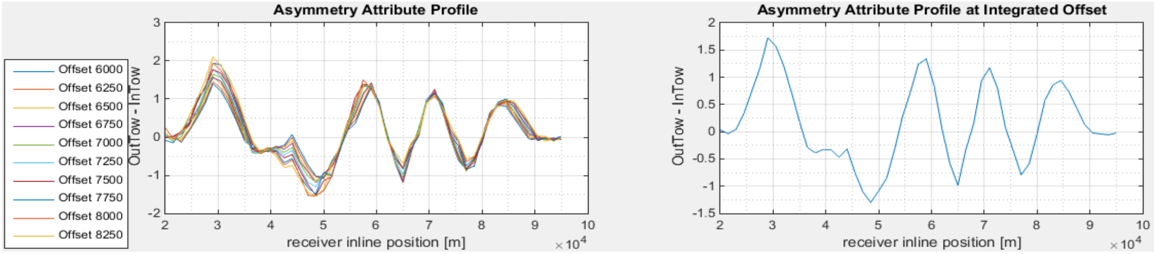

Figure 107. Non-normalized Asymmetry profile at integrated range of offsets for frequency of 0.25 Hz.

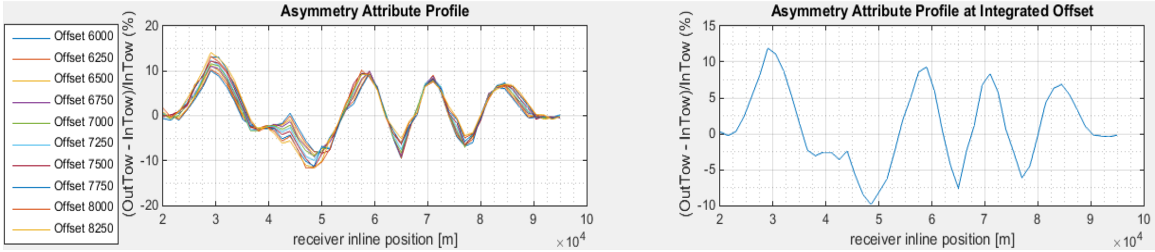

Figure 108. Normalized Asymmetry profile at integrated range of offsets for frequency of 0.25 Hz.

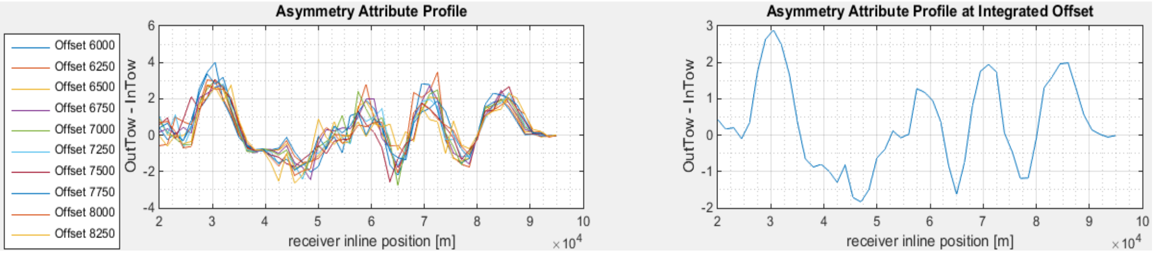

Figure 109. Non-normalized Asymmetry profile at integrated range of offsets for frequency of 1.25 Hz.

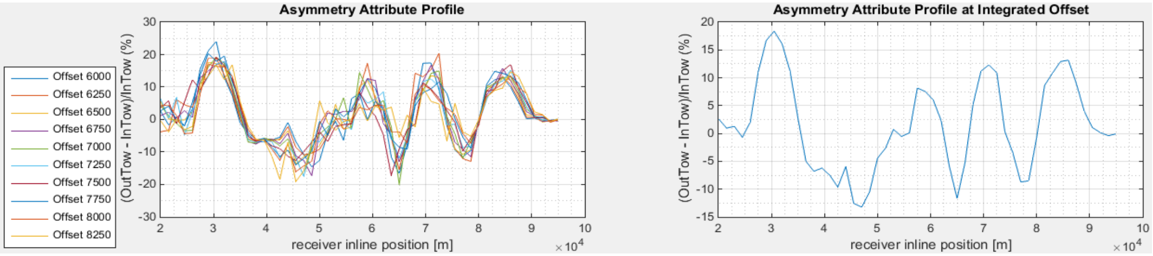

Figure 110. Normalized Asymmetry profile at integrated range of offsets for frequency of 1.25 Hz.

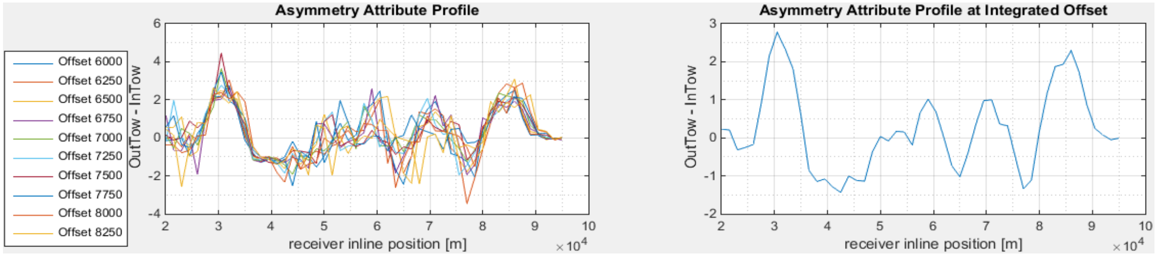

Figure 111. Non-normalized Asymmetry profile at integrated range of offsets for frequency of 2.25 Hz.

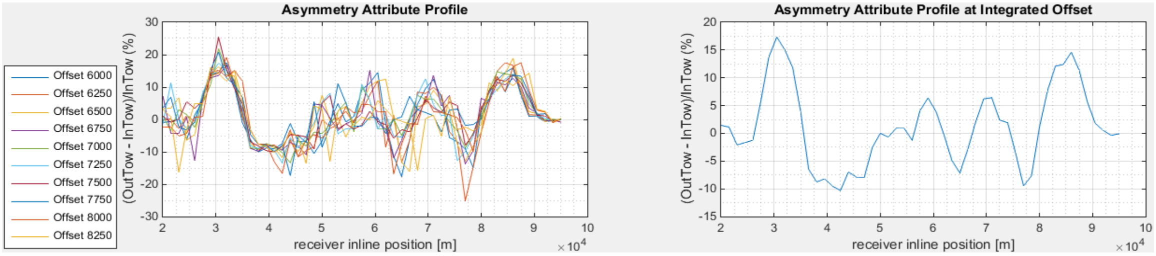

Figure 112. Normalized Asymmetry profile at integrated range of offsets for frequency of 2.25 Hz.